

# Development of non-thermal DBD microplasma reactor for combustion applications

**Citation for published version (APA):**

Elkholy, A. H. E. (2019). *Development of non-thermal DBD microplasma reactor for combustion applications*. [Phd Thesis 1 (Research TU/e / Graduation TU/e), Mechanical Engineering]. Technische Universiteit Eindhoven.

**Document status and date:**

Published: 25/10/2019

**Document Version:**

Publisher's PDF, also known as Version of Record (includes final page, issue and volume numbers)

**Please check the document version of this publication:**

- A submitted manuscript is the version of the article upon submission and before peer-review. There can be important differences between the submitted version and the official published version of record. People interested in the research are advised to contact the author for the final version of the publication, or visit the DOI to the publisher's website.
- The final author version and the galley proof are versions of the publication after peer review.
- The final published version features the final layout of the paper including the volume, issue and page numbers.

[Link to publication](#)

**General rights**

Copyright and moral rights for the publications made accessible in the public portal are retained by the authors and/or other copyright owners and it is a condition of accessing publications that users recognise and abide by the legal requirements associated with these rights.

- Users may download and print one copy of any publication from the public portal for the purpose of private study or research.
- You may not further distribute the material or use it for any profit-making activity or commercial gain
- You may freely distribute the URL identifying the publication in the public portal.

If the publication is distributed under the terms of Article 25fa of the Dutch Copyright Act, indicated by the "Taverne" license above, please follow below link for the End User Agreement:

[www.tue.nl/taverne](http://www.tue.nl/taverne)

**Take down policy**

If you believe that this document breaches copyright please contact us at:

[openaccess@tue.nl](mailto:openaccess@tue.nl)

providing details and we will investigate your claim.

# Development of Non-Thermal DBD Microplasma Reactor for Combustion Applications

PROEFSCHRIFT

ter verkrijging van de graad van doctor  
aan de Technische Universiteit Eindhoven,  
op gezag van de rector magnificus prof.dr.ir. F.P.T. Baaijens,  
voor een commissie aangewezen door het College  
voor Promoties, in het openbaar te verdedigen op  
vrijdag 25 oktober 2019 om 11:00 uur

door

Ahmed Hussiny Elsaid Elkholy

geboren te Cairo, Egypte



Dit proefschrift van het proefontwerp is goedgekeurd door de promotoren en de samenstelling van de promotiecommissie is als volgt:

voorzitter:	prof.dr.ir. G.M.W. Kroesen
1 <sup>e</sup> promotor:	prof.dr. L.P.H. de Goey
2 <sup>e</sup> promotor:	prof.dr. U.M. Ebert
copromotor(en):	dr. Y. Shoshyn
leden:	dr. J.M. Bergthorson (McGill University)
	prof.dr.ir. G.M.W. Kroesen
	prof.dr.ing. A.J.M. Pemen
	dr.ir. J.A. van Oijen
adviseur(s):	dr.ir. S. Nijdam

*Het onderzoek of ontwerp dat in dit proefschrift wordt beschreven is uitgevoerd in overeenstemming met de TU/e Gedragscode Wetenschapsbeoefening.*

*"Happiness does not come from doing easy work but from the afterglow of satisfaction that comes after the achievement of a difficult task that demanded our best."*

*- Theodore Rubin (1932 - 2019)*



This research was financially supported by the Culture Affairs and Mission Sector, Ministry of Higher Education and Scientific Research, Government of Egypt.

ISBN: 978-90-386-4881-1

Copyright © 2019 by Ahmed Elkholy.

All rights reserved. No part of the material protected by this copyright notice may be reproduced or utilized in any form or by any means, electronic or mechanical, including photocopying, recording or by any information storage and retrieval system, without written permission from the copyright owner.

Printed in the Netherlands.

# Abstract

Despite of the increase in the renewable energy sources, combustion of fossil fuels remains the main energy resource, and it will continue in the future in order to meet the increase in the global energy demand. However, due to their impact on the environment, regulations on carbon dioxide and pollutant emissions become more strict. As a containment, scientists are working toward fuel-lean combustion to meet these strict regulations. The main challenge of the fuel-lean combustion is its poor stability, thus new technologies are required to achieve a reliable combustion system. In this study, the use of nanosecond-pulsed repetitive plasma discharge is examined as a potential method to achieve a more stable premixed combustion system.

A new dielectric-barrier (DBD) microplasma flow reactor driven by nanosecond high-voltage pulses has been developed. By this design we were able to sustain a non-equilibrium plasma discharge in a pattern of 400  $\mu\text{m}$  diameter channels at pressures up to 1 bar. The microplasma flow reactor is a promising device for a wide range of applications that require an efficient interaction between a non-thermal plasma discharge and a gas flow. Some of these applications are pollutant control,  $\text{CO}_2$  to  $\text{CO}$  conversion, plasma-assisted combustion and plasma medicine.

Time-resolved electrical and optical measurements have been conducted to characterize the main features of the plasma discharge in the DBD microplasma reactor. Pulse energy per channel of about 1.5  $\mu\text{J}$  has been calculated from the current and voltage time evolution. The discharge at low pressure is characterized by high vibrational temperatures (3980 K) and high reduced electric field strengths (9000 Td) compared to atmospheric pressure (3460 K and 550 Td), which indicates a higher electron energy at lower pressure. Based on natural luminosity images, all gas flowing through the reactor can be assumed to interact with the plasma at 50 mbar. At higher pressures, the emission concentrates at the channel walls and not all gas is in direct contact with the plasma. The distribution of the plasma-generated radicals, however, is unknown. The luminous part of the plasma is strongly non-thermal, with vibrational temperatures of about 4000 K, but the gas temperature remains only a few degrees above ambient. In addition, we have noticed that the discharge emission intensity slightly decreases by increasing the air

flow velocity through the channels at atmospheric pressure due to the lower pre-ionization level at higher velocities. A reactor lifetime study showed around 100 minutes lifetime at low pressure. Nevertheless, more effort is needed to increase the lifetime of the reactor in order to transfer it to real applications at higher pressures.

The initial characterization of a new burner design to study the effect of non-thermal plasma discharge on combustion characteristics at atmospheric pressure is presented. The burner allows stabilizing an inverted cone flame in a mixture flowing through a perforated plate designed as a microplasma reactor. The design principle of the microplasma reactor is based on the dielectric barrier discharge scheme which helps to generate a stable non-thermal plasma discharge driven by nanosecond high-voltage pulses in the burner holes.

The influence of a high-voltage (5 kV) pulsed nanosecond discharge on the laminar burning velocity of methane-air flame has been investigated over a range of equivalence ratios (0.55 - 0.75). The laminar burning velocity was calculated by the conical flame-area method which has been validated by other published data. CH\* chemiluminescence image analysis has been applied to accurately determine the flame area. The results show an increase of the burning velocity of about 100% in very lean ( $\phi = 0.55$ ) flames as a result of the plasma discharge effect. The use of plasma discharge is also found to extend the lean blow-off limit of the premixed flames. This extension depends strongly on the pulse repetition frequency or average discharge power.

Finally, the local effect of the plasma discharge on the burning velocity at different vertical locations from the plasma source was investigated. The local burning velocity was obtained using stream-tube method with the help of PIV velocity measurement and Able inverted flame images. The experiment shows that the burning velocity of the flame is improved, but this improvement is independent of the distance from the plasma source, for all the plasma conditions that have been covered in this study. This proves that, for the studied distances from the plasma source, there is no local effect of the plasma discharge on the burning velocity. This means that the dominant mechanism is the thermal mechanism and there is no evidence of any local improvement due to chemical or aerodynamic mechanisms.

# Contents

<b>1</b>	<b>Introduction</b>	<b>1</b>
1.1	Background . . . . .	1
1.2	Plasma classification . . . . .	2
1.3	Plasma Generation . . . . .	3
1.4	Non-thermal atmospheric pressure plasmas . . . . .	5
1.4.1	Pulsed Corona Discharges . . . . .	6
1.4.2	Dielectric Barrier Discharge . . . . .	6
1.4.3	Packed-Bed Discharges . . . . .	8
1.4.4	Atmospheric Pressure Plasma Jets . . . . .	8
1.4.5	Nanosecond Repetitively Pulsed (NRP) Discharges . . . . .	9
1.5	Combustion . . . . .	10
1.5.1	Flame stabilization . . . . .	12
1.5.2	Laminar burning velocity . . . . .	13
1.5.3	Plasma-Assisted Combustion (PAC) . . . . .	15
1.6	Objective and Contribution . . . . .	18
1.7	Outline of the Thesis . . . . .	19
<b>2</b>	<b>DBD Microplasma Reactor</b>	<b>21</b>
2.1	Introduction . . . . .	21
2.2	Geometry design and material . . . . .	24
2.3	Fabrication process . . . . .	26
2.4	Reactor lifetime . . . . .	30
2.5	Potential applications of the DBD microplasma reactor . . . . .	31
2.5.1	Flow reactor . . . . .	31
2.5.2	Wounds and skin treatment . . . . .	32
2.5.3	Plasma assisted combustion . . . . .	32
2.6	Summary . . . . .	33

<b>3</b>	<b>Experimental setup</b>	<b>35</b>
3.1	Introduction . . . . .	35
3.2	Experimental setup . . . . .	36
3.3	Electrical setup . . . . .	41
3.4	Optical emission spectroscopic setup . . . . .	43
3.4.1	Wavelength calibration . . . . .	43
3.4.2	Apparatus function . . . . .	43
3.5	High-speed imaging setup . . . . .	44
3.6	Error estimation . . . . .	45
3.7	Summary . . . . .	47
<b>4</b>	<b>Plasma discharge characteristics</b>	<b>49</b>
4.1	Introduction . . . . .	49
4.2	Electric characteristics . . . . .	50
4.2.1	Electrical breakdown in micro-channels . . . . .	52
4.2.2	Synchronization . . . . .	52
4.2.3	Voltage and current measurements . . . . .	54
4.2.4	Pulse energy calculation . . . . .	54
4.3	Optical investigation on DBD microplasma reactor . . . . .	54
4.4	Plasma emission . . . . .	57
4.5	Discharge temperature . . . . .	58
4.5.1	Rotational temperature . . . . .	58
4.5.2	Vibrational temperature . . . . .	59
4.5.3	Average gas temperature . . . . .	60
4.6	Effective reduced electric field strength $(E/N)_{\text{eff}}$ . . . . .	62
4.7	Effect of flow rate on discharge intensity . . . . .	67
4.8	Effect of pulse repetition frequency on discharge deposited energy	68
4.9	Effect of equivalence ratio on the discharge characteristics . . . . .	70
4.9.1	Full-breakdown frequency . . . . .	70
4.9.2	Pulse energy . . . . .	72
4.9.3	Kinetic and transport coefficients of electrons in methane/air mixtures . . . . .	72
4.10	Summary . . . . .	75

---

<b>5</b>	<b>Effect of non-thermal plasma on flame stabilization and emissions</b>	<b>77</b>
5.1	Introduction . . . . .	77
5.2	Modification of the reactor geometry . . . . .	79
5.3	Burning velocity measurements . . . . .	79
5.4	Thermal contribution to the burning velocity enhancement . . . . .	84
5.5	Effect of plasma on blow-off limits. . . . .	86
5.6	Nitric Oxides measurements . . . . .	89
5.7	Summary and Conclusions . . . . .	91
<b>6</b>	<b>Effect of the plasma discharge on local burning velocity: A particle image velocimetry study</b>	<b>93</b>
6.1	Introduction . . . . .	93
6.2	Working principle of PIV . . . . .	94
6.3	Experimental setup . . . . .	95
6.4	Effect of seeding particle density on plasma discharge . . . . .	97
6.5	Velocity measurements . . . . .	100
6.6	Local burning velocity measurements . . . . .	101
6.6.1	Governing equations . . . . .	102
6.6.2	Temperature measurement. . . . .	104
6.6.3	Local burning velocity determination . . . . .	107
6.7	Summary and Conclusions . . . . .	111
<b>7</b>	<b>Summary, conclusions and recommendations</b>	<b>113</b>
7.1	Overview . . . . .	113
7.2	Summary and conclusion . . . . .	113
7.3	Recommendation for future work . . . . .	115
<b>A</b>	<b>Unsuccessful reactor geometries</b>	<b>117</b>
A.1	Surface electrodes reactor . . . . .	117
A.2	Wire electrodes reactor . . . . .	118
A.3	Insulated thick metal reactor . . . . .	119
<b>B</b>	<b>Testing protocol for the NPG-6/15k pulse generator</b>	<b>121</b>



---

<b>C Faraday cage</b>	<b>123</b>
C.1 The electromagnetic field measurements . . . . .	123
C.2 Faraday cage design . . . . .	125
C.2.1 Skin depth . . . . .	125
C.2.2 Minimum hole sizes . . . . .	126
C.2.3 The EMF after using the Faraday cage . . . . .	126
<b>D Electron-impact reactions with molecules and radicals for methane-air mixture</b>	<b>129</b>
<b>Bibliography</b>	<b>131</b>
<b>List of Symbols</b>	<b>143</b>
<b>List of Abbreviations</b>	<b>145</b>
<b>Acknowledgments</b>	<b>147</b>
<b>List of Publications</b>	<b>149</b>
<b>Curriculum Vitae</b>	<b>151</b>

## Introduction

---

---

### 1.1 Background

Similar to blood plasma, Irving Langmuir introduced the term *plasma* for the ionized gas in 1928. Plasma, a quasi-neutral gas, is widely known as the fourth fundamental state of matter. It can be considered as a gaseous mixture of negatively charged electrons, highly charged positive ions, free radicals, photons and excited species, as shown in Fig. 1.1. Plasma exists naturally, and forms more than 99% of the visible universe. On earth, it also can be obtained, artificially, for industrial and laboratory purposes. The existence of free electrons and ions makes plasma highly interactive and electrically conductive, which affects its electrical and chemical behavior.

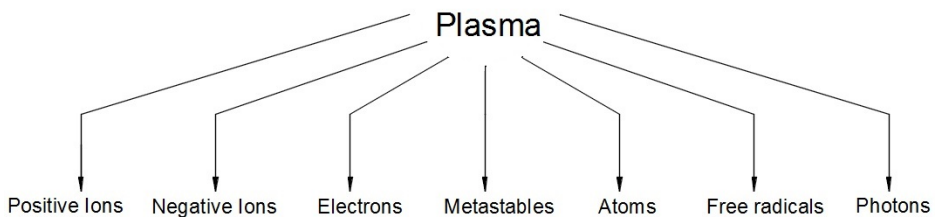


Figure 1.1: Constituents of plasma (Nehra et al. 2008).

Although plasma itself has its own domain of science and applications, it also can be merged with many different applications to enhance their performance. Some of these applications are microelectronics, water purification, atomic layer deposition, chemical synthesis, materials processing, surface treatment, chemical conversion, etc. With the recent need in alternative energy sources and environmental concerns, plasma took a role in hydrogen production, biomass conversion,

emission treatment and plasma ignition and stabilization of flames (Yazicioglu and Latircioglu 2017).

The use of electric fields to enhance flame characteristics was initially investigated in the early 19th century (Brande 1814), then it was implemented in applications during the 20th century. When the electric field is sufficiently strong to breakdown the gas mixture, plasma effects will be present. This plasma enhances the combustion in terms of ignition, stabilization, and combustion emission. Rapid progress in the electronic industry in the late 20th century led to the exploration of new types of plasma sources, like nanosecond and picoseconds high-voltage pulse generators. The plasma discharge generated by these power sources have different thermal and chemical characteristics compared to the traditional plasma sources, which make them favorable to combustion science.

This chapter will include a brief overview of plasma classification, combustion stabilization, a historical overview of plasma-assisted combustion, and the motivation of applying plasma discharge in combustion applications and research.

## 1.2 Plasma classification

Plasma discharges can be classified into two main groups, as shown in Table 1.1. The first group consists of 'high-temperature plasma' (HTP) where all species (electrons, ions, and neutral species) are in a thermal equilibrium state. This means that  $T_e \cong T_i \cong T_g$  where  $T_e$ ,  $T_i$  and  $T_g$  are the temperatures of the electron, ion and gas molecules, respectively. The second group contains the 'low-temperature plasma', which can be further subdivided. One subgroup is referred to as 'thermal plasma', also called quasi-equilibrium plasma, which is in a local thermal equilibrium (LTE) state. Such plasmas can be produced by atmospheric arcs, sparks, and flames. Thermal plasma is associated with a significant Joule heating, thermal ionization and high power density at high operating pressures. However, thermal plasma has low excitation selectivity and is characterized by very high gas temperature ( $T_g$ ) and relatively limited energy efficiency.

Table 1.1: Classification of plasma.

Plasma	State	Example
High-temperature plasma		
Equilibrium plasma	$T_e \cong T_i \cong T_g = 10^6 - 10^8 \text{K}$ $n_e \geq 10^{20} \text{m}^{-3}$	Fusion plasma.
Low-temperature plasma		
Thermal plasma (Quasi-equilibrium plasma)	$T_e \cong T_i \cong T_g \leq 2 \cdot 10^4 \text{K}$ $n_e \geq 10^{20} \text{m}^{-3}$	Arc plasma, torches, RF discharges
Non-thermal plasma (Non-equilibrium plasma)	$T_e \gg T_i \cong T_g = 300 - 10^3 \text{K}$ $n_e \cong 10^{10} \text{m}^{-3}$	Glow, corona, APPJ, DBD, MHCD

The second subgroup is the 'non-thermal plasma' (NTP), also called non-equilibrium plasma or cold plasma. In the non-thermal plasma discharge, the electron temperature is about 1 eV (about 10,000 K), while the gas temperature is close to room temperature or slightly higher. The main characteristics of this plasma type are determined by the electron temperature,  $T_e$ , and the electron density,  $n_e$ . As shown in Fig 1.2, different types of plasma discharges can be determined by their coordinates in a plot of  $T_e$  vs.  $n_e$ .

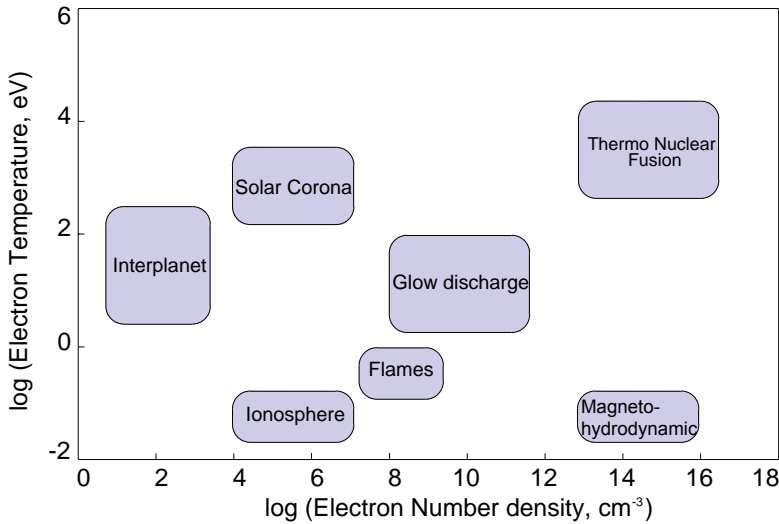


Figure 1.2: Electron temperatures verses electron densities for different kind of plasmas (Fridman 2008).

In the present work we are dealing with a non-thermal plasma discharge, which has the following features: (1) the plasma is driven electrically; (2) collisions of charged particles with neutral gas molecules are important; (3) there are boundaries at which surface losses are important; (4) ionization of neutrals sustains the plasma in steady state; and (5) the electrons are not in thermal equilibrium with the ions (Lieberman and Lichtenberg 2005).

## 1.3 Plasma Generation

Plasmas are generated by supplying energy to a gas causing the formation of charge carriers. Discharge ignition will occur if the applied energy is high enough to provide the electrons with a sufficient energy for excitation or ionization when

they collide with molecules. When the ionization collisions occur, a new set of electrons will be generated. The new electrons together with the colliding electrons will gain more energy from the electric field to ionize more atoms, creating an ionization wave. This ionization process, also called 'Townsend discharge' or 'Townsend avalanche', is responsible for initializing and sustaining the plasma discharge. Plasmas can be classified by the nature of the applied energy source to;

- Thermal energy sources (e.g. flames)
- Beam type energy sources (e.g. laser beam and electron beam)
- Electrical energy sources :
  - Direct current (DC) discharges
  - Alternating current (AC) discharges, like
    - a- Microwave plasmas
    - b- Radio-frequency (RF) plasma, like
      - Capacitively coupled plasmas
      - Inductively coupled plasmas
  - Pulsed plasma discharges

Each plasma source has its own spatial and temporal characteristics, which can be suitable for a particular application. The choice of the proper source for a specific application requires the study of the characteristics of the various plasmas and a good understanding of the application requirements. The most commonly used method of plasma generating for industrial application is by applying an electric field to the gas. The DC discharge is generally created in closed discharge vessels using interior electrodes. It has the advantage that the microscopic physical processes are well known and understood, and plasmas can be diagnosed in detail. Besides, the power sources are well developed and broadly used. The disadvantage is that the interior electrodes have a limited lifetime, and they may react with the medium between the electrodes (Conrads and Schmidt 2000).

AC discharges can operate with insulated, external electrodes, or electrodeless. Therefore, reaction with the medium is unlikely, which results in longer lifetime. Microscopic processes in RF discharges are rather complex. Diagnostics tools are well developed, but sometimes difficult to use due to interference by RF noise. Microwave discharge produces high density plasma in the pressure range from 10 Pa up to atmospheric pressure, and it is generated without electrodes. The electron energy in the microwave plasma is relatively low compared to DC discharges. Microwave power sources are expensive for the high-power applications.

Pulsed discharge sources have the advantage of high-power density and are easy to control by changing the pulse duty cycle. Additionally, they produce

highly non-equilibrium discharges which are favorable for many applications. More advantages of this type will be covered in this thesis in detail. However, pulsed plasma power sources and diagnostics tools are complicated and rather expensive.

Plasma can also be generated by non-electrical sources, like electron beam or laser beam, so-called 'beam-produced plasma discharges'. In this type, the plasma is sustained by the interaction between an electron or photon beam with the gaseous medium. The beam plasmas are characterized by high energy efficiency, about 70% of the beam energy can be transferred to the plasma. It is possible to create plasmas with high degrees of ionization in low-pressure environments.

## 1.4 Non-thermal atmospheric pressure plasmas

Non-thermal plasma discharges have gained great attention in the last decades due to their unique features that make them very promising in many industrial applications. The concept behind non-thermal plasmas is that the electron mass is, approximately, 2000 times lower than the ion mass. This makes it much easier for electrons to gain energy than ions and neutral species. However, to generate non-thermal plasma, a non-equilibrium thermodynamic situation should be achieved. This may be reached by an abrupt change of the macroscopic conditions (volume, pressure, temperature) or by applying an external force to the gas (i.e. electric or magnetic field). Applying an electric field is the most applicable way to achieve this condition. First, the energy transfers to the electrons, then they transfer their energy by means of inelastic collisions with the particles of the gas, creating excited species, ions, radicals, photons as well as additional free electrons through electron-impact ionization. The energy can be interchanged by means of electronic, vibrational, rotational, and translational collision processes (Hippler et al. 2001). In such kind of plasma, typical mean electron energy may range from 0.5 eV to 5 eV, while the energy of the heavy particles is about 0.025 eV to 0.05 eV corresponding to 300 K to 600 K. Average charge carrier densities are  $10^8 \text{ cm}^{-3}$  to  $10^{12} \text{ cm}^{-3}$ .

Non-thermal plasma discharges can be generated by different electrical discharges such as corona discharge, micro hollow cathode discharge, atmospheric pressure plasma jet (APPJ), gliding arc discharge, atmospheric uniform glow discharge, dielectric barrier discharge (DBD) and plasma needle. Non-thermal plasma offers better selectivity and energy efficiency than thermal plasma, (Nehra et al. 2008). The main advantage of this kind of discharges is that the input energy to the system goes into energetic electron production instead of elevating the gas temperature. Controlling the electron energy threshold, by means of the input energy characteristics, makes it ideal for a variety of plasma-assisted processes. In the following sections, we will discuss several non-thermal plasma generation techniques. One of them is the dielectric barrier discharge (DBD) as one of the most

efficient and widely used methods to generate a non-thermal plasma discharge at atmospheric pressure.

### 1.4.1 Pulsed Corona Discharges

A corona discharge happens due to the ionization of the gas surrounded by an electrically charged conductor. It always happens near sharp edges where the electric field is sufficiently capable to form a conductive region, but not high enough to cause electrical breakdown or arcing to nearby objects. Pulsed corona discharges are promising in many applications due to their high output power, without streamer transformation into sparks, compared to continuous coronas. Figure 1.3 shows some examples of corona discharges.

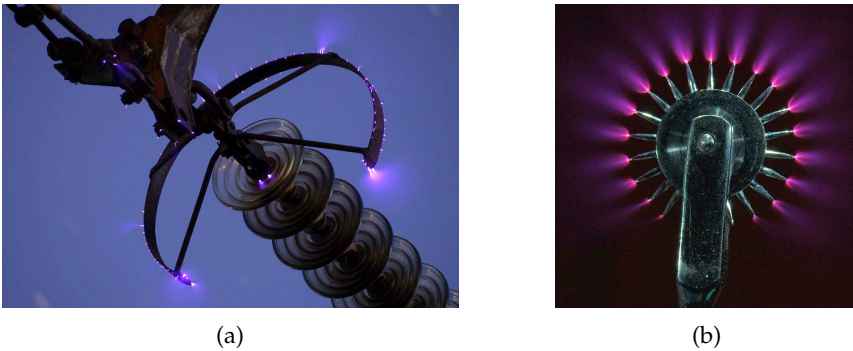


Figure 1.3: Examples of corona discharges: (a) corona discharge on an insulator string of a 500 kV overhead power line, and (b) corona discharge on a Wartenberg wheel. [Source: Wikipedia.org/wiki/Corona\_discharge]

### 1.4.2 Dielectric Barrier Discharge

Dielectric-barrier discharge (DBD), or silent discharge, is the electrical discharge between two electrodes separated by an insulating dielectric layer placed in the current path. It was first reported by Ernst Werner von Siemens in 1857 to generate Ozone from oxygen or air at atmospheric pressure Kogelschatz et al. (1999). He found that a plasma discharge can be initiated between two coaxial electrodes covered by a coaxial glass tube. A high-amplitude alternating current was used to generate a radial electric field in order to cause an electrical breakdown in the flowing gas. The glass acts as a dielectric which barriers the plasma discharge, so it was originally called '*silent discharge*' by (Andrews and Tait 1860), and later it became '*dielectric barrier discharge (DBD)*'. Figure 1.4 shows the most common configurations of dielectric barrier discharge, (Nehra et al. 2008).

A dielectric barrier discharge works at a strongly non-equilibrium condition at atmospheric pressure. It can work with different power source types like pulsed DC, AC or nanosecond high-voltage pulses. The discharge gap is varied between 0.1 mm to several centimeters, depending on the dielectric material, thickness, peak voltage, operating pressure, and gas. The typical dielectric material should have high breakdown strength and low dielectric constant, such as quartz, ceramics, and fiberglass. In DBDs the dielectric layer separates between the discharge and electrodes, which protects the electrodes from etching and corrosion.

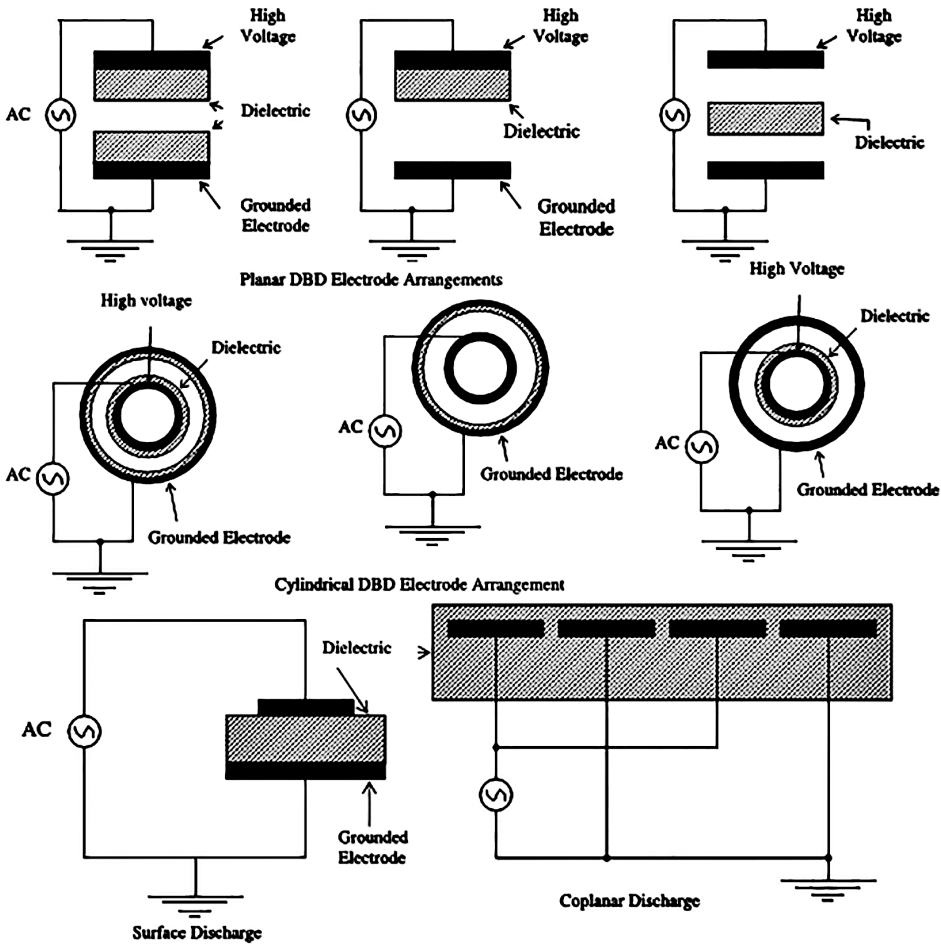


Figure 1.4: Typical configurations of dielectric barrier discharges (Nehra et al. 2008).

The non-thermal features and the ease of manufacturing of DBDs make it ideal for a broad range of applications from small laboratory reactors to large industrial installations with several kilowatt input power. Some of these appli-



cations are ozone generation, excimer UVR optical source, surface treatment, high power CO<sub>2</sub> lasers, excimer based mercury-free fluorescent lamps, and flat large-area plasma displays (Kogelschatz 2003).

### 1.4.3 Packed-Bed Discharges

A packed-bed reactor can be considered as a special configuration of the DBD reactor where pellets are placed inside a discharge region between two electrodes, as shown in Fig. 1.5. A high voltage of about 15-30 kV is required to create a non-thermal plasma in the void space between the pellets. The material of the pellets can be non-catalytic or catalytic. Several studies have been done to address the effect of the material, diameter and porosity of the pellets on the reactor performance, (Chen et al. 2008a) and (Warnock et al. 2005).

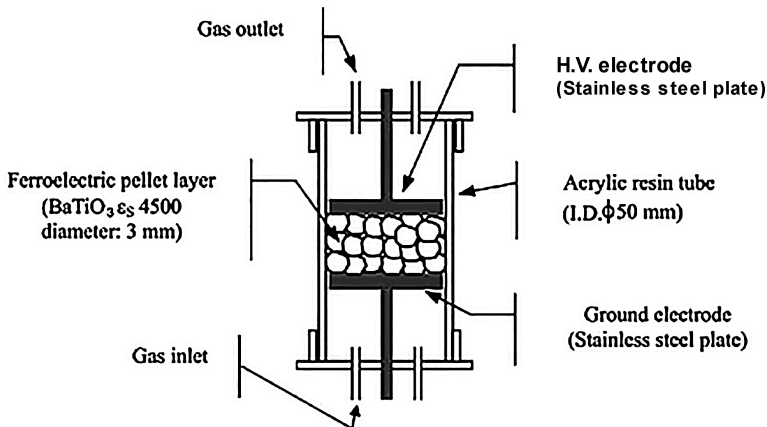


Figure 1.5: Example of a packed-bed bio-reactor (Warnock et al. 2005).

### 1.4.4 Atmospheric Pressure Plasma Jets

Atmospheric pressure plasma jets (APPJs) are non-thermal, high pressure, uniform glow plasma discharges that produce a stream of highly reactive chemical species. The discharge flows in the annular space between an outer cylindrical (grounded) electrode and an inner coaxial (powered) electrode. The ions and electrons are rapidly lost by recombination after exiting from the nozzle. However, the high flow velocity keeps the metastable species and radicals for longer distance after the nozzle exit. APPJs are widely used for medical purposes as well as decontamination devices.



Figure 1.6: Example of using APPJ for human skin treatment. [Source: pedl.tamu.edu]

### 1.4.5 Nanosecond Repetitively Pulsed (NRP) Discharges

Generation of glow discharge at atmospheric pressure can be achieved by two methods. First, by limiting the current by using a resistor-like load in the circuit. However, these current-limiting methods are not an efficient technique for ionization. The practical alternative is the nanosecond repetitively pulsed (NRP) discharge. The theory behind the NPR discharge is to apply a very high electric field which is capable to efficiently ionize the gas but to stop the field before the glow to arc (spark) transition occurs. The pulse repetition rate is controlled so that the inter-pulse duration is shorter than the time needed for the recombination of the active species. This leads to a high electron density due to the accumulation of consecutive pulses. The accumulation of metastable species is also capable of sustaining the discharge and the active species interesting for applications.

The NRP discharge is one of the effective ways to reduce the consumed power needed to obtain a high electron number density in the air at atmospheric pressure without excessively heating the gas. This can be done by tuning the pulse duty cycle, pulse amplitude, and pulse duration. As shown in Fig. 1.9, experimental and numerical studies were done by Rusterholtz (2012), showing the resulting electron density resulting from DC and NRP plasma generation. In their work, 10-ns pulses at pulse repetition rates from 10 to 100 kHz have been used. A power reduction of 2-3 orders of magnitude was possible compared to DC discharges producing an equivalent electron number density.

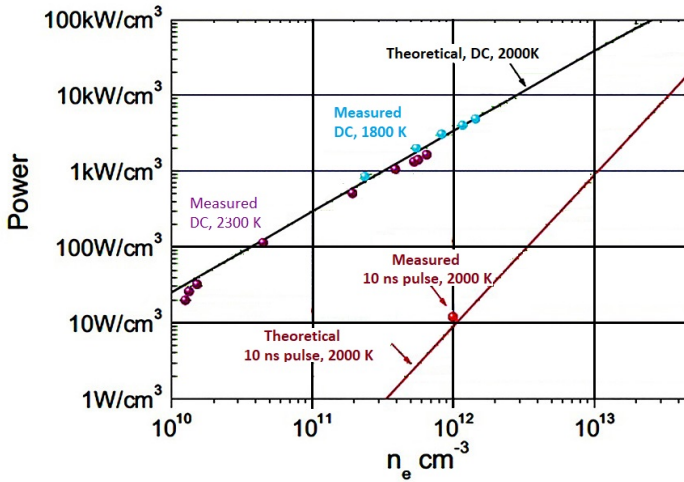


Figure 1.7: Measured and calculated power budget for DC and NRP plasma generation as function of the resulting electron number density. The NRP glow was obtained with a 10-ns, 10-kV, 100-kHz repetitive nanosecond pulse generator. The inter-electrode gap distance was about 1 cm and air was preheated to 2000 K (Rusterholtz 2012).

## 1.5 Combustion

Energy is essential for our modern life. Global energy consumption is projected to increase 28% by 2040 due to economic growth, according to the latest International Energy Outlook 2017 (IEO2017), (Schiffer et al. 2018). Although renewable energy resources are more environmental friendly, they face major obstacles. Some of these obstacles are; high initial cost, large area requirements, geographical limitations and instability of the produced power. Other sources, like nuclear power reactors, also have problems which could accidentally release radiation into the environment and the difficulty of getting rid of the radioactive waste. Therefore, combustion of fossil fuels will possibly remain the main global energy source for the upcoming decades, even with the expected growth in renewable energy sources.

Fossil fuels are some of the cheapest ways to get steady and reliable energy source. Statistically, they supply about 79% of the globe energy consumption in the world (Kumar et al. 2010). Although, the amount of fossil fuels is limited, new oil discoveries can secure the global demand for decades. However, the use of fossil fuel comes with serious impacts to our health and environment. Impacts are sometimes easy to see, such as pollution and land degradation, and sometimes less obvious, such as the costs of asthma and cancer, or the impacts of sea level rise due to the global warming. In fact, the number of deaths attributed to air

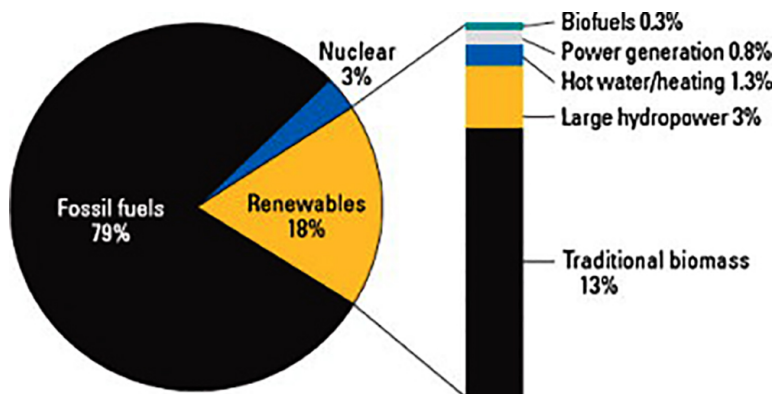


Figure 1.8: Fossil fuel share of the global energy consumption,2008 (Kumar et al. 2010).

pollution each year are 6.5 million deaths, according to the World Health Organization (WHO), which is much greater than the deaths by HIV/AIDS, tuberculosis and road injuries combined. This comes along with the Paris Agreement on climate change, which aims to limit the global mean temperature rise to well below 2 °C above the pre-industrial level. Different emission prediction scenarios are simulated for different economies, energy availability and national and international policies. These scenarios, known as representative concentration pathways (RCPs), are identified by their approximate total (accumulated) radiative emissions at 2100 relative to 1750 (Fuss et al. 2014), see Fig.1.9. The RCPs include a stringent mitigation scenario (RCP2.6), two intermediate scenarios (RCP4.5 and RCP6.0) and one scenario with very high emissions (RCP8.5). Scenarios without additional efforts to constrain emissions ('baseline scenarios') lead to pathways ranging between RCP6.0 and RCP8.5. RCP2.6 is representative of a scenario that aims to keep global warming likely below 2°C above pre-industrial temperatures. A clear goal was formulated to reduce the global CO<sub>2</sub> emissions to half each decade, known as the "carbon law". To meet this objective, numerous efforts in the renewable and non-renewable energy sectors have to be devoted. Among these efforts, combustion community is working to develop improved energy-efficient and cleaner combustion processes.

Lean-premixed combustion systems have proven to be the most efficient and less polluting combustion processes (Huang and Yang 2009). However, combustion instability remains a critical issue limiting the development of low-emission, lean-premixed combustion systems. Unstable combustion is always accompanied by instability in the thermal flux, pressure, and mechanical vibration inside the combustion chambers. Work at such combustion conditions is, of course, not desired.

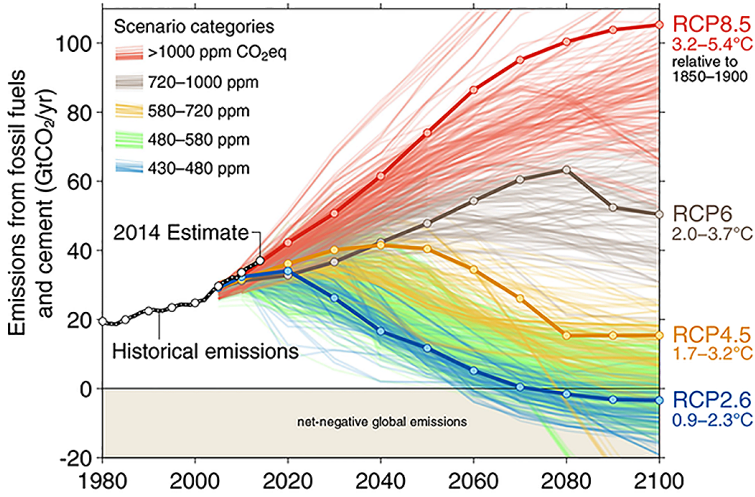


Figure 1.9: Carbon emission pathways (Fuss et al. 2014).

### 1.5.1 Flame stabilization

Flame stabilization is needed to avoid combustion instability in lean-premixed combustion systems. Flame stabilization can be achieved where the local laminar flame speed equals the local flow velocity. Flame liftoff occurs when the laminar burning velocity is lower than the gas flow velocity. It leads to incomplete combustion due to the escape of some of the unburnt mixture. Also the ignition of lifted flame is difficult to be controlled. The other type of flame instability is the flash back, where the laminar burning velocity is higher than the gas flow velocity. In such condition, the flame tends to propagate toward the flame tube, which may result in explosion.

Many methods have been developed to approach a stable flame. Some of them aim to create a location where the burning velocity equal to the flow velocity. Others aim to, continuously, ignite the flame by external ignition source or by recirculation of the hot products. Some of these methods are the following:

- Flame stabilization using a bluff body
- Flame stabilization using a swirling flow
- Flame stabilization using a pilot flame
- Flame stabilization using a counter flow stabilizing technique
- Flame stabilization using a transverse flow

Another method of flame stabilization using an electric field has been reported by (Gulyaev et al. 1985), (Pedersen and Brown 1993) and (Yagodnikov and Voronetskii 1994). They found some interesting behavior of flames influenced by sub-breakdown electric fields, decreasing the ignition temperature and increasing the burning velocity. Their researches have stimulated interest in the effect of the plasma discharge generated by electric fields into the combustion research. This will be discussed in more details in section 1.5.3.

## 1.5.2 Laminar burning velocity

The laminar burning velocity ( $S_L$ ) is related to the rate at which the unburnt mixture is consumed in a propagating laminar flame. Laminar burning velocity is the most important fundamental property of premixed combustion. It is not only used for burner and engine designs, but also it has a great use in chemical reaction mechanisms validation and turbulent flame modeling. Accurate determination for the laminar burning velocity is constantly needed for combustion applications. So far, several techniques have been used for measuring the laminar burning velocity, and for a wide range of temperature, pressure, and fuels. Some of these techniques are the following;

**Bunsen flame method** The Bunsen flame method was used extensively for decades to determine the laminar burning velocity. In this method, the flame has a conical shape and stabilized on the burner rim. The average flame speed is calculated by dividing the volume flow rate of the mixture by the luminous cone surface area:

$$S_L = \frac{m}{\rho_u \cdot A_f}, \quad (1.1)$$

where  $S_L$  is the average burning velocity,  $m$  is the mass flow rate of the mixture,  $A_f$  is the flame total area which can be determined graphically. The flow needs to be a plug flow. It can also be determined by measuring the conical angle of the flame using  $S_L = V_u \cdot \sin\alpha$ , where  $V_u$  is the unburnt gas velocity at the burner inlet and  $\alpha$  is the half conical angle. Fig. 1.10 shows a schematic representation of the method. Accuracy of burning velocity determination by the Bunsen flame method is limited by the exit velocity profile and heat loss to the tube wall.

**Stagnation flame method** This method utilizes two identical nozzle-generated combustible flows facing each other to generate a stagnation flow field. By ignition, two symmetrical flat flames are located on the two sides of the stagnation plane, propagating away from one another. Combustion products exist in the region between the two flames. This configuration allows flame extinction to occur when the flames are pushed close together due to the high strain rates. The stagnation flame is a stretched flame, where the stretch intensity is represented by the velocity gradient ( $a = dv/dy$ ). The laminar burning velocity without stretching

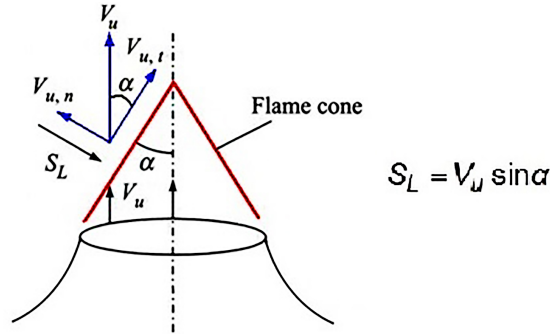


Figure 1.10: Determination of the laminar burning velocity using a Bunsen burner method.

can be determined by linear extrapolation to  $a = 0$  (Tien and Matalon 1991). Fig. 1.11 shows a schematic representation for the typical stagnation flame method.

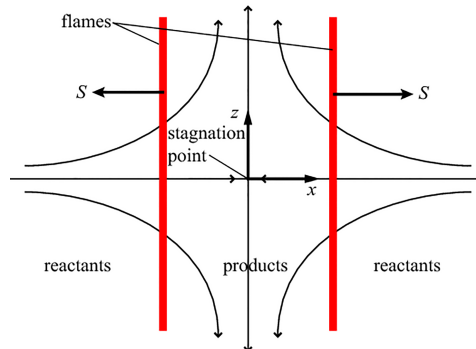


Figure 1.11: Schematic represents the typical stagnation flame method (Tien and Matalon 1991).

**Spherical flame method** The spherical flame area method comprises a freely propagating flame from spark ignition sources in initially quiescent gas mixtures. The oldest and most common method uses the pressure rise change in a closed vessel to calculate  $S_L$ . Another method utilizes high-speed images for the flame propagation. The images are analyzed to estimate flame size, consequently, the flame speed is derived from the variations of the flame size against the time elapsed. Following the linear relation between flame speed and flame stretch, the unstretched laminar burning velocities and corresponding Markstein lengths (the dependence of burning velocity on stretch) of laminar flames can be deduced. Fig. 1.12 shows a growing flame kernel images for stoichiometric mixtures for ethanol-air flame at atmospheric condition with a time interval of 4 ms (Liao et al. 2007).

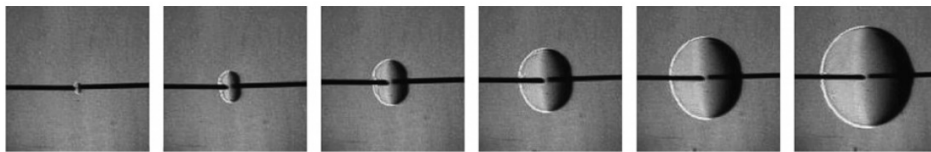


Figure 1.12: Determination of the laminar burning velocity using spherical flame method (Liao et al. 2007). The image shows the typical growing flame kernels for ethanol-air stoichiometric mixture at atmospheric condition. The time interval between the images is 4 ms.

**Heat flux method** Heat flux method was introduced by de Goey et al. (1993). It is considered as one of the most accurate methods for the laminar burning velocity determination as it uses one-dimensional adiabatic unstretched flame. The main idea of the heat flux method is the stabilization of a flat flame with the unburnt gas velocity so that the heat loss by the flame is compensated by the heat added to the unburnt gas. The heat flux by the flame is determined by the burner plate temperature profile. The adiabatic condition can be considered when the heat loss from the flame equals the heat gain to the burner plate. This adiabatic condition is difficult to achieve experimentally, but for the heat flux method this is possible. The gas velocity corresponding to the adiabatic condition, i.e. flat temperature profile, in this case represents the laminar burning velocity.

### 1.5.3 Plasma-Assisted Combustion (PAC)

The main roles of the plasma discharge in the combustion applications are generating heat, producing radicals and excited components, and modifying the transport processes. Plasma generates additional chemical reaction pathways for the fuel oxidation, which helps in flame stabilization, extending flammability limits, and increasing the flame luminosity. Additionally, the improvement of the flame stabilization facilitates burning of leaner mixtures, resulting in a reduction in thermally driven emissions, like  $\text{NO}_x$ , due to the reduction in the flame temperature.

The combustion performance can be improved by plasma discharges through several mechanisms. The weight of each mechanism is different, depending on; the type of plasma, i.e. thermal or non-thermal plasma, the type of fuel, i.e. light or heavy fuel, operating conditions, i.e. temperature and pressure, and others. Fig. 1.13 shows a schematic of the major enhancement mechanisms of plasma interaction with combustion (Ju and Sun 2015). These mechanisms can be summarized as follows;

- Thermal mechanism
- Kinetic mechanism



- Transport mechanism

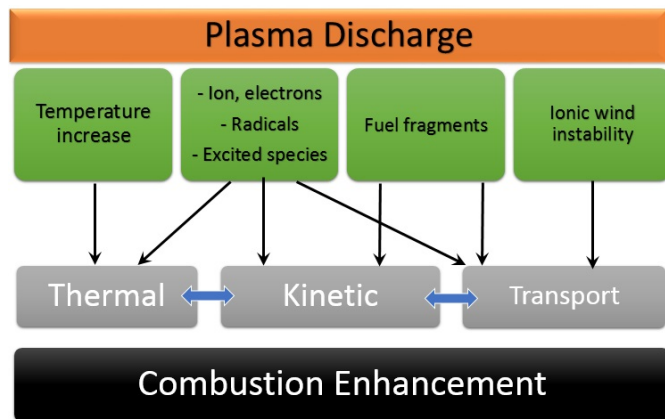


Figure 1.13: The main mechanisms responsible for combustion enhancement by plasma discharges.

The thermal mechanism is mainly driven by Joule heating and exothermic reactions. Joule heating is produced by passing the electric current through a gas between two electrodes. It is caused by interactions between charge carriers (electrons) and the ions and neutral molecules of the gas, giving them kinetic energy. While, the exothermic reactions are promoted by the highly energetic electrons and ions. Thermal plasma is often characterized by thermal equilibrium. Therefore, the temperatures of all energy levels (rotational, vibrational, and translation) and components (heavy molecules, electrons, ions, and radicals) are almost equal. The consumed energy is used to heat up the entire gas, like plasma torches, and the temperature is often in the range of 10,000- 100,000 K (10-100 electron volts (eV)). In non-thermal plasma, electron temperature is high (about 1 eV), while rotational excitation temperature, ion temperature, and heavy particle temperature are slightly above the room temperature. Although, the Joule heating in non-thermal plasma is not a significant mechanism compared to the thermal plasma, the minor rise in the gas temperature accelerates chemical reactions and fuel oxidation according to the Arrhenius law. This increases the burning velocity and flame stability.

The kinetic mechanism is motivated by highly energetic electrons and ions, which generate active radicals (e.g., O, OH, and H) via direct electron impact dissociation, ion impact and recombination dissociation (e.g.,  $O_2^+$  and  $N_2^+$ ), and collisional dissociations with electronically excited species (e.g.,  $N_2^*$ ,  $O_2(^1\Delta g)$  and  $CH_4^*$ ) and vibrationally excited (e.g.,  $N_{2(v)}$ ) molecules. These plasma-generated species and radicals behave like catalysts and participate in chain reactions that promote or accelerate reaction pathways.

The transport mechanism is influenced by the ionic wind (the momentum transfer from an electric field to the gas due to the space charge), ion and electron drift. Note that, these mechanisms are quite interdependent, which means that they are affecting each other in many ways. For example, the generated species can be responsible for some exothermic reactions which promote the thermal mechanism. At the same time, the higher the temperature, the stronger the plasma intensity, which in turn increases the radical species concentrations.

Several experimental and numerical investigations have been conducted to understand the role of plasma discharge on ignition; e.g. (Yin et al. 2013), (Kosarev et al. 2009), (Nagaraja et al. 2014) and (Cathey et al. 2007), flame stabilization and extinction; e.g. (Sun et al. 2013), (Pilla et al. 2006), (Michael et al. 2013), and (Li et al. 2013), and flame speed enhancement; e.g. (Ombrello et al. 2010) and (Nagaraja et al. 2015).

Several types of plasma discharges have been demonstrated as a promising way for combustion enhancement. Examples are filamentary discharge (Leonov et al. 2006), microwave discharge (Michael et al. 2013), gliding arc discharge (Ombrello et al. 2006), modulated streamer high frequency discharge (Klimov et al. 2004), and surface discharge (Shibkov et al. 2004).

Nanosecond pulsed discharge has received a considerable attention during the last decades due to the progress in the solid-state industry. Non-thermal discharges produced by pulsed power have been studied for various applications such as removal of hazardous environmental pollutants in gases, ozone generation, food processing, and medical applications. Enhancing the combustion and ignition performance is one of the potential applications for the nanosecond discharge due to the high energy efficiency and the significant radical production without excessive gas heating. Thanks to the very strong reduced electric field in a very short time period, which allows energy transfer mainly for electronic excitation and dissociation. Therefore, nanosecond discharge is a highly non-equilibrium process to enable a high electron temperature which results in a fast electron impact dissociation.

Many researchers have studied the nanosecond discharge kinetics and its effect on the combustion characteristics. They attributed the combustion enhancement to the significant radical production and the so-called 'fast gas heating' at the discharge region, e.g. (Mintoussov et al. 2011) and (Bak et al. 2011). More specifically, quenching reactions of the excited electronic state of the molecular oxygen. The weak bonds of the molecules are easy to break during the quenching process, generating energy responsible for raising the gas temperature. However, this process is pressure dependent: at low pressures, the role of the plasma-generated radicals is dominating and the temperature rise is negligible, while at high pressures, the plasma is in a filamentary mode where the gas heating is the responsible mechanism for the enhancement of burning rates.

Lean flammability limit studies have been performed for a turbulent premixed flame using a nanosecond repetitively pulsed plasma by (Pilla et al. 2006). They

placed the electrodes in the recirculation zone behind a bluff body as shown in Fig. 1.14a. Through spectroscopic measurements, an increase of the concentration of free radicals, namely O, H, and OH, inside the recirculation zone of the flame was noticed, which may explain the observed enhancement flammability limit, as shown in Fig. 1.14b.

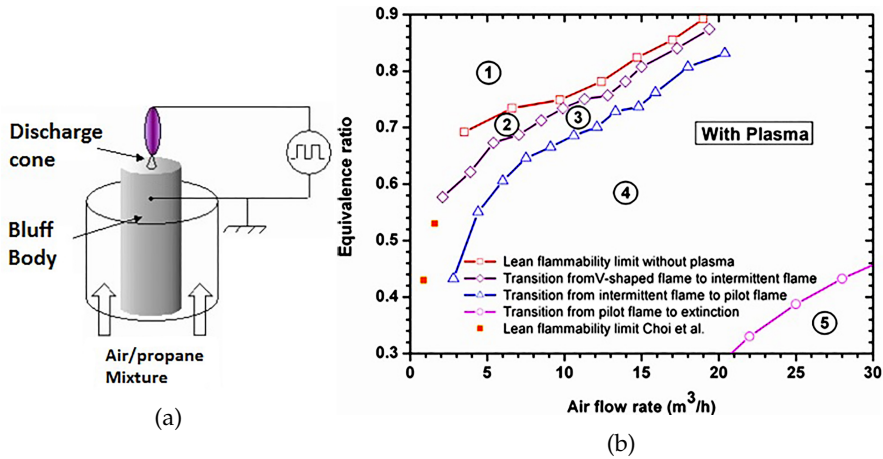


Figure 1.14: (a) Schematic for an experiment done by (Pilla et al. 2006) to study the effect of nanosecond pulsed plasma on the lean flammability limit for a turbulent flame, and (b) the flammability regimes with different plasma modes.

Despite the significant advancement in the last few years, many of the plasma-combustion interaction mechanisms remain unclear. The plasma/combustion reaction mechanisms are in preliminary phase and still need a lot of effort. The available mechanisms are not covering all plasma and fuel types and need extensive validations. The reaction cross section data are rare for most of the fuel reactions. Modeling of nanosecond plasma assisted combustion is very challenging and time consuming. Well understood fundamental experiments are needed to solve the coupling between flow, combustion, and plasma discharge. The results of these experiment can be used for better understanding and model validation.

## 1.6 Objective and Contribution

The objective of this research is to develop a better understanding of the effect of the nanosecond repetitively pulsed plasma discharge on the combustion characteristics of methane/air flames, in particular, flammability limit and burning velocity. To achieve this goal, we have developed a novel plasma reactor which employs pulsed DBD micro-discharges, and can act as a burner disk to stabilize premixed laminar flames. The main achievement of this design is that it can generate a stable plasma discharge at atmospheric pressure as well as low pressure

with a reasonable lifetime. This reactor is analyzed in detail and subsequently it is used to investigate the plasma-assisted combustion, burning velocity, flammability limits, etc. The following subjects are covered:

- The main thermal and electrical characteristics of the new DBD microplasma reactor (including current, voltage, pulse energy, reduced electric field, and others.)
- The effect of the nanosecond plasma discharge on the laminar burning velocity and flammability limits of lean premixed methane-air flame.
- A particle image velocimetry (PIV) study for inverted flames is implemented to determine the local effect of the plasma discharge on the burning velocity.

## 1.7 Outline of the Thesis

The thesis is organized into seven chapters. An introduction to plasma discharge and the plasma-assisted combustion is presented in this chapter.

Chapter 2 presents the new DBD microplasma device that is used to generate a non-thermal plasma discharge in micro channels of a perforated burner plate. The design philosophy, geometry and the manufacturing processes of the new device are presented in details. The potential applications of the device are also discussed.

Chapter 3 is mainly discussing the experimental setups that have been used in this study. The setups involve different electrical and optical instruments to analyze the plasma and flame characteristics. The optical emission spectroscopy setup as well as the high-speed imaging setup are described in detail. The methodology of error estimation in different physical quantities is covered as well.

Chapter 4 is devoted to describe the main characteristics of the plasma discharge in the DBD microplasma reactor for different operating pressures. The main electrical characteristics of the nanosecond pulse will be explored. The thermal properties, like rotational, and vibrational temperatures are determined by fitting the experimentally observed spectra of the second positive system (SPS) structure of  $N_2$  ( $C^3\Pi_u \rightarrow B^3\Sigma_g$ ) with the SPECAIR simulation tool. The reduced electric field is also determined using the intensity ratio of nitrogen spectral bands with high temporal and spatial resolution.

In Chapter 5, the enhancement of the combustion characteristics using the nanosecond plasma discharge will be discussed. Determine of the burning velocity using the conical flame area method will be presented. A parametric study based on the equivalence ratio, pulse repetition rate and plasma/flame power ratio will be discussed. Additionally, the blow-off limit with different plasma and flow conditions will be reported. The effect of the plasma discharge on NO<sub>x</sub> generation will be studied as well.

Chapter 6 covers an experiment using the particle image velocimetry (PIV) method to determine the local effect of the plasma discharge on the burning velocity using the stream-tube method.

The concluding remarks from this thesis and the recommendations for future works are outlined in Chapter 7.

## DBD Microplasma Reactor

---

---

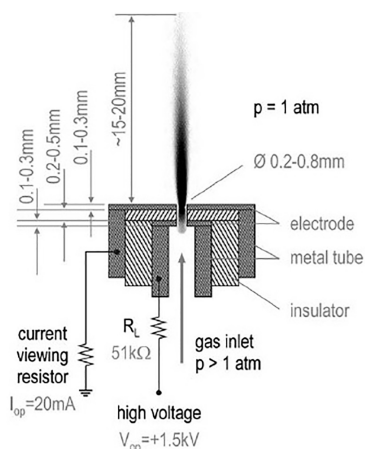
This chapter is devoted to introduce a new microplasma device that can be used to generate a non-thermal plasma discharge in micro channels. The design philosophy is based on the dielectric barrier discharge scheme driven by repetitive nanosecond pulses which can offer a highly efficient non-thermal plasma discharge at atmospheric pressure. The geometry, manufacturing processes and the main characteristics of the new device is presented. Some of the potential applications are also discussed. DBD microplasma device is the backbone of the approaches developed in the subsequent chapters.

---

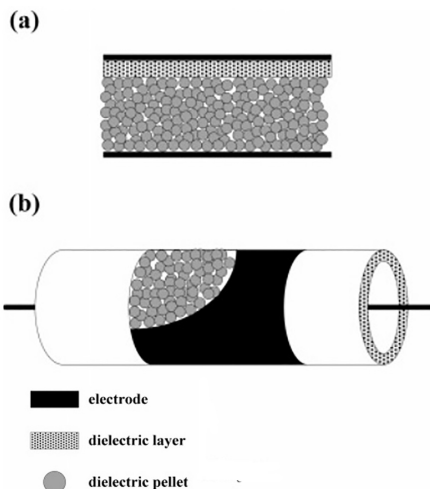
### 2.1 Introduction

Plasma flow reactors can be used to chemically process a gas. They are of interest because of their high energy efficiency and high selectivity. Therefore, they have a strong potential in applications like surface treatment (Shimizu et al. 2011), thin film deposition (Benedikt et al. 2007), detoxification of gaseous pollution (Shimizu et al. 2010, 2008), plasma medicine (Lee et al. 2009) and ozone generation (Hensel et al. 2009). Many different designs have been tested to generate a stable non-thermal plasma discharge in a flow reactor at pressures up to one atmosphere. Some of these designs, as shown in Fig. 2.1, are plasma jets (Kolb et al. 2008; Schutze et al. 1998), packed-bed plasma reactors (Chen et al. 2008b; Yu et al. 2012), pulsed-corona plasma reactors (Grabowski et al. 2007; Ono and Oda 2003; Winands et al. 2006) and atmospheric pressure glow discharges (APG) (Akitsu et al. 2005).

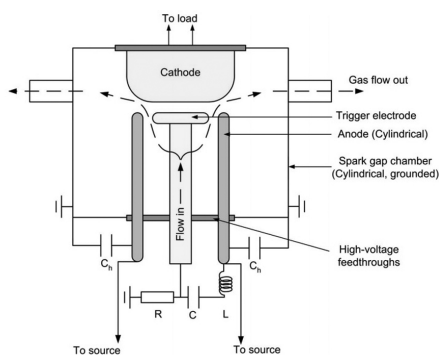
One of the most extensively studied configurations is an array of so-called microhollow cathode discharges (MHCD), which has the ability to produce a high-density plasma discharge in a relatively small volume (characteristic dimension



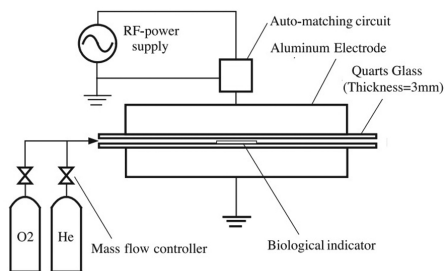
(a) Plasma jets (Kolb et al. 2008)



(b) packed-bed plasma reactors (Chen et al. 2008b)



(c) Corona plasma reactors (Winands et al. 2006)



(d) pulse-modulated RF-APG device (Akitsu et al. 2005)

Figure 2.1: Examples of plasma flow reactors

of about  $10^{-4}$  m) (Gomes et al. 2009; Karl et al. 1997; Schoenbach et al. 1996). Examples of the microhollow cathode discharge designs are given in Fig. 2.2. Compared to other types of flow reactors, MHCD ensures a maximum interaction between the plasma discharge and the processed gas. However, two conditions should be fulfilled to maintain a discharge in MHCD devices. Firstly, the applied voltage should exceed the breakdown voltage and be able to ignite the discharge for the given gas and pressure (Foest et al. 2006). Secondly, according to the Allis-White similarity law, the product of the pressure ( $p$ ) and the aperture diameter of the cathode ( $D$ ) should fall in the typical operating range for MHCD, which is 0.1-13 mbar·cm depending on gas, electrodes, and geometry (Becker et al. 2006).

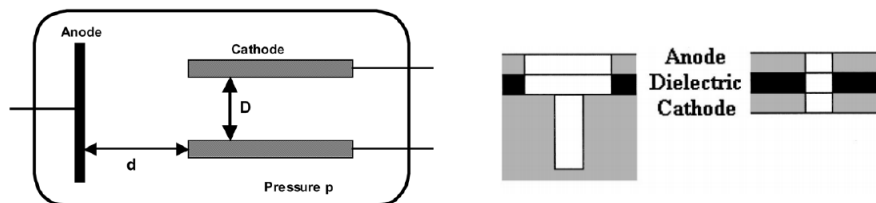


Figure 2.2: General diagram of a micro hollow cathode discharge device.

These conditions pose some constraints regarding scaling-up the diameter of the MHCD devices at high pressure. Based on the upper limit of the product ( $p \cdot D$ ), atmospheric pressure operation in air would lead to a maximum diameter ( $D$ ) of 100  $\mu\text{m}$ . However, in many applications, especially for gas treatment, it is desirable to increase the diameter to reduce the pressure drop for the same flow condition.

One of the most successful ways to increase the hole diameter of the reactor is by using a dielectric barrier discharge (DBD) (Papadakis et al. 2011; Sakai et al. 2005) driven by nanosecond high-voltage pulses. The surface discharge deposited by the (pulsed) discharge counteracts the applied field, thereby self-limiting the discharge. Together with the nanosecond pulses, this helps to generate a uniform discharge distribution and reduces the chance of glow to arc transition. In addition, nanosecond repetitive high-voltage pulses provide highly energetic electrons and more chemically excited species compared to AC power sources due to the rapid ionization process, with a power consumption that is about one order of magnitude lower (Zhang et al. 2013; Pai et al. 2009). The increase of the electron energy comes without a considerable increase of the gas temperature, thereby reducing undesired thermal effects of the plasma discharge on the treated gas.

In this chapter, we introduce a new geometry which utilizes the dielectric barrier discharge (DBD) method to sustain a non-thermal plasma discharge in an array of 400  $\mu\text{m}$  diameter channels perforating a 1.5 mm thick dielectric slab with embedded electrodes. The discharge is powered by nanosecond high-voltage pulses and is operated at pressures up to one atmosphere, which corresponds to a pressure ( $p$ ) times diameter ( $D$ ) of 40 mbar $\cdot\text{cm}$ . The main development in this study is that the high-voltage electrode is fully embedded within the dielectric substrate. This allows to generate a non-thermal plasma discharge at atmospheric pressure in channels larger than the maximum possible diameter for microhollow cathode discharges (MHCD) at the same pressure.

Although we are, successfully, able to increase the reactor hole diameters to be more than 100  $\mu\text{m}$ , but it is still can be considered as a microdischarge by definition. In principle, plasma can be considered as microdischarges if the characteristic length is smaller than 1 mm. Two features can be achieved by scaling down the hole diameter of the flow reactor.



- Scaling down of the plasma discharge usually is accompanied by increases in its power density.
- Plasma-flow interactions in microdischarges channels are more efficient than volume discharges.

## 2.2 Geometry design and material

As shown in Fig. 2.3, the new plasma device is a 1.5 mm thick dielectric slab perforated by a hexagonal array of 363 channels. The channels have a diameter  $d$  of 0.4 mm and a pitch  $p$  of 1.0 mm. The outer diameter of the reactor is 70 mm while the effective diameter of the flow area is 20 mm. The reactor geometry includes four layers of copper electrodes (A, B, C, and D). The high-voltage electrodes (B and C) are embedded into the dielectric material. The grounded electrodes (A and D) are located on the top and bottom surfaces of the reactor.

The outer and the inner copper layers have a diameter of 40 mm and 30 mm, respectively. All electrodes are perforated in the same hexagonal pattern as the dielectric, but the channels are twice as large as those in the dielectric. The device can work in two modes: single-layer discharge mode and double-layer discharge mode. In the single-layer discharge mode, only electrodes A and B are activated (see Fig. 3.7 for the equivalent circuit diagram) while electrodes C and D are kept floating. All the work presented in this study has been done in the single-layer discharge mode due to the deficiency of the power source to supply enough current to all the channels in both layers at the same time.

Cathode and anode are separated by a dielectric layer with a thickness of 0.36 mm. The outer (grounded) and inner (high-voltage) electrodes are made of copper with thicknesses of 18  $\mu\text{m}$  and 38  $\mu\text{m}$ , respectively. The separation distance between the two embedded electrodes is 0.6 mm, while the total thickness of the reactor is 1.5 mm. The width and thickness of the embedded electrodes have been calculated to safely withstand the peak current of the discharge pulses which is 40 A for a duration of 10 ns as it will be shown in Fig. 4.4a.

The formula for calculating the allowable current through the trace is published in the IPC-2221 standard section 6.2 as shown below.

$$I = k\Delta T^{0.44} A^{0.725} \quad (2.1)$$

where  $I$  is the current in Amps,  $k = 0.024$  for internal layers and  $k = 0.048$  for external layers,  $\Delta T$  is temperature rise in K, and  $A$  is the cross sectional area of the copper trace in  $\text{m}^2$ . The trace width can then be calculated by re-arranging this formula to determine the cross-sectional area that the desired current can safely pass through.

We came to this design by performing a geometrical parameter study to i) determine the minimum dielectric thickness in order to maximize the discharge

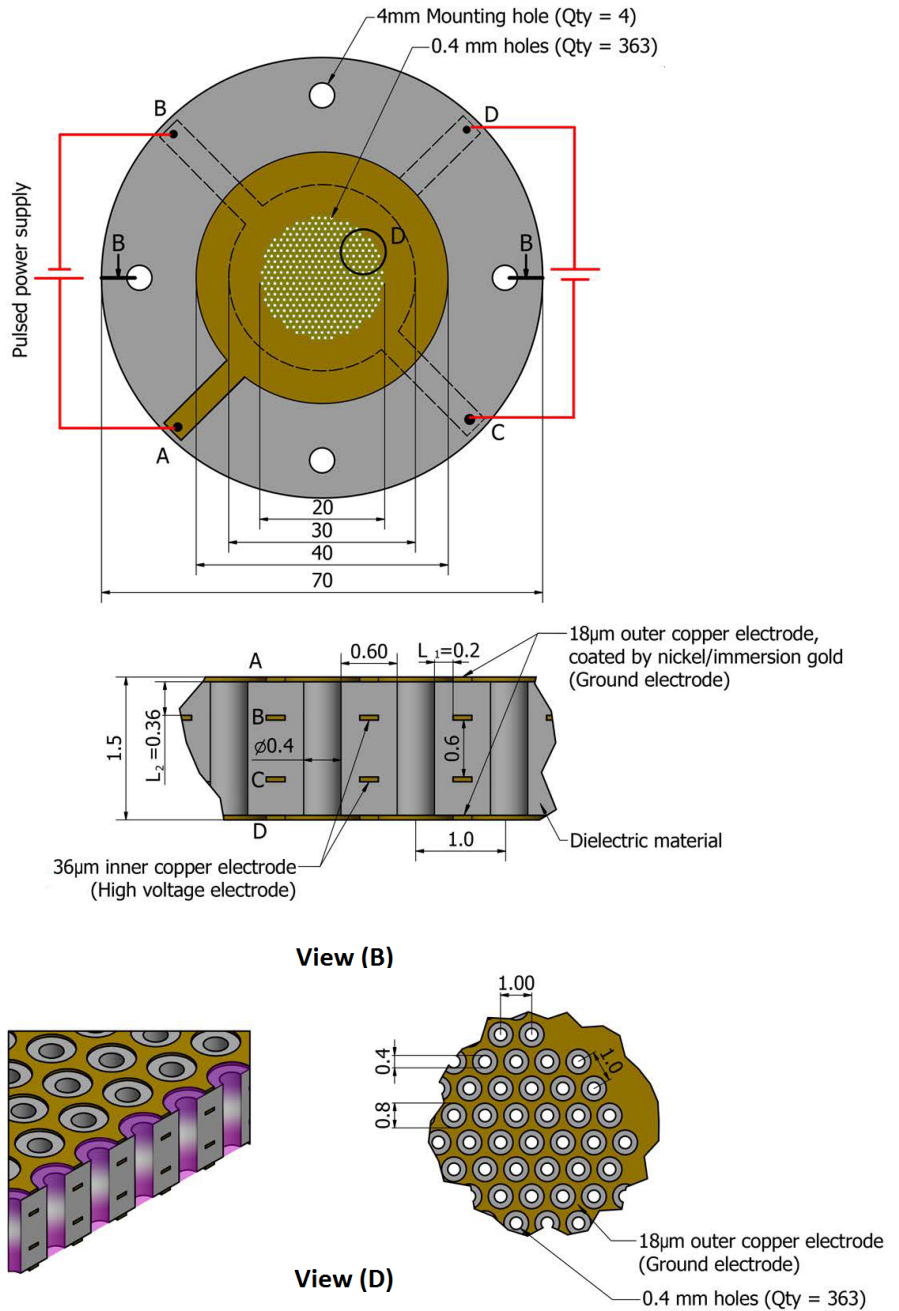


Figure 2.3: Schematic of reactor configuration [All dimensions are in mm].

strength, and ii) guide most of the discharge to the inside of the channels instead of the top or bottom reactor surfaces, to get an efficient interaction with the flowing gas. From this study, we found that the dielectric thickness between the anode and the wall of the hole, ( $L_1$  in view (B) of Fig. 2.3), should be less than the axial dielectric thickness between the anode and cathode ( $L_2$ ).

The dielectric material of the reactor is a composite of woven electrical grade fiberglass and epoxy resin. It has a dielectric constant  $D_r$  of  $4.17 \pm 0.05$  (at 1 GHz / 23 °C), a thermal conductivity of 0.4 W/m.K, a dielectric breakdown strength of 32 kV/mm, a thermal expansion coefficient of 14 ppm/°C and a glass transition temperature of 180 °C. This material has a stable performance over a wide range of frequencies and temperatures, as well as good machinability.

In order to reduce the chances of micro-filamentary discharges on the reactor surface, which would reduce the reactor lifetime as a result of excessive heating, the outer copper electrodes have been coated by a nickel/immersion gold layer which gives a surface roughness of 0.5  $\mu\text{m}$ . In some applications which are accompanied by thermal radiation, like plasma-assisted combustion or chemical vapour deposition, the copper layers also act as protective layers to conduct away excessive heat from the process. This prevents overheating of the dielectric material which can lead to dielectric failure. This overheating may come from the plasma discharge itself (Joule heating) or from the application, like the flame radiation in the plasma assisted combustion application.

## 2.3 Fabrication process

Due to the design complexity of the reactor and the need of accurate dimensions with a minimum tolerance, a special fabrication process, based on the photolithography technique<sup>1</sup>, has been applied. The fabrication process has three main steps;

- Converting the copper pattern into computer-aided manufacturing (CAM) features using special software called 'Eagle software'.
- Manufacturing process using the photolithography.
- Testing process.

Eagle is a CAD software developed by by CadSoft (<http://cadsoft.de>), and it is widely used for designing of electronic schematic and layout of printed circuit boards (PCB). It helps to accurately define each copper layer layout separately and

---

<sup>1</sup>Photolithography, also termed optical lithography or UV lithography, is a process used in micro-fabrication to pattern parts of a thin film or the bulk of a substrate. It uses light to transfer a geometric pattern from a photo-mask to a light-sensitive chemical "photo-resist", on the substrate. A series of chemical treatments then either engraves the exposure pattern into, or enables deposition of a new material in the desired pattern upon the material underneath the photo-resist.

to define the channels size and location. The software produces 'Gerber' layout files as well as 'Excellon' drill files, which are the standard file formats accepted by PCB fabrication machines.

The entire manufacturing process of the reactor is done in a temperature and humidity-controlled darkroom environment to ensure the accuracy of the copper lines. The process starts by converting each copper layer into a pixel image film, which called the '*photo tool*', using a laser photoplotter.

To produce the inner layers of our multilayer device, it starts with a panel of a dielectric slab with copper layers pre-bonded onto each side, see Fig. 2.4a. The panels are coated with a photo-resistive film as shown in Fig. 2.4b, this process happens in a clean room to make sure that no dust gets onto the surface where it could cause a short or open circuit on the finished device. The bed of the printer has registration pins matching the holes in the photo tools and in the panel. The first film is loaded onto the pins, then the coated panel, and the second film afterward. The pins ensure that the top and bottom layers are precisely aligned. A powerful UV lamps is used to harden the photo-resist through the clear film to define the copper pattern.

Outside the clean room the panel is sprayed with a powerful alkali solution which dissolve (or etch away) the exposed copper from the inner layer, see Fig. 2.4e. The panel is pressure-washed and dried. The desired copper pattern is now covered by the hardened resist. The process is carefully controlled to ensure that the finished conductor width is exactly as designed. Next, we strip off the photo-resist which protect the copper image to get the exact required pattern, see Fig.2.4f.

The outer layers of our multilayer device consist of sheets of fiberglass pre-impregnated with uncured epoxy resin (prepreg) and a thin copper foil. We lay-up a copper layer, a layer of prepreg, the pre-treated core, another prepreg, and copper layer, see Fig. 2.4g. Then, we press them together using a bonding press. This press uses heated press plates and pressure to bond the layers of the device together. The heat melts and cures the epoxy resin in the prepreg while the pressure bonds the device together, see Fig. 2.4h.

After that, the channels are drilled by a laser drilling machine to ensure clean hole walls and a uniform pattern, see Fig. 2.4i. Once we drilled the channels, we repeat the imaging process (pixel image film, photo resist, but for the outer layers to get the outer copper tracks, see Fig. 2.4j). To enhance the surface roughness, a nickel layer is chemically deposited onto the copper and then a thin layer of gold is coated over the nickel. At the end of the device production process, we electrically test every layer against the original design by using a flying probe tester to assure the absence of any open circuit in each layer or short circuit between the layers.

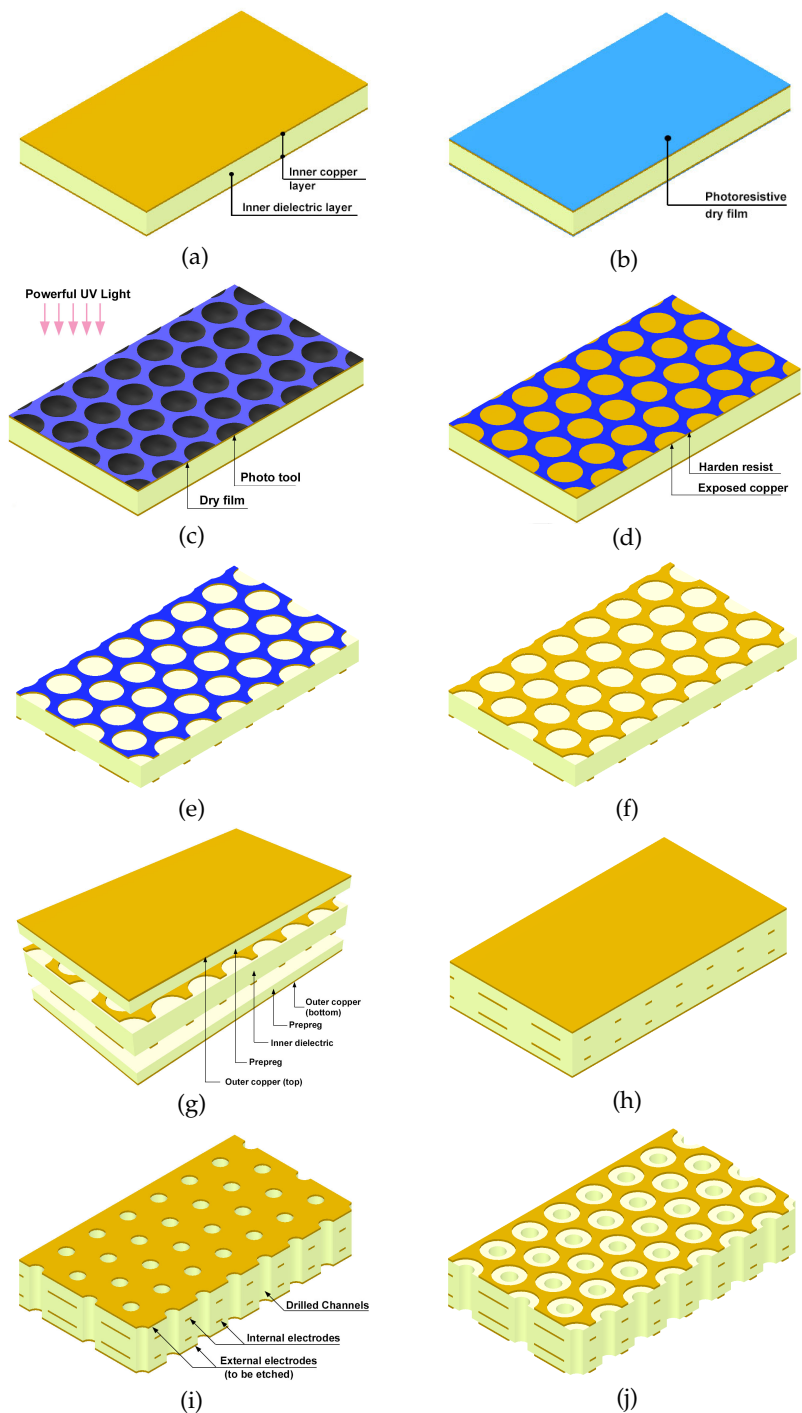


Figure 2.4: Manufacturing processes of the DBD microplasma reactor.

Fig. 2.5 shows an image for the DBD microplasma reactor after a complete manufacturing process. Fig. 2.6 shows a natural luminosity top view image of a plasma discharge in this DBD microplasma reactor, with 3.4 l/min air flow upwards, out of the plane of the paper, at atmospheric pressure, 5 kV voltage pulse with a repetition rate of 3 kHz, recorded by a common DSLR camera (Nikon D5100). Note that the plasma is attached to the walls of the microchannels, not in the center of the holes.

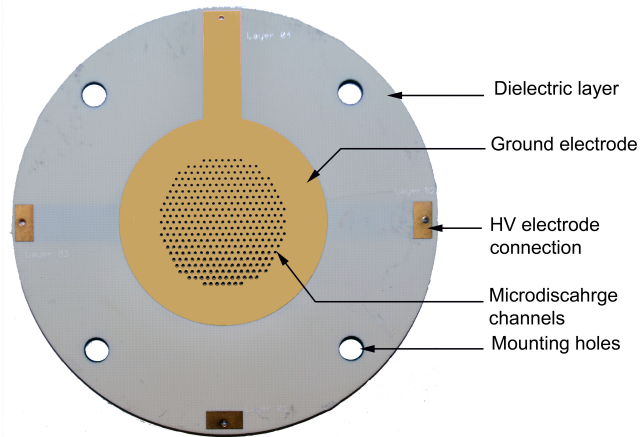


Figure 2.5: Image of the DBD microplasma reactor. The embedded electrodes configuration is shown in Fig. 2.3.

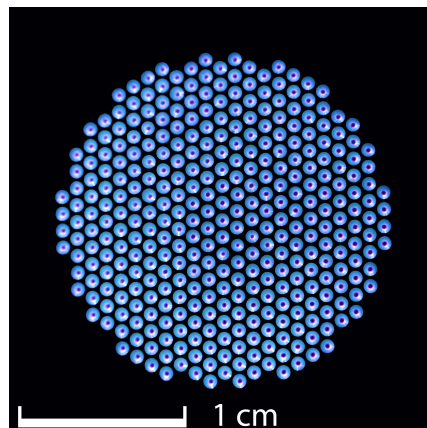


Figure 2.6: Image of the plasma discharge in the DBD microplasma reactor (see Fig. 2.3 for details) in air with a flow rate of 3.4 l/min at atmospheric pressure and a pulse repetition frequency of 3 kHz, exposure time: 1/20 sec.

## 2.4 Reactor lifetime

One of the serious problems of microplasma devices is their often short lifetime due to surface and internal damages. This is due to the frequent loss of plasma confinement due to vaporization and ablation, which cause significant surface erosion and structural failure (Felix et al. 2016; Hassanein and Konkashbaev 1998). Reactor lifetime is very sensitive to many parameters, e.g. geometry, material of the dielectric and power source.

The device can be damaged when a complete surface erosion happens in one single spot, see Fig.2.7. This allows for a spark to propagate between the two electrodes at this spot only. After that, a uniform plasma no longer ignites throughout the other channels.

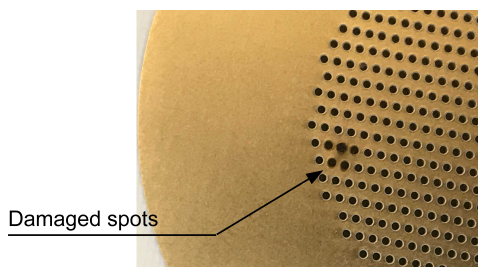


Figure 2.7: Image shows a damaged reactor. The black spot is due to a spark resulting from a dielectric erosion in this channel.

The lifetime of the reactor is investigated by measuring the time to breakdown at various frequencies and operating pressures. Fig. 2.8 shows the dependence of the reactor lifetime on the pulse repetition frequency at atmospheric pressure and 50 mbar. At a frequency of 2 kHz and atmospheric pressure, the reactor lifetime was about 24 minutes in continuous operation mode. While at 100 mbar, it was about 103 minutes. This shows an enhancement in the reactor lifetime of about four times by lowering the operating pressure by a factor of 20. This enhancement increases to a factor of about ten at a pulse repetition rate of 10 kHz, even though the lifetime itself decreases in both cases.

Two factors may contribute to the observed enhancement. Firstly, at low pressure, the ion impact frequency is minimal, which slows down the dielectric wear down process. Secondly, at low pressure the gas temperature is lower as will be shown in Section 4.5.1. Both reasons make the reactor more prone to failure at atmospheric pressure due to thermal stress on the internal structure of the dielectric material. Additional factors that may affect the lifetime of the reactor and need more investigation are voltage amplitude and duration, geometry, reactor material and operating gas.

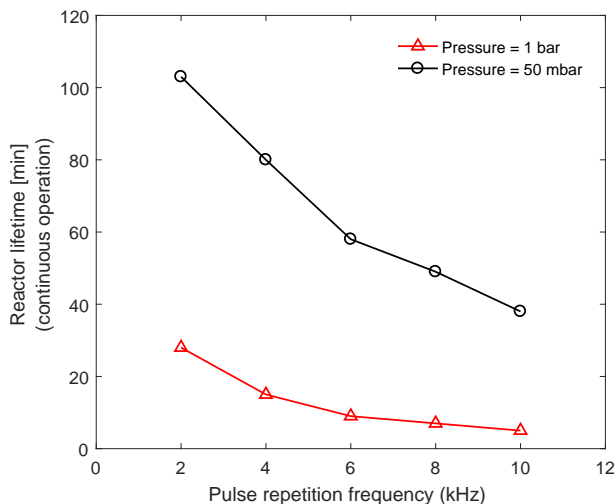


Figure 2.8: Reactor lifetime in continuous operation mode as function of pulse repetition frequency at atmospheric pressure (black line) and 50 mbar (red line). Both are for stagnant air and plasma voltage of 5 kV.

## 2.5 Potential applications of the DBD microplasma reactor

The unique physical and chemical properties caused by the increased surface-to-volume ratio and the decreased electrode spacing are the main reasons that make DBD microplasma reactor particularly suitable for many practical applications. In this section, we will point out some of these applications.

### 2.5.1 Flow reactor

Driven by the high energy efficiency and high chemical selectivity of the plasma discharge, plasma flow reactors are a very rich branch in plasma science. Here are some examples where our DBD microplasma reactor can be applied to;

- Ozone production
- CO<sub>2</sub> to CO conversion
- Chemical vapor deposition



## 2.5.2 Wounds and skin treatment

Plasma biology is a relatively new and rapidly growing field of non-thermal plasma science. Recently, non-thermal plasma has been applied in treatment of living tissues (Shashurin et al. 2008), sterilization and healing of wounds, and skin diseases (Weltmann et al. 2012). Non-thermal atmospheric pressure plasma is highly effective in deactivation of micro-organisms. Atmospheric pressure non-thermal discharge in air provides a high density of strongly reactive oxidizing species able to kill micro-organisms without any considerable heating effect.

Figure 2.9 shows that we can apply safely and directly a 5 kV non-thermal pulsed plasma discharge from our DBD microplasma reactor to human skin. This provides an opportunity for our new non-thermal plasma flow device to efficiently interact with skin diseases and wounds treatment. More investigations on this topic are needed and should be made in-line with medical safety regulations.

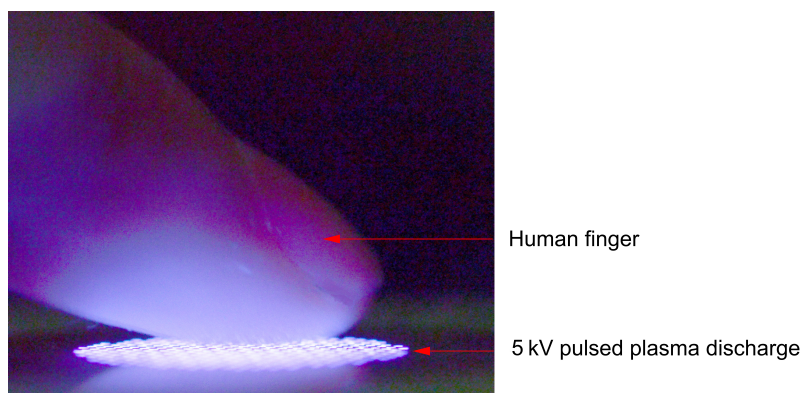


Figure 2.9: Image of a human finger safely touching a 5 kV DBD microplasma nanosecond discharge with a pulse repetition rate of 3 kHz.

## 2.5.3 Plasma assisted combustion

As mentioned in Chapter 1, plasma produces radicals and species which may have a contribution to actively control the combustion stability. In this thesis, we will use the DBD microplasma reactor as a burner platform, to study the combustion enhancement mechanisms by using plasma discharge. Figure 2.10 shows a methane-air flame at atmospheric pressure produced by the DBD microplasma burner. The plasma is powered by repetitively nanosecond high-voltage pulses.

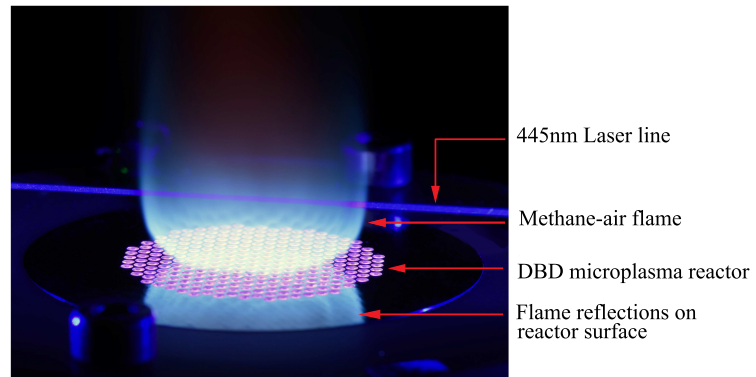


Figure 2.10: Image of DBD microplasma burner.

## 2.6 Summary

A novel DBD microplasma reactor has been developed. The geometry and manufacturing process has been presented. By this design, we were able to sustain a non-equilibrium plasma discharge in a pattern of  $400 \mu\text{m}$  diameter channels at pressures up to 1 bar. The DBD microplasma flow reactor is a promising device for a wide range of applications that require an efficient interaction between a non-thermal plasma discharge and a gas flow. A reactor lifetime study showed around 100 minutes lifetime at low pressure. Nevertheless, more effort is needed in order to increase the lifetime of the reactor in order to transfer it to real applications.



## Experimental setup

---

---

In this chapter, we describe the main components of the experimental setups. The setups allow to examine both the plasma discharge characteristics in the DBD microplasma reactor as well as the combustion characteristics. The setups are designed to work under different operating pressures, from atmospheric pressure down to 50 mbar. A detailed description of the optical emission spectroscopy setup, which is used to study the main features of the nanosecond pulses, is presented. This chapter also contains the methodology of the error estimation for the different physical quantities under investigation.

---

### 3.1 Introduction

As presented in Chapter 2, a new DBD microplasma device has been developed. It is important to study the main electrical and thermal characteristics of the plasma discharge generated by this device. In this chapter, two experimental facilities are described. Both of them utilize the DBD microplasma reactor as the plasma source. The first facility is designed to provide an optical access to the plasma discharge inside the DBD microplasma reactor, which allows to examine the temporal and spatial distribution plasma inside the channels. The second facility is designed as a burner platform to study the effect of the plasma discharge on the combustion enhancement of methane-air premixed flame. These facilities are developed to work under different operating pressures and both provide optical access to the plasma discharge as well as the flame.

Due to the high electromagnetic noise, generated by the nanosecond high-voltage discharge, intrusive measuring techniques have a limited use in our setups. Therefore, a number of optical and laser diagnostic techniques have been employed to study the plasma characteristics and the plasma-flame interaction

mechanism. In the subsequent sections, we will present these techniques in details.

This chapter gives an overview of the experimental setups used in the studies. In Section 3.2 we present the main components used to provide a uniform flow of air and methane mixture toward the plasma reactor. Section 3.3 describes the electrical components used to generate the nanosecond discharge as well as the measuring devices for the electrical parameters. In Section 3.4 and 3.5, we aim to provide the details of the optical emission spectroscopy and the high-speed imaging setup to some extent. Finally, Section 3.6 shows the methods used to calculate the uncertainties associated with the measurement of the different physical quantities used in this study.

## 3.2 Experimental setup

A schematic representation of the experimental setup is shown in Fig. 3.1. The setup consists of four main parts;

- Plenum chamber.
- Water Jacket.
- DBD microplasma reactor.
- Vacuum chamber.

The plenum chamber and the water jacket are made of steel and brass respectively. The purpose of these parts is to create a uniform air/mixture flow towards the plasma reactor. The gas inlet/outlet port is located at 25 mm from the bottom of the plenum chamber. A perforated plate, located at 40 mm from the bottom, works as a flow straightener. The holes in the perforated plate have a 1.0 mm diameter and 2.0 mm pitch, and they cover the entire area of the plate, see Fig. 3.2.

The reactor temperature is controlled by means of a hot-water jacket underneath the reactor, see Fig. 3.3. The inner surface of the water jacket is tapered to provide a gradual variation in the gas velocity toward the reactor/burner. The water is heated by an electric heater and a thermostat to control the water temperature. The water circuit can heat up and control the upper surface of the reactor up to 80 °C.

In case of reduced pressure, two vacuum chambers have been used alternately. One is used to give an optical access to the channels from the top plane, see Fig. 3.5. It is 20 mm in height and 60 mm in diameter, and is mounted on top of the plasma reactor. The top flange of the chamber includes a fused quartz window

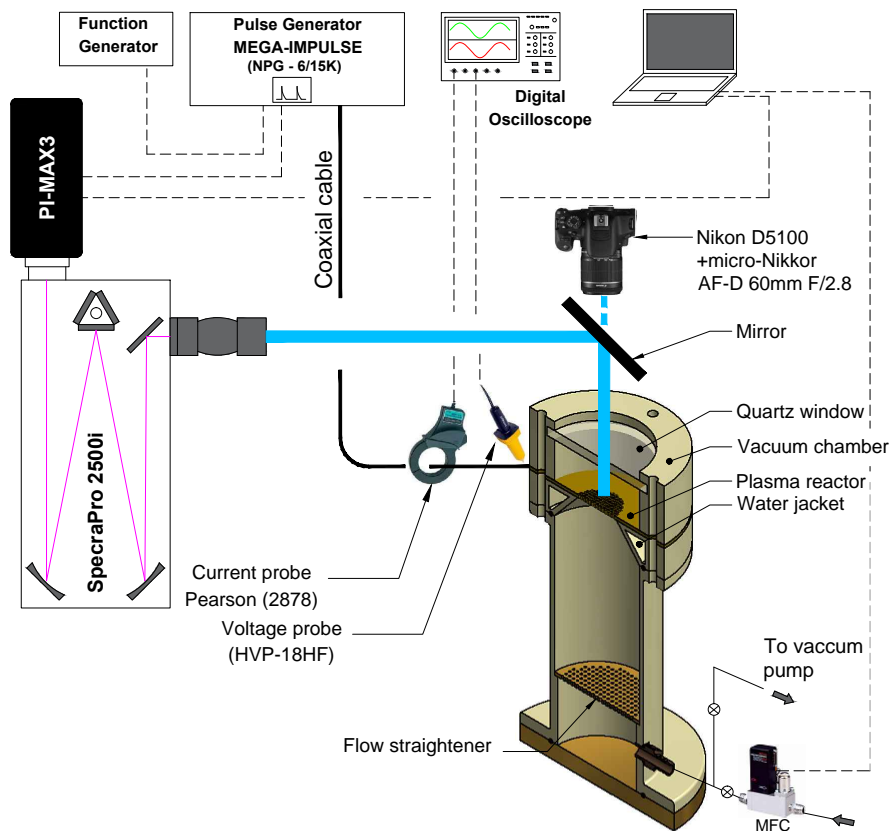


Figure 3.1: Schematic of the experimental setup.

with a thickness of 4 mm, through which the discharge optical emission can be viewed.

The second chamber is used to confine the flame in case of combustion, as shown in Fig. 3.6. It consists of a cylindrical quartz tube with a height of 100 mm, 40 mm external diameter and thickness of 4 mm. The top flange has two openings. The first opening has a diameter of 8 mm and is used to exhaust the combustion product by a vacuum pump, in the reduced pressure experiments. A manual needle valve is used to control the pressure inside the chamber. A buffer vessel is installed between the vacuum pump and the needle valve to damp any fluctuations generated by the vacuum pump. The second opening has a diameter of 10 mm, and is used to place a spark plug for flame ignition. Two high-temperature o-rings are used to prevent leakage between the quartz cylinder and the top and bottom flanges. Four 4 mm threaded bolts are used to connect the top flange and burner body.

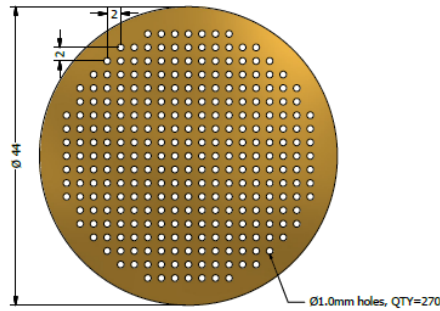


Figure 3.2: Schematic of the flow straightener

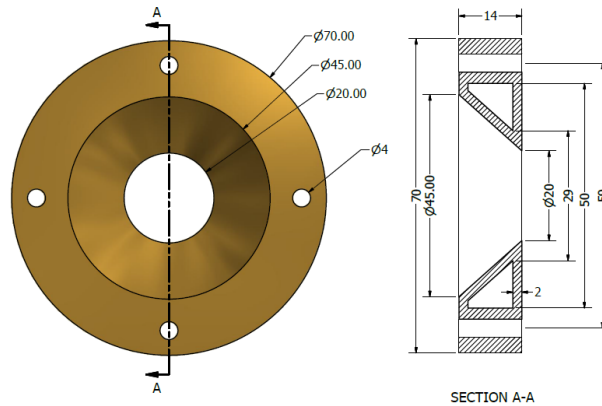


Figure 3.3

Figure 3.4: Schematic of the water jacket.

The air and fuel flow rates are controlled by Bronkhorst mass flow controllers (MFC's). A cylindrical buffer vessel is placed before the MFC's to damp pressure fluctuations. The MFC's are connected to the computer via a RS232 serial cable and are controlled by Bronkhorst software. In addition, an air filter is installed just before the MFC to avoid impurities. To further ensure purity, synthetic air of grade 4.0 has been used.

A vacuum pump model Busch R5 KB 0010, with a minimum pressure of 2 mbar and flow of  $10 \text{ m}^3/\text{h}$ , has been used to evacuate the vacuum chamber to the desired pressure. A shell and tube heat exchanger, cooled by water, was used to cool down the exhaust before entering the vacuum pump. Additionally, a buffer vessel with a volume of  $0.2 \text{ m}^3$  has been placed between the vacuum pump and the exhaust outlet to absorb any fluctuations generated by the vacuum pump. A manual needle valve is used to control the pressure inside the chamber. The

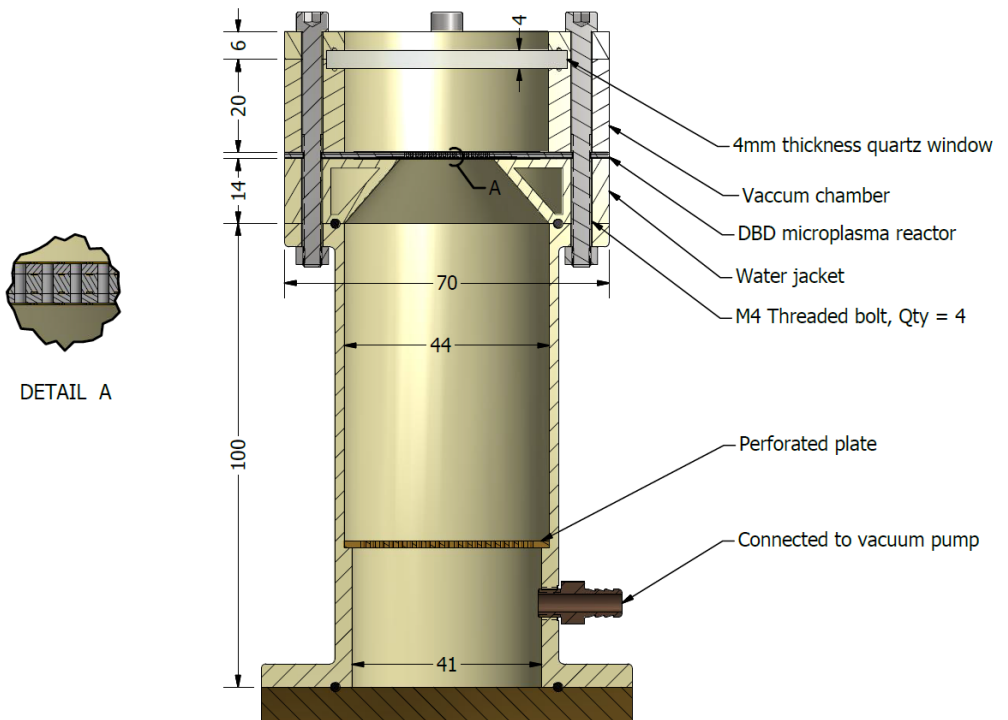


Figure 3.5: Detailed drawing for the setup used for plasma characteristics measurements (all dimensions are in mm).



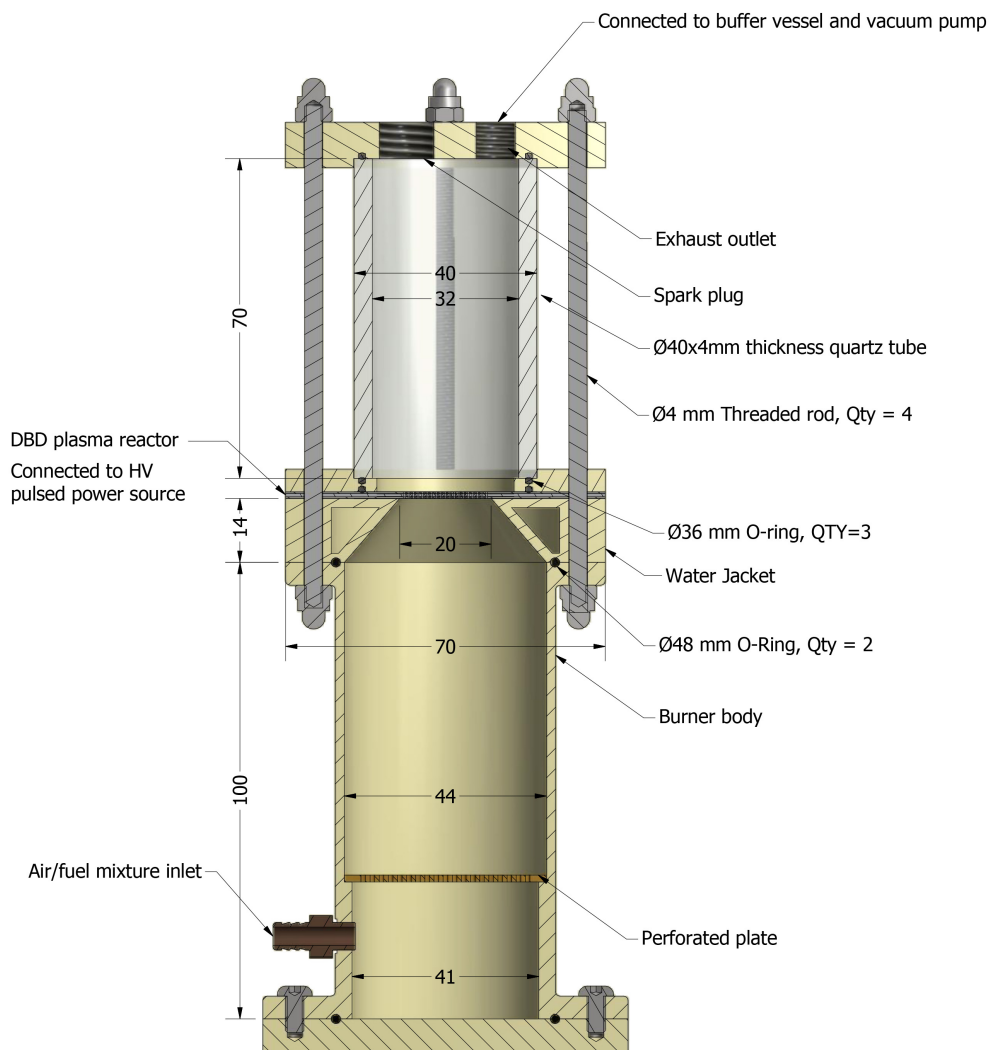


Figure 3.6: Detailed drawing for the burner configuration (all dimensions are in mm).

pressure is monitored by a piezo-resistive digital pressure gauge model PG100 mounted directly on the inlet pipe.

### 3.3 Electrical setup

Fig. 3.7 shows the equivalent electrical circuit diagram as used with single-layer operation (red box) and double-layer operation (blue box) for the DBD microplasma reactor. In case of double-layer operation, the total voltage  $V_{(t)}$  is the same for the two layers, while the current is divided evenly between the two layers. When the voltage exceeds the breakdown voltage, indicated as an ignition switch in the figure, the current  $I_D$  passes through the discharge gap to initiate the plasma discharge.

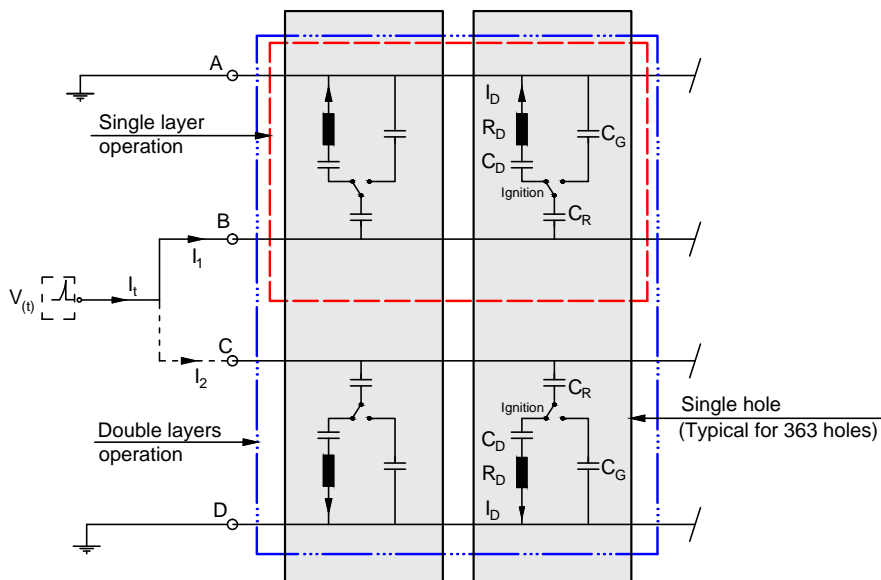


Figure 3.7: Equivalent electrical circuit diagram for single-layer operation (red box) and double-layer operation (blue box). For connections A, B, C and D, refer to Fig. 2.3.  $C_R$  is the reactor capacitance,  $C_G$  is the air gap capacitance,  $R_D$  and  $C_D$  are the resistance and capacitance of the discharge, respectively. For illustration purposes, only 2 of the 363 holes are drawn.

The high-voltage pulses are produced by a Mega-Impulse semiconductor-based pulse generator model NPG-6/15k, see Fig.3.8. Positive polarity pulses of 4 - 6 kV

in amplitude, 25 ns in duration and 10 ns of rise time are created at a pulse repetition frequency in the range of 0-10 kHz. The pulse generator can be internally or externally triggered. In case of external triggering, a 100 ns triggering pulse is applied to the 'SYNC IN' connector by a coaxial cable with a 50  $\Omega$  impedance. The external triggering is achieved by a FeelTech frequency generator model FY2102S. Unfortunately, dielectric barrier discharge loads have a high nonlinear nature and some reflection of energy inevitably occurs, see Zhang et al. (2017). The generator is protected against the overheating resulting from reflected energy.

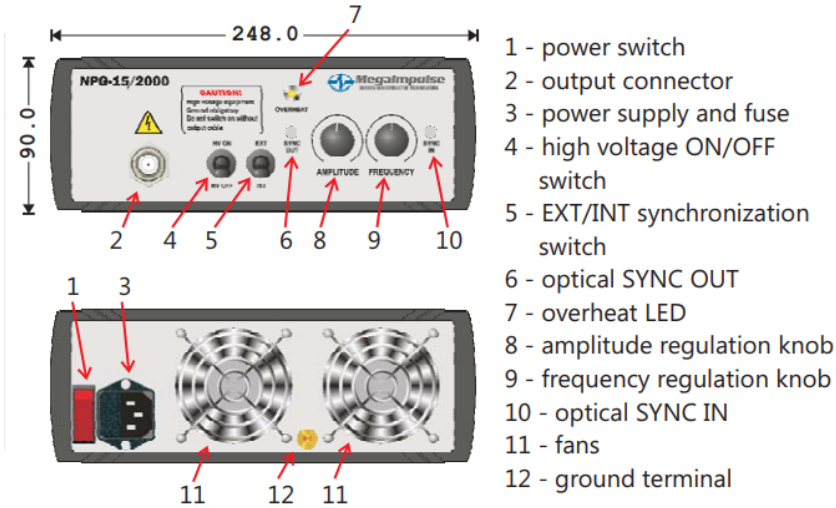


Figure 3.8: Nanosecond high-voltage pulse generator.

Voltage and current are simultaneously monitored by a Lecroy waverunner 44MXi-A oscilloscope with an analog bandwidth of 400 MHz and a sampling rate of 5 GS/s. The voltage signal is measured by a North Star high-voltage probe model PVM-4 with a sensitivity of 1 V/1 kV, a bandwidth of 120 MHz and 2 ns rise time. The probe is placed between the reactor terminals. The current through the electrodes is measured by a Bergoz current transformer model CT-F0.5 with a 1.75 ns rise time and a sensitivity of 0.5 V/A voltage-to-current conversion. The current coil is placed around the grounded cable just after the reactor. The current probe cable length is matched with the cable length of the voltage probe to eliminate any delay between the two signals which leads to a significant error in the pulse energy calculation, this point will be discussed in more detail in section 4.2.

The reciprocal of the effective capacitance of the external circuit  $C_{\text{total}}$  is the sum of the reciprocal of two components; the reactor capacitance  $C_R$  and the cable capacitance  $C_{\text{cable}}$ . Both the reactor and cable capacitances have been measured by a Fluke RCL meter model PM6303, resulting in  $C_R = 94$  pF and  $C_{\text{cable}} = 200$  pF. So, the equivalent total capacitance is  $C_{\text{total}} = 64$  pF.

## 3.4 Optical emission spectroscopic setup

Optical emission spectroscopy has been performed with a SpectraPro 2500i spectrometer with a focal distance of 0.5 m, fitted with three gratings of 300, 1800 and 3600 grooves/mm. The emission spectra from the plasma discharge have been recorded using a 1024 x 1024 pixels ICCD camera model Princeton Instruments PIMax 3, located at the exit port of the spectrograph. A UV-Nikkor lens with 105 mm focal length and f/4.5 is attached to the spectrometer entrance slit to collect the emitted light from the plasma discharge.

### 3.4.1 Wavelength calibration

The spectral sensitivity of the entire optical system is wavelength-calibrated using a low-pressure pencil type mercury lamp Sansonetti et al. (1996), model ORIEL 6035. This lamp provides a group of well defined spectra lines to determine the spectral sensitivity of the system and the apparatus profile. The 253.65, 435.83 and 579.07 nm spectra lines have been used to cover the measuring range. During the calibration process, the lamp is placed 20 cm away from the front of the spectrograph. Three steps are required to perform the calibration process correctly:

- Offset: to adjust the peak to be exactly in the center of the array.
- Adjust: to adjust other wavelengths which may still be improperly calibrated.
- Dispersion: to calibrate the wavelength scaling so that peaks on the far left or the far right in the window are also accurately calibrated.

### 3.4.2 Apparatus function

The apparatus function is the intensity distribution function in the output plane of a spectroscopic system assuming the input to be an ideal sharp isolated spectral line. A 355 nm spectrum line of a Dye laser has been used to measure the apparatus function of the spectroscopic system. Fig. 3.9 shows the apparatus function of the system for 300, 1800 and 3600 grooves/mm gratings for a 20  $\mu\text{m}$  wide slit. Table 3.1 shows the blaze wavelengths and the equivalent full widths at half maximum (FWHM) of the apparatus functions (approximately Gaussian shapes).

Synchronization between the voltage pulses signal and the ICCD camera gate was achieved by a triggering signal from the high-voltage pulse generator which was adjusted by the internal delay generator of the ICCD camera. A 200 ns time delay has been observed between the rising edge of the high-voltage pulse and

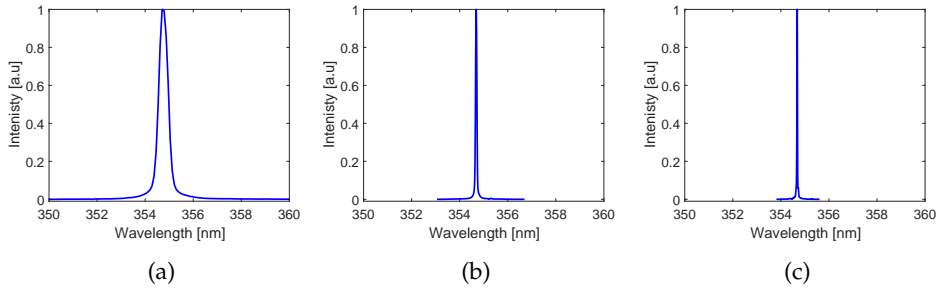


Figure 3.9: 355 nm line broadening at 20  $\mu\text{m}$  slit width for (a) 300 grooves/mm grating, (b) 1800 grooves/mm grating, and (c) 3600 grooves/mm grating.

Table 3.1: Blaze wavelength and equivalent FWHM of the apparatus function for a 20  $\mu\text{m}$  wide slit of the gratings used in this experiment.

	Grating (grooves/mm)		
	300	1800	3600
Blaze wavelength [nm]	300	200	300
FWHM [nm]	0.58	0.084	0.037

the onset of the plasma discharge. This time delay comes from many sources: (1) the high-voltage pulse generator delay, (2) signal delay due to 3 meters cable length, (3) the charging of the reactor capacitance, (4) the camera internal delay, and (5) the time light takes from the discharge to the camera (about 1 ns / 30 cm). The digital images have been recorded using a commercial 16.2 mega-pixel digital camera Nikon D5100 fitted with a micro-Nikkor lens with a 60 mm focal length and  $f/2.8$ .

### 3.5 High-speed imaging setup

A high-speed camera model FASTCAM Mini UX100 camera fitted with an Invisible vision intensifier model UVi 1850-05 is used to capture the plasma discharge for a single high-voltage pulse. Table 3.2 shows the specification of the camera and intensifier system. Synchronization between the image intensifier and the high-voltage pulses was achieved by a BNC-575 pulse-delay generator. Fig. 3.10 shows the setup used for the high-speed imaging of the plasma discharge in the microplasma reactor.

Table 3.2: Specification of the high-speed image system.

	Specification
Camera	FASTCAM Mini UX100
Image sensor	12-bit ADC
Maximum resolution	1,280 × 1,024 pixel
Minimum frame Rate <sup>(1)</sup>	4000 fps
Maximum frame Rate <sup>(2)</sup>	800,000 fps
Minimum shutter speed	1 $\mu$ s
Sensitivity	ISO 10,000
Objective lens	60 mm NIKKOR micro lens
Intensifier	Invisible vision model UVi 1850-05

<sup>(1)</sup> At a resolution of 1280 × 1024 pixel

<sup>(2)</sup> At a resolution of 1280 × 8 pixel

### 3.6 Error estimation

There are many sources of errors in the measuring of any physical quantity. Experimental errors are commonly divided into two main groups:

- Systematic errors.
- Random errors.

Common sources of systematic errors are faulty calibration of measuring instruments, poorly maintained instruments, or faulty reading of instruments by the user. On the other hand, random errors are statistical fluctuations in the measured data due to the precision limitations of the measuring device. Random errors cannot be easily avoided, but can be reduced by averaging the fluctuated signal over a large number of observations.

In our experiments, we are dealing with many physical quantities which encounter different sources of uncertainties. Some of these quantities are:

- Mass flow rate.
- Equivalence ratio.
- Pressure.
- Temperature.
- Current and voltage.

The mass flow rate is measured by the mass flow controller (MFC) manufactured by Bronkhorst. The accuracy of the mass flow controllers is  $\pm 0.1\%$  of the full

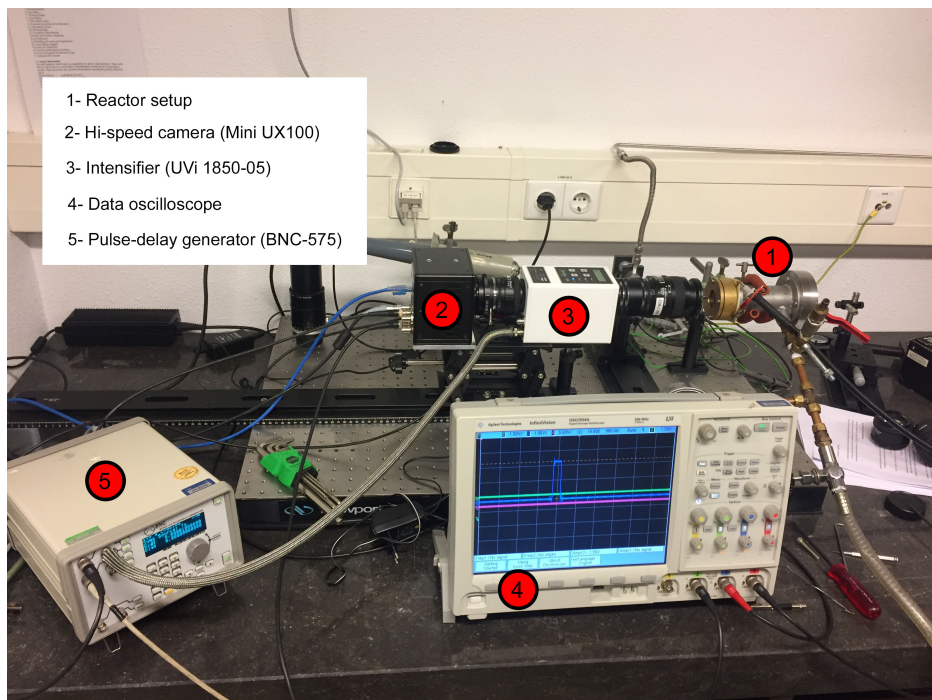


Figure 3.10: High-speed imaging setup.

scale reading plus  $\pm 0.5\%$  of the reading value. This value increases at flow rates less than 10% of the maximum allowable flow rate. The MFC's have been calibrated on a regular basis using the 'Flow Piston Prover' calibration setup, Bosschaart (2002). Also, in the same thesis, a pressure dependent study has been performed to study the dependence of the mass flow rate on the pressure. It has been found that a 0.08% variation of the mass flow rate by 1 bar change in the pressure (which is the maximum pressure difference in our low pressure experiment). Therefore, it has been concluded that the effect of the pressure on mass flow calculation can be safely neglected during the low pressure experiment.

Since the equivalence ratio is a function of the mass flow rates, then the uncertainty in the equivalence ratio can be defined as the partial derivative of the equivalence ratio as a function of flow rates. The relative error of the equivalence ratio is given by the sum of the relative error of the individual flow rates.

$$\frac{\Delta\phi}{\phi} = \sum \frac{\Delta m_i}{m_i} \quad (3.1)$$

Similarly, the uncertainty in the gas velocity measurement is the summation of the uncertainties of the gas temperature, pressure, area and mass flow rate.

$$\frac{\Delta U}{U} = \frac{\Delta T}{T} + \frac{\Delta P}{P} + \frac{\Delta A}{A} + \sum \frac{\Delta m_i}{m_i} \quad (3.2)$$

The uncertainties of measuring mass flow rate, temperature, pressure, current and voltage have been determined by the MFC, thermocouple, pressure gauge, current probe and voltage probe manufacturer data sheets, respectively. Table 3.3 summarizes the range of operation and the accuracy of each device.

Table 3.3: Range of operation and the accuracy of the measuring devices.

Instrument	Range	Accuracy
MFC (Air)	0-18 L/min	$\pm 0.5\%$ Rd plus $\pm 0.1\%$ FS
MFC (CH <sub>4</sub> )	0-0.9 L/min	$\pm 0.5\%$ Rd plus $\pm 0.1\%$ FS
Pressure gauge	0-3 bar (abs)	$\pm 0.2\%$
Thermocouple	- 270 to 1260 °C	$\pm 0.75\%$
Voltage probe	0 - 18 kV	$\pm 3\%$ FS
Current probe	400 A	$\pm 1\%$ RS

### 3.7 Summary

In this chapter, two experimental facilities were presented. The first facility is to study the main characteristics of the plasma discharge in the DBD microplasma reactor. The second is used to study the effect of plasma discharge on combustion characteristics. The setups are designed to give an optical access to the plasma discharge and the flame at different operating pressures. Then, we presented the main components to generate the plasma discharge and to measure its electrical characteristics. The optical emission spectroscopy setup has also been discussed. The results obtained from these setups will be discussed in chapter 4, 5 and 6.





## Plasma discharge characteristics

---

In this chapter, the plasma discharge characteristics in the DBD microplasma reactor have been studied. In the following sections, we will discuss the main electric and thermal characteristics of the plasma discharge. In addition, an empirical correlation from the literature has been used to determine the reduced electric field strength at various operating pressures using the intensity ratio of vibronic emission bands of molecular nitrogen. The effects of the gas flow rate, mixture equivalence ratio, and the reactor temperature on the discharge characteristics are also investigated.

---

### 4.1 Introduction

Dielectric-barrier discharges (DBDs) are characterized by the presence of at least one insulating layer in contact with the discharge between two electrodes connected to an AC/pulse power supply. The dielectric layers covering the electrodes act as current limiters and prevent the transition to an arc discharge. The main advantage of this type of electrical discharges is that non-equilibrium and non-thermal plasma conditions can be established at atmospheric pressure.

In this chapter, we present an overview of the non-thermal plasma characteristics with a particular focus on the nanosecond discharge in/above the DBD microplasma channels over a wide range of operating conditions. In section 4.2, we describe the electric characteristics of the nanosecond pulses by measuring the pulse current and voltage together with a method used for synchronization. Then, we evaluate the energy deposited in the plasma discharge at different operating pressures. In section 4.3, the discharge structure inside the micro-channels is demonstrated using natural luminosity images as well as short exposure ICCD images.

In section 4.4, the analysis of the plasma discharge products in air using optical emission spectroscopy is presented. In section 4.5, we used the relative intensity of nitrogen bands to determine the rotational and vibrational temperatures of the discharge at different operating pressures. In section 4.6, the effective reduced electric field strength  $(E/N)_{\text{eff}}$  has been obtained from the intensity ratio of  $\text{N}_2^+(B-X)$  (0-0) band at 391.4 nm and  $\text{N}_2(C-B)$  (2-5) band at 394.3 nm.

In section 4.7, we investigate the effect of the gas flow rate on the discharge intensity. Finally, the influence of the methane-air equivalence ratio as well as the reactor temperature on the discharge breakdown characteristics have been studied experimentally and numerically, in section 4.9.

## 4.2 Electric characteristics

First investigations on the ns-DBD by Roupasov et al. (2009) and Correale et al. (2011) showed that the fast pressure gradient following the energy deposition is considered to be the main contributor for the flow actuation mechanism. In recent work, Correale et al. (2014), evidence was given of the existence of a strong thermal effect due to nanosecond plasma actuation using Schlieren imaging. The nanosecond pulse results in a temperature rising time in the order of microseconds, while gas expansion is in the order of milliseconds. This difference in the time scales generates a strong pressure rise inside the discharge volume, resulting in a weak compression wave. Therefore, it was concluded that the flow actuation mechanism is highly influenced by the electric pulse characteristics.

Beside that, calculating the energy deposited in the plasma discharge is crucial for plasma-assisted combustion research. To calculate the consumed energy, it is important to measure the discharge current and the voltage across the electrodes accurately. Many challenges are associated with measuring the voltage and current signals of the nanosecond high-voltage pulses, which may lead to inaccurate measurements. Some of these challenges are;

1. The nanosecond pulses, generically, have a high bandwidth and a short rise-time, which requires special probes with higher bandwidths than the measured signals.
2. The harmonics emitted by the strong electromagnetic field of the pulses have a wide range of frequencies. These harmonics interfere with the measured signals.
3. Jitter and voltage-current phase-shift are hard to avoid.

In our studies, the voltage and current are measured by a North Star high-voltage probe model PVM-4 and a Bergoz current transformer model CT-F0.5, respectively. A comparison between the probe characteristics and the signals to

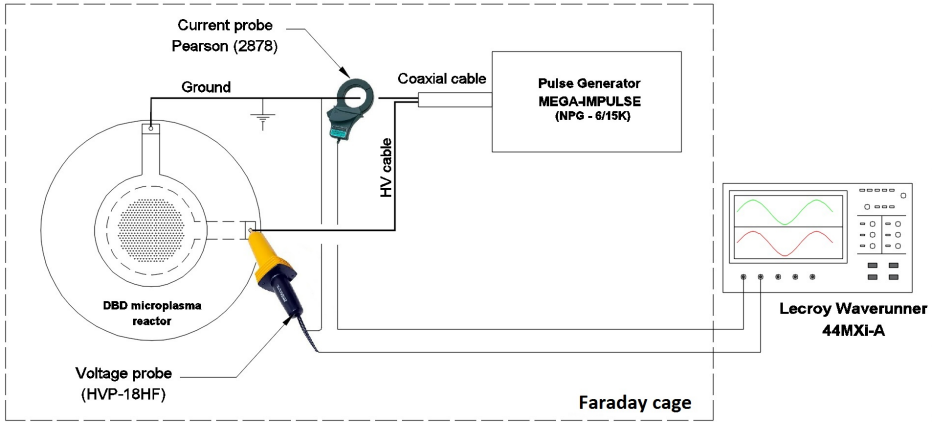


Figure 4.1: Schematic of the electrical measurement setup.

be monitored is presented in table 4.1. As shown, both voltage and current signals fall in the operational range of the probes. The signals are monitored by a Lecroy waverunner 44MXi-A oscilloscope with an analog bandwidth of 400 MHz and a maximum sampling rate of 5 GS/s. Fig. 4.1 shows a schematic of the electrical measurement setup. This setup is used to measure the actual applied voltage and the current flowing through the electrodes. To reduce the uncertainty resulting from the high-voltage harmonics, a Faraday cage has been used. All the sources of the harmonics, e.g. pulse generator, the reactor, high-voltage cable and the probes have been located inside the cage. The oscilloscope is located outside the cage to get a signal free from harmonics.

Table 4.1: Summary of PVM-4 voltage probe and Bergoz CT-F0.5 current probe characteristics and the pulse signal to be measured.

	Voltage		Current	
	Signal	Probe	Signal	Probe
Peak value	4-7 kV	60 kV	80 A	400 A
Rise time	10 ns	2 ns	4.4 ns	1.75 ns
Bandwidth	35 MHz	175 MHz	80 MHz	200 MHz
Sensitivity	-	1V/1kV	-	0.5 V/A
Accuracy	-	$\pm 2\%$	-	$\pm 0.5\%$

### 4.2.1 Electrical breakdown in micro-channels

The electrical breakdown for a gas is controlled by different parameters such as pressure, temperature, gas composition and geometry, as discussed earlier in section 2.1. Together with these parameters, the generator should also be able to provide a sufficiently high current that is required to breakdown the gas in the entire network of micro-channels. Figure 4.2 shows two conditions for the reactor in air at atmospheric pressure; (left) the current is sufficient to breakdown the gas in all the network channels and, (right) the current is capable only to partially breakdown the gas in some of the channels. It is worth mentioning that only the full-breakdown mode is considered in all the experiments in this thesis.

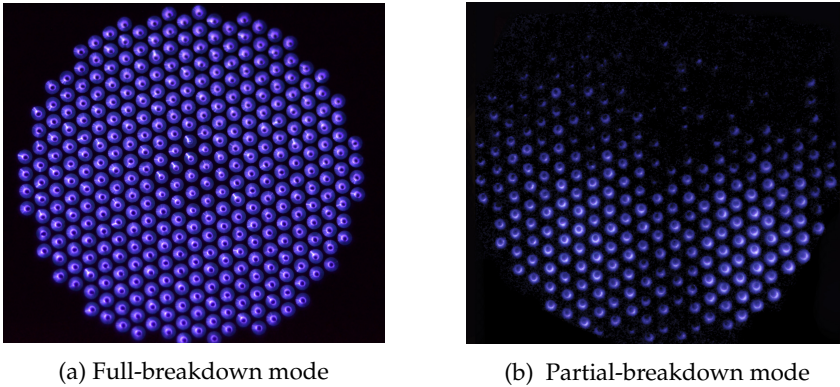


Figure 4.2: Natural emission of DBD microplasma reactor in (a) full-breakdown mode, and (b) partial-breakdown mode. Both are in stagnant air at atmospheric pressure.

### 4.2.2 Synchronization

The pulse energy has been calculated by multiplying the voltage and current waveforms. Both are recorded simultaneously for the same pulse but they are not automatically synchronized. The time-delay between the two signals could arise from the inherent time-response of the probes themselves or due to different cable lengths for the measuring probes. This delay introduces a significant error in the pulse energy calculation. Therefore, signals should be corrected for this delay before the energy calculation.

The synchronization was done by a method similar to the one performed by Xu (2013) with some modifications. The main principle of this method is the matching between the measured current ( $I_{meas}$ ) and the purely capacitive current ( $I_{cap}$ )

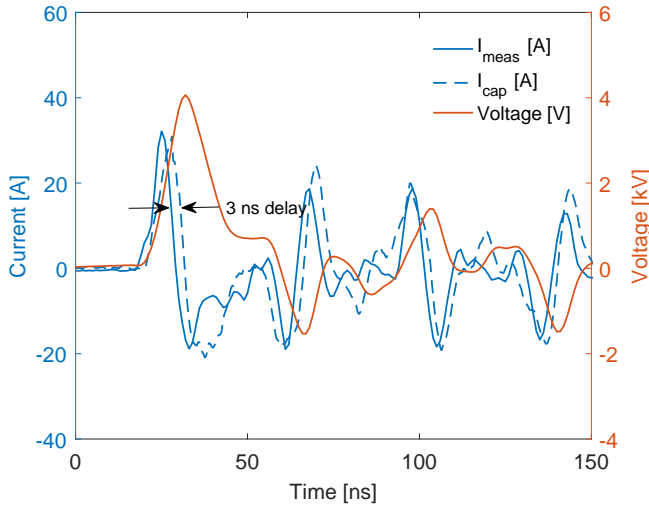


Figure 4.3: Voltage-current synchronization curve. The voltage and current waveforms have been measured in single layer operation of a DBD microplasma reactor covered by silicon layer. The signals have been averaged over 100 pulses. The capacitive current  $I_{cap}$  is calculated by Equation 4.1.

generated by the same device. In Xu (2013), they generated the purely capacitive current by reducing the voltage below the breakdown voltage. However, in our case, the minimum voltage produced by the NPG-6/15K pulse generator is 4 kV, which is capable to generate a plasma discharge in some channels. So, we had to increase the permittivity of the medium between the electrodes without changing the electrode configurations (distance between electrodes) to prevent the plasma current from forming in any of the channels. To achieve that, a layer of silicon, with a relative permittivity of 11.6, has been added to fill all the channels and to cover both surfaces in order to increase the permittivity between the electrodes. In this case, the measured current is purely capacitive, which follows the following relation;

$$I_{cap} = C \frac{dV}{dt} \quad (4.1)$$

Figure 4.3 shows the measured current ( $I_{meas}$ ), measured voltage (V) and the corresponding calculated capacitive current ( $I_{cap}$ ) by Equation 4.1 at 100 Hz. The signals have been averaged over 100 pulses. A 3 ns time-delay was observed at the half-height of the rising edge. This time-delay has been taken into account in all measurements done in this thesis.

### 4.2.3 Voltage and current measurements

Figure 4.4a shows the current  $I$  and voltage  $V$  waveforms, after synchronization, of a single pulse for single-layer operation in stagnant air at atmospheric pressure (solid lines) and at 50 mbar (dashed lines). The signals have not been averaged to avoid the jitter error. The voltage signal shows a positive polarity incident pulse with a 5 kV peak followed by a negative polarity reflected pulse with a 1.75 kV peak. The rise-time of the incident pulse is about 10 ns. The current signal shows the same behaviour, with a positive peak of 75 A, corresponding to 205 mA per channel followed by a negative peak of 58 A. The full-width at half-maximum (FWHM) duration of the current signal is 7 ns and it has a rise-time of 4.4 ns.

### 4.2.4 Pulse energy calculation

The instantaneous pulse power  $P_{pulse}$  (blue lines in Fig. 4.4b) has been obtained by multiplying the measured voltage  $V$  with the current  $I$  (after adjusting the time delay). The power has been integrated over the pulse duration to get the total energy  $E_{pulse}$  deposited in the plasma discharge:

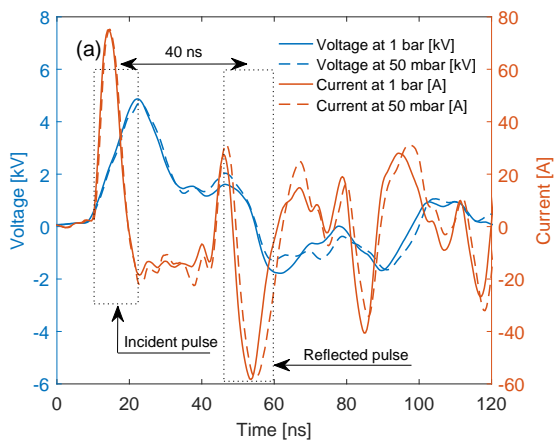
$$P(t) = I(t) \cdot V(t) \quad (4.2)$$

$$E_{pulse} = \int_{t_1}^{t_2} P(t) dt. \quad (4.3)$$

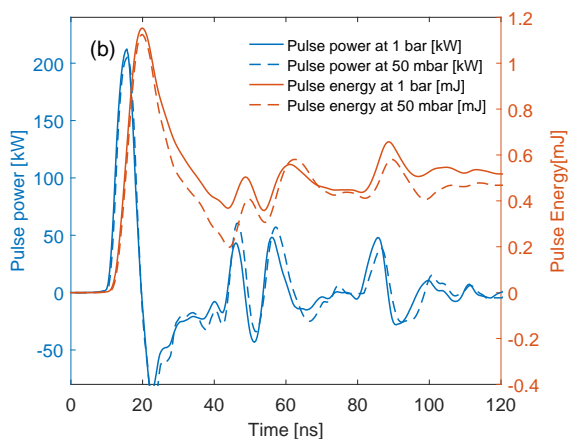
As shown in Fig. 4.4b (red lines), the total energy per pulse is about 0.53 mJ/pulse at atmospheric pressure and 0.47 mJ/pulse at 50 mbar. These values correspond to pulse energies of 1.46  $\mu$ J and 1.3  $\mu$ J per channel, respectively. The incident pulse is followed by a reflected pulse after about 40 ns, followed by some ripples. This behaviour has been validated by time-resolved measurement of the discharge emission, reported in section 4.5.2 below.

## 4.3 Optical investigation on DBD microplasma reactor

Figure 4.5 shows the structure of the plasma discharge inside and outside of the DBD microplasma holes at different operating pressures. The figure shows natural luminosity images of the plasma reactor, looking directly into the channel from above (see Fig. 3.1). The pink glow is due to the plasma in the channels, the bluish glow around it is due to the plasma on the dielectric (note that the holes in the electrodes have twice the diameter of the channels). Figure 4.6 shows short exposure ICCD images of single pulses in one channel under similar conditions.



(a) Voltage (blue lines) and current (red lines) waveforms.



(b) Power (blue lines) and energy (red lines) waveforms.

Figure 4.4: (a) Temporal development of the applied voltage (blue lines) and resulting current (red lines) at the plasma reactor. (b) Calculated instantaneous power (blue lines) and pulse energy (red lines). All are for stagnant air at atmospheric pressure (solid lines) and 50 mbar (dashed lines).

At atmospheric pressure, Fig. 4.5a, the discharge is concentrated as an annulus on the inner wall of the channel and no discharge is visible in the center of the holes. This is related to the short mean free path of the electrons due to the inelastic collisions with the neutral atoms, which narrows the discharge region. Outside the holes, a micro-filamentary discharge from the hole to the cathode ring can be



observed (the white reddish lines traversing the bluish regime). The single-pulse ICCD image in Fig. 4.6a shows a similar behaviour.

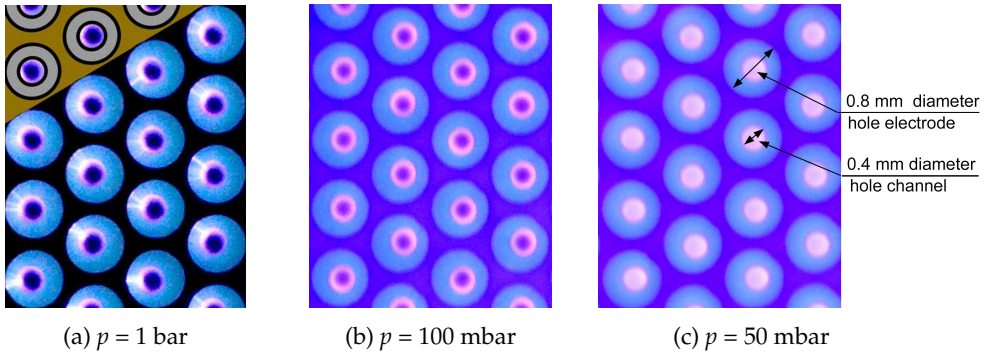


Figure 4.5: Natural luminosity images of plasma discharge in DBD microplasma reactor in stagnant air at voltage = 5 kV and pulse repetition frequency = 2 kHz at three different pressures. Exposure time = 50 ms. A detail of the schematic drawing from Fig. 2.3 has been overlaid on (a) to give a sense of scale.

At a pressure of 100 mbar, Fig. 4.5b, the mean free path of the electrons increases, resulting in a wider and more uniform annular ring inside the holes. Also, note the absence of micro-filamentary discharges, also in the short exposure image (Fig. 4.6b). Meanwhile, the glow discharge extends beyond the confinement of the holes, giving rise to the faint pink glow over the whole field of view. By decreasing the pressure further to 50 mbar, Figs. 4.5c and 4.6c, the plasma discharge is characterized by a high current and it uniformly fills the whole channel.

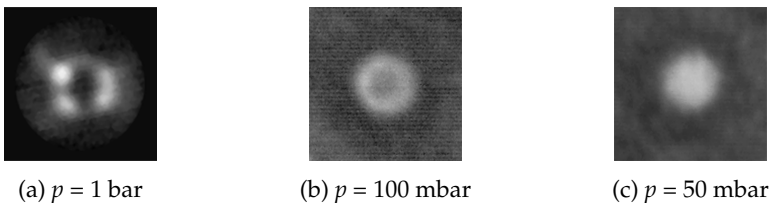


Figure 4.6: ICCD images of a plasma discharge in a single channel during one pulse with an exposure time of 200 ns in stagnant air at voltage = 5 kV at three different pressures.

## 4.4 Plasma emission

Emission spectra intensities in DBD microplasma reactor have been recorded under two different operating pressures in stagnant air: atmospheric pressure and 50 mbar, to study the effect of the operating pressure on the discharge emission structure. The emissions are recorded using the 300 grooves/mm grating, covering a spectral range from 300 nm to 500 nm. The signals are integrated over 100 ns after the onset of the pulse.

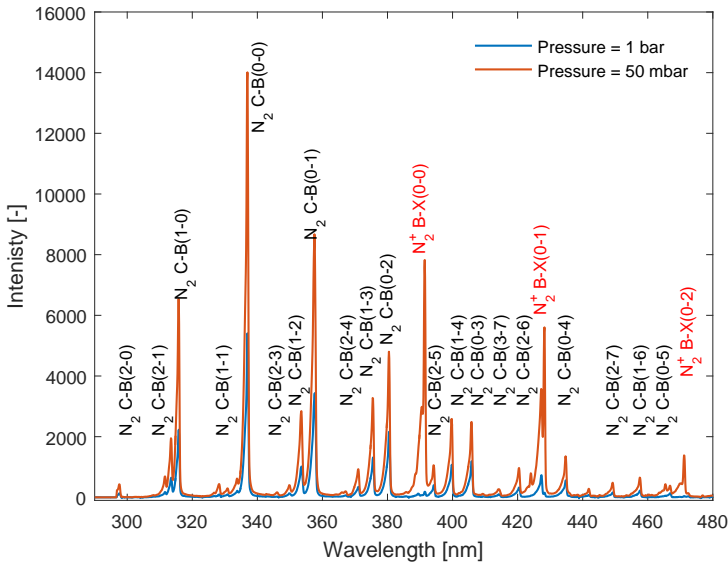


Figure 4.7: Spectral intensities for air in DBD microplasma discharge at atmospheric pressure (blue line) and  $P = 50$  mbar (red line) at voltage of 5 kV. The spectra are recorded using 300 grooves/mm grating covering 300 nm to 500 nm. The signals are integrated over 100 ns after the onset of the pulse.

As shown in Fig. 4.7 the air plasma produces a large amount of excited species of N<sub>2</sub>, including but not limited to bands of the N<sub>2</sub> second positive system N<sub>2</sub> (C-B) and also bands of the first negative system for the nitrogen ion N<sub>2</sub><sup>+</sup> (B-X). It is clear from the figure that the emission at a pressure of 50 mbar is much higher (about three times) than the intensity at atmospheric pressure. Not only the magnitude, but we can also notice a large amount of nitrogen ions N<sub>2</sub><sup>+</sup> (B-X) at low pressure, which is barely visible at atmospheric pressure. This is an indication of the high electron density and energy at low pressure compared to high pressure. This can be explained by increasing the mean free path when reducing the pressure. This increases the number of ionization processes significantly at low pressure, as mentioned in section 4.3.

## 4.5 Discharge temperature

Gas temperature is a very important parameter in plasma science for two reasons. Firstly, the gas temperature has a direct effect on reactive species generation, (Sismanoglu et al. 2010). Secondly, there are many applications that need control of thermal behaviour, like wound treatment, chemical decomposition, combustion, etc. Nanosecond plasma discharges typically are of non-equilibrium nature resulting in different kinetic energy distributions for the different species (i.e. electrons, ions, neutrals). Apart from that, the different degrees of freedom (electronic, translation, vibration and rotation) are also not necessarily in equilibrium, (Bruggeman et al. 2014; Roupassov et al. 2009). In the following sections we will focus on the rotational and vibrational temperature measurement of the plasma discharge in the DBD microplasma reactor, as well as the average gas temperature.

### 4.5.1 Rotational temperature

The rotational temperature of the plasma discharge in stagnant air has been obtained by fitting the experimentally observed spectra of the (0 – 2) band structure of the second positive system (SPS) of  $N_2$  ( $C^3\Pi_u \rightarrow B^3\Sigma_g$ ) with the SPECAIR simulation tool Laux et al. (2006) convoluted with the measured instrumental slit function. The spectra are integrated over 20 ns following the start of the voltage pulse, using a spectrograph slit width of 2  $\mu\text{m}$ . The signal has been accumulated over 300,000 pulses to increase the signal-to-noise ratio. The signal was collected from an area covering four complete holes at the center of the reactor disc. The measurements are carried out for a pulse repetition frequency of 3 kHz using the grating of 3600 grooves/mm.

As shown in Fig. 4.8, when comparing the rotational line structure with a simulated Boltzmann rotational distribution, a good fit was obtained at both atmospheric pressure and reduced pressure. This implies that the rotational distribution has been thermalized (via heavy species collisions or electron collisions) in a short time (few nanoseconds). The rotational distribution of the excited states can be considered representative of the ground state rotational temperature, which is usually close to the gas temperature Fridman (2008).

The rotational temperatures obtained from the SPECAIR fitting procedure were  $550 \text{ K} \pm 30 \text{ K}$  and  $470 \text{ K} \pm 30 \text{ K}$  for pressures of  $p = 1 \text{ bar}$  and  $p = 50 \text{ mbar}$ , respectively. This indicates that the rotational temperature reduces with the reduction in the operating pressure, which agrees with the reduction in the consumed power as indicated in Fig. 4.4b. A related point to consider is that the measured rotational temperature is only applied during the pulse. After the pulse, the temperature relaxes over time until subsequent pulse comes.

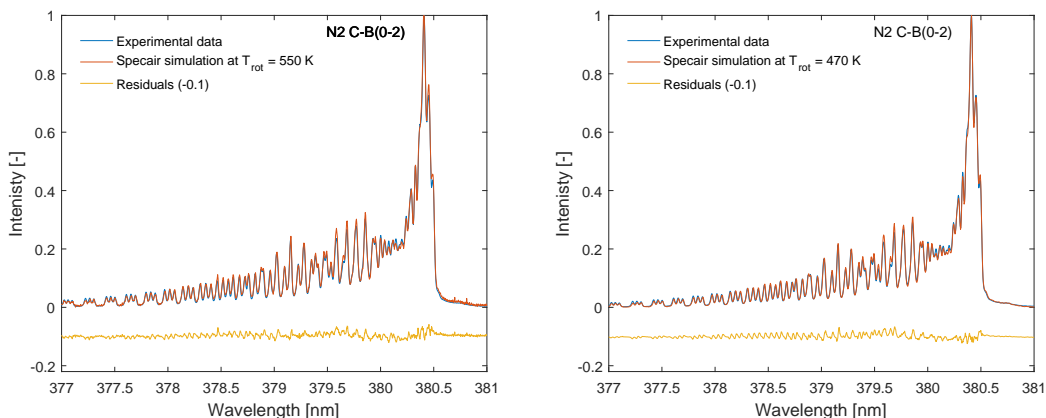


Figure 4.8: Experimental (blue line) and simulated (red line) normalized spectrum of stagnant air at (left)  $p = 1$  bar, and (right)  $p = 50$  mbar. The simulated spectra are from SPECAIR using  $T_{rot} = 550$  K and  $T_{rot} = 470$  K, respectively.

### 4.5.2 Vibrational temperature

The vibrational temperature describes the population of the vibrational states of molecular species, if this follows a Boltzmann distribution. In this study, the vibrational temperature has been obtained by fitting the observed structure of the (0-2), (1-3) and (2-4) spectral bands of the SPS of  $N_2$  to SPECAIR simulations. By using a grating of 1800 grooves/mm and integrating the signal over 100,000 pulses.

Here, the fit is not as good as for the rotational temperature, leaving a higher uncertainty in the vibrational temperature calculations. This fitting error may be caused by errors in the intensity calibration of the spectrometer or by the non-Boltzmann nature of the discharge. Therefore, the estimated vibrational temperature here is the temperature corresponding to the minimum residual error for these three bands considered. As shown in Fig. 4.9, estimated vibrational temperatures of  $3460 \pm 100$  K at atmospheric pressure and  $3980 \pm 100$  K at  $p = 50$  mbar can be extracted. Obviously, the vibrational temperature is considerably higher than the rotational and, presumably, the translational temperatures. The reduction of the vibrational temperature with increasing operating pressure can be attributed to two factors. On the one hand, there is enhanced collisional relaxation of the vibrationally excited levels as the collisional frequency increases. On the other hand, less energy may be put into vibration due to the reduction in the electron energy with pressure. This finding will be discussed in more detail later, in the context of estimating the reduced electric field strength at different operating pressures in section 4.6.

In order to illustrate the discharge behaviour during the pulse duration, the

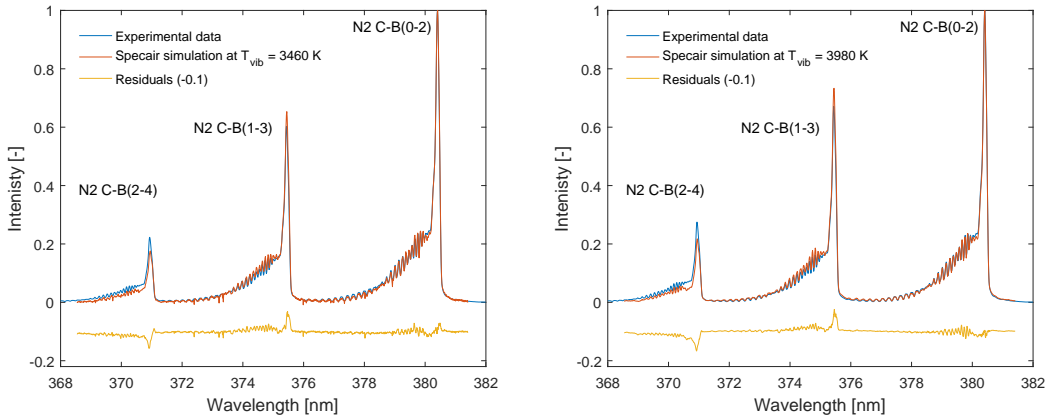


Figure 4.9: Experimental (blue line) and simulated (red line) normalized spectra of stagnant air at (left)  $p = 1$  bar, and (right)  $p = 50$  mbar. The simulated spectra are from SPECIAIR with  $T_{vib} = 3460$  K and  $T_{vib} = 3980$  K respectively.

time evolution of spectral intensity between 330 nm and 420 nm over a time span of 80 ns is shown in Fig. 4.10. Each spectrum in this figure is integrated over a temporal window of 3 ns, using a 300 grooves/mm grating. As shown, there are two main peaks in the spectra, separated by 40 ns. This behaviour agrees very well with the power measurements from Fig. 4.4b, as it also shows two principle power peaks with roughly the same time separation.

It is worth to mention that no vibrational or rotational temperature differences were observed between the first peak at  $t = 25$  ns and the second peak at 65 ns, as can be driven from Fig. 4.11. These spectra have been recorded in stagnant air at atmospheric pressure using the 1800 grooves/mm grating centered at 355 nm to cover the (0-1) and (1-2) bands of the SPS of  $N_2$ . About 30 percent reduction in emission intensity has been observed between the first and the second peak.

### 4.5.3 Average gas temperature

To measure the average gas temperature downstream of the reactor, we have used a thermocouple type K (model Testo 0613-1912) with a 5 mm probe diameter and a reaction time of 35 seconds to damp noise. The probe junction is located 5 mm downstream from the central hole of the reactor. Fig. 4.12 shows the air temperature as a function of pulse repetition frequency for an air flow rate of 3.4 l/min at atmospheric pressure.

As shown in the figure, there is a linear relationship between pulse repetition frequency and average gas temperature, with a slope of 6.5 K/kHz. From this

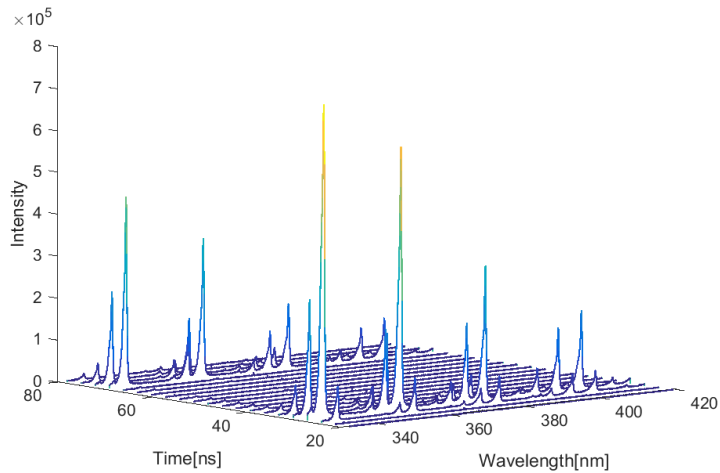


Figure 4.10: Temporal development of emission spectra of the plasma discharge at atmospheric pressure in air, with an integration window of 3 ns using a 300 grooves/mm grating.

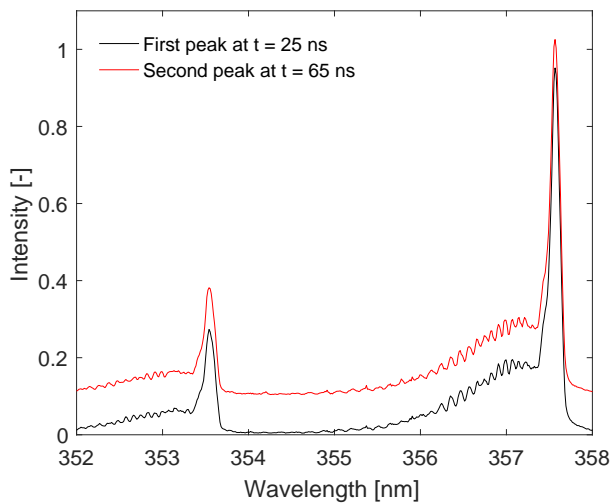


Figure 4.11: A comparison of the normalized spectra for the first peak (black line) and the second peak (red line) during one pulse. The signals are integrated over 100,000 pulses for stagnant air at atmospheric pressure. The second peak line has been shifted upward by 0.1 for better visualization.

relationship, we can extract an average value of the thermal power generated by the plasma discharge,  $Q_{plasma} = \dot{m} \cdot c_p \cdot \Delta T$ , where  $\dot{m}$  is the mass flow rate,  $c_p$  is the specific heat of air at constant pressure and  $\Delta T$  is the difference between inflow and outflow temperatures. This gives an average value of 0.45 W for 5 kV pulses at a repetition frequency of 1 kHz, or in other words, the energy spent to gas heating is 0.45 mJ/pulse for all channels combined.

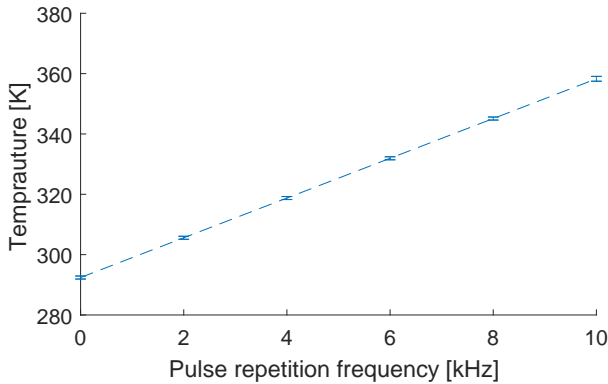


Figure 4.12: Measured gas temperature as function of pulse repetition frequency for air with flow rate of 3.4 l/min at atmospheric pressure and  $V = 5$  kV. The dashed line indicates a linear fit and the error bars represent the standard deviation in the measurements.

This value is 85 % of the pulse energy calculated from the voltage and current measurements at atmospheric pressure in section 4.2. The rest of the consumed power is spent on other degrees of freedom such as dissociation of the molecular gas components (like the dissociation of the molecular oxygen in the quenching reaction of  $N_2(B)$  (Rusterholtz et al. 2013)), heating of the dielectric material and conduction to the metal body. In case of reduced pressure, it is expected that the fraction of the power which is dissipated into gas heating will be lower, and more power will go to the chemical processes due to the higher electron energy and hence ionization efficiency.

## 4.6 Effective reduced electric field strength $(E/N)_{\text{eff}}$

The reduced electric field  $E/N$  is defined as the electric field  $E$  normalized to the natural number density  $N$ . The determination of the electric field is important as it is considered the main driving force for the plasma discharge. On the other hand, electric fields affect the flame stability, emissions and soot formation (Belhi et al. 2010; Lee et al. 2005; Saito et al. 1999).

Determination of the actual reduced electric field  $(E/N)$  by direct methods is relatively complicated for pulsed microdischarges because both the electric field

( $E$ ) and the concentration of neutral particles ( $N$ ) vary strongly in time and space. However, Paris et al. (2005) introduced an indirect method by using the intensity ratio of nitrogen spectral bands. The obtained intensity ratio can be used for electric field strength estimation if the nitrogen molecules are excited dominantly from the ground state directly by the electron impact.

For this the (0-0) transition band of the first negative system of  $N_2^+$  (FNS;  $B^2\Sigma_u^+ \rightarrow X^2\Sigma_g^+$ ) at 391.4 nm and the SPS (2-5) band at 394.3 nm are used. The following relation between the intensity ratio  $R_{391/394}$  and the reduced electric field has been proposed for low-temperature plasmas in air in a pressure range of 0.3 – 100 kPa with a maximum deviation of 12%:

$$R_{391/394} = 46 \exp \left[ -89 \left( \frac{E}{N} \right)^{-0.5} \right]. \quad (4.4)$$

Figure 4.13 shows the integration window used in the reduced electric field calculations. The integration window covers four channels in the center of the reactor, with a width of 50  $\mu\text{m}$  and a height of 4 mm. Fig. 4.14 presents images of the emission spectra between 388 nm and 395 nm at different operating pressures. The images show the  $N_2^+$  (B-X) (0-0) line at 391.4 nm and the  $N_2$  (C-B) (2-5) line at 394.3 nm for the incident pulse (left) and the reflected pulse (right).

The distribution of the  $N_2^+$  (B – X) (0-0) and  $N_2$  (C – B) (2-5) intensities over the channel width are presented in Fig. 4.15, at 300 and 50 mbar, for both the incident and reflected pulses at 5 kV and 3 kHz pulse repetition rate. The spectra of the  $N_2^+$  (B – X) (0-0) and  $N_2$  (C – B) (2-5) bands are accumulated for 10 ns after the onset of each pulse and integrated over 300,000 pulses using a 1800 grooves/mm grating.

Three distinct regimes can be recognized from these figures when going from the center of a channel outwards: (1) inside the channel (A-B), (2) between the channel and the grounded electrode edge (B-C), and (3) the grounded electrode (C-D). At 300 mbar, and during the incident pulse, the minimum intensity of the nitrogen FNS is located at the center of the channel (point A). Going outwards, two peaks can be distinguished. The first peak is located inside the channel close to the wall (point B). This is caused by the integration over the line of sight of the ionization wave which is travelling from the high-voltage electrode towards the channel exit. This peak is expanding by reducing the pressure until it reaches the center at 50 mbar when the central minimum disappears.

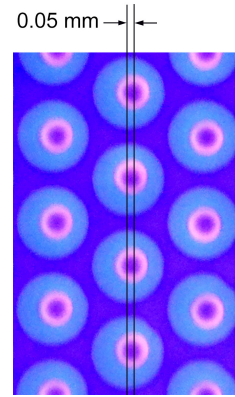


Figure 4.13: The integration window used for the reduced electric field calculations.



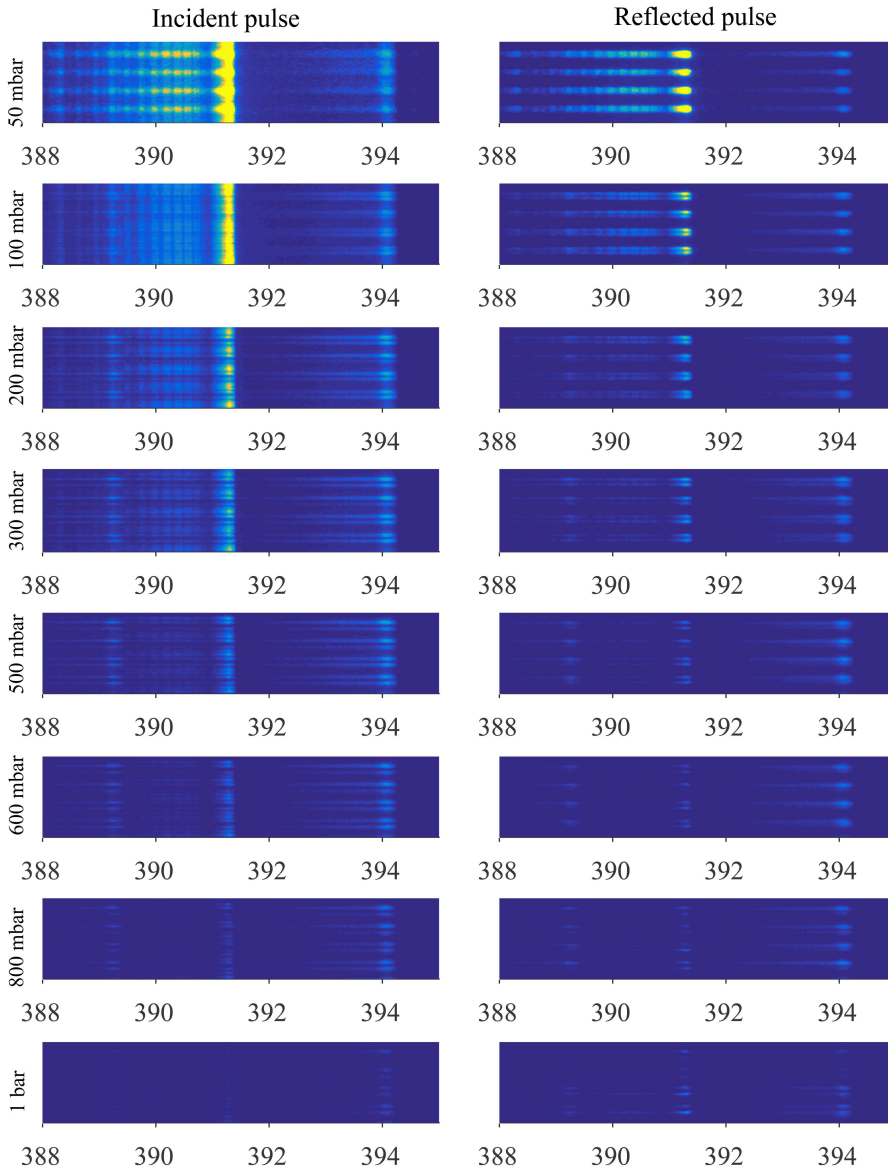


Figure 4.14: Emission spectra of plasma discharge in DBD microplasma reactor at different operating pressures. The images cover the spectra from 388 nm to 395 nm showing the  $N_2^+$  (B-X) (0-0) at 391.4 nm and the  $N_2$  (C-B) (2-5) at 394.3 nm for four channels in row at the center of the reactor. The emissions are integrated over 10 ns after the onset of (left) the incident pulse and (right) the reflected pulse. All are for 5 kV and 3 kHz pulse repetition rate at different operating pressures in stagnant air. The signals are integrated for 300,000 pulses.

The second peak is located at the grounded electrode edge (point C), which is most likely produced by a discharge which is formed due to the field enhancement at the grounded electrode edge. The intensities of the two peaks have almost the same strength, even at different operating pressures. In contrast, during the reflected pulse, only one peak of  $N_2^+(B-X)$  (0-0) is formed, the one at the channel walls while the one at the grounded edge is absent. This could be explained by the following three effects: Firstly, the high electron density leftovers from the incident pulse around the grounded electrode covers the sharp edge, which consequently reduces the local field enhancement as well as the energy and number of produced electrons. Secondly, it could be related to the drift direction of the electrons. Thirdly, the low voltage of the reflected pulse compared to the incident pulse may prevent the  $N_2^+(B-X)$  (0-0) excitation.

The vibrationally excited nitrogen state  $N_2(C-B)$  (2-5) appears mostly near the wall of the channel during both the incident and reflected pulses, although with about half of the intensity during the reflected pulse. Furthermore, it seems like the discharge at the grounded electrode, near point (C), consumes most of the energy on the ionization and less on vibrational excitation. This can explain the reduced amount of  $N_2(C-B)$  (2-5) compared to  $N_2^+(B-X)$  (0-0) at this location.

For pressures between one atmosphere and 100 mbar, the discharges have almost identical structures and only differ in the relative intensities between the excited states. However, at 50 mbar, the structure changes dramatically, as shown in the bottom graphs in Fig. 4.15. The major difference in the structure is that there is only one peak in the center of the channel for both the SPS of  $N_2$  and FNS of  $N_2^+$ , this is due to the large main free path at 50 mbar, as discussed earlier in section ???. It is also clear that the FNS of  $N_2^+$  is about one order of magnitude higher than the SPS of  $N_2$ , which indicates a high reduced electric field strength.

Figure 4.16 shows the effective reduced electric field strength  $(E/N)_{\text{eff}}$  which is determined by the intensity ratio method, presented in Eq.4.4, for the incident and reflected pulses. A spatial averaging has been performed for the  $N_2^+(B-X)$  (0-0) and  $N_2(C-B)$  (2-5) over (A-B) and (B-D) positions for one channel. The signals are accumulated for 10 ns and integrated over the line of sight for 300,000 pulses.

The general trend, for all lines in the figure, is that the effective reduced electric field strength increases gradually with decreasing operating pressure. This trend is expected, as the neutral number density of the gas decreases with pressure while the applied voltage (and therefore path-integrated electric field) remains constant. The figure shows a value of  $550 \pm 100$  Td and  $340 \pm 50$  Td for  $(E/N)_{\text{eff}}$  for the incident pulse inside the channel (A-B) and outside the channel (B-D), respectively. By reducing the pressure down to 100 mbar,  $(E/N)_{\text{eff}}$  increases gradually to  $4600 \pm 700$  Td and  $1900 \pm 300$  Td. Also, at this pressure range,  $(E/N)_{\text{eff}}$  for the reflected pulse inside the channel is slightly higher than for the incident pulse. This can be explained by the substantial increase in  $(E/N)_{\text{eff}}$  of the incident pulse outside the channel. By reducing the pressure down to 50 mbar,  $(E/N)_{\text{eff}}$  inside the channel increases to about  $10000 \pm 1500$  Td for the incident pulse with a relatively

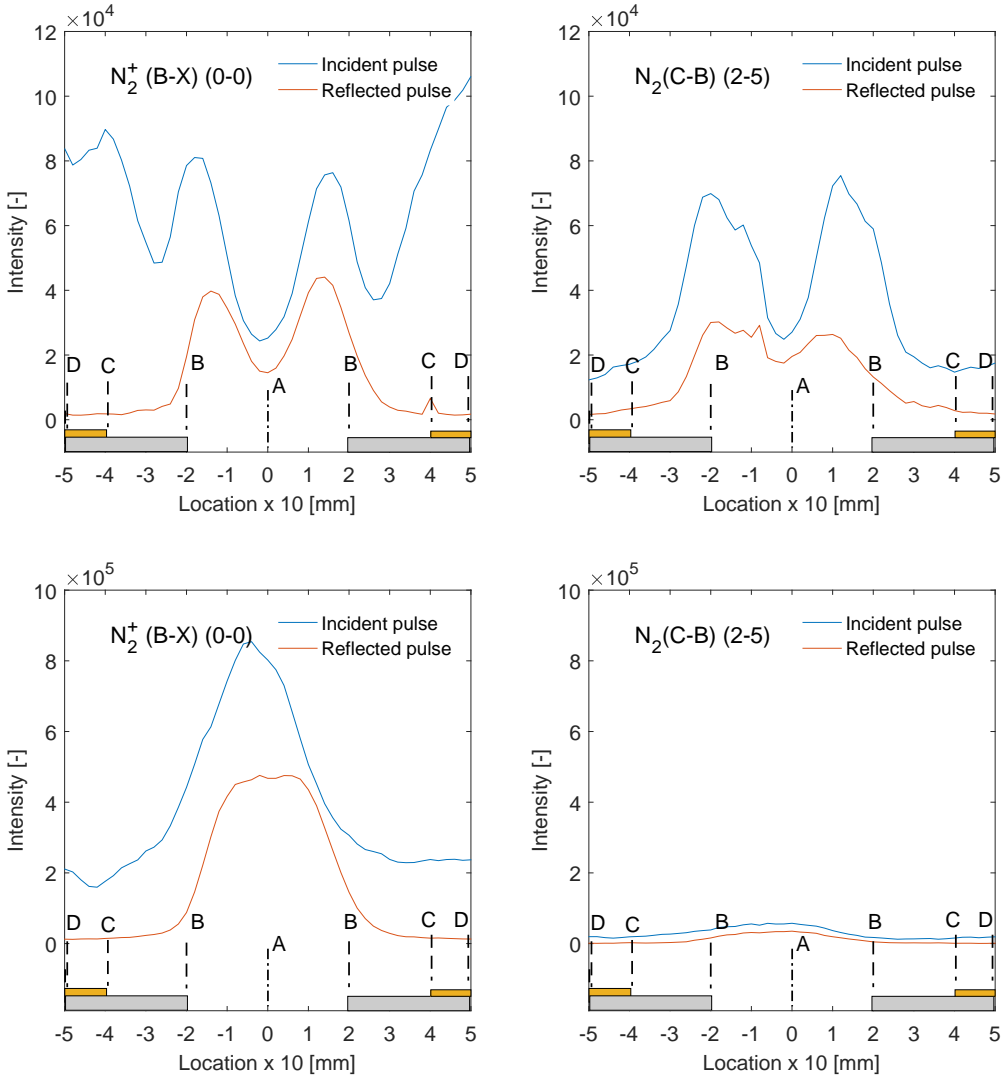


Figure 4.15: Emission intensity of (left) the  $N_2^+$  (B-X) (0-0) at 391.4 nm and (right) the  $N_2$  (C-B) (2-5) at 394.3 nm over one channel at pressure of 300 mbar (top) and 50 mbar (bottom). The signals are accumulated for 10 ns during the incident pulse (in blue) and reflected pulse (in red). All for 0.55 mJ per pulse and 3 kHz repetition rate in stagnant air and the signals are integrated for 300,000 pulses.

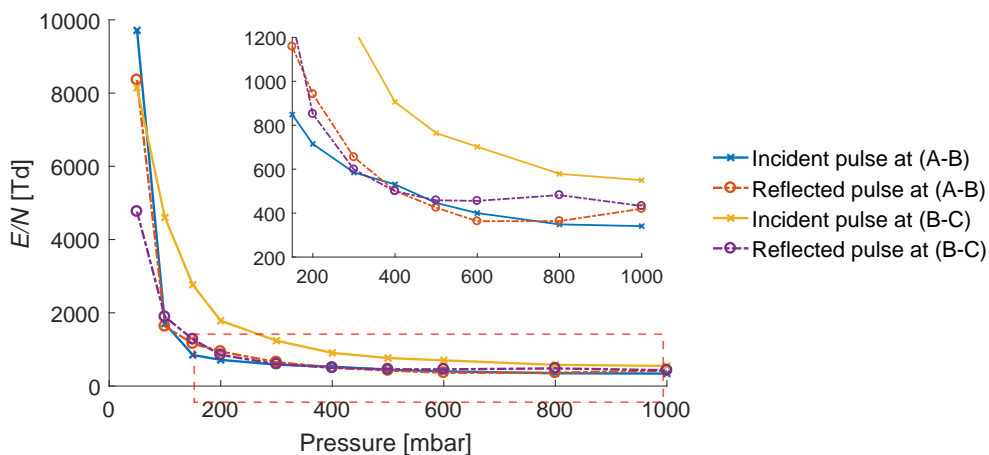


Figure 4.16: Effective reduced electric field  $(E/N)_{\text{eff}}$  as a function of the operating pressure, calculated from the intensity ratio  $R_{391/394}$  for (solid line) incident pulse, (dashed line) reflected pulse, ( $\times$ ) for B-C, and ( $\circ$ ) for A-B. The insert shows a magnification for the range of 150 mbar to 1 bar. Plasma conditions are given in Fig. 4.15.

lower value outside the channel.

## 4.7 Effect of flow rate on discharge intensity

To study the effect of the flow velocity inside the channels on the discharge intensity in the DBD microplasma reactor, a set of experiments has been done for different air flow velocities at atmospheric pressure with 5 kV pulses at 3 kHz repetition rate. This study has been carried out for mean air flow velocities ranging from 0 to 7 m/s inside the channels, corresponding to average flow velocities from 0 to 1 m/s above the reactor.

Figure 4.17 shows the residence time of a volume of gas passing through the discharge region in a channel (distance of 0.36 mm for single-layer operation) ranges from 50 to 250  $\mu\text{s}$  for air velocities between 7 and 1.4 m/s. Obviously, the minimum residence time is much longer than the characteristic time scale of the plasma discharge, which is tens of nanoseconds. However, these residence times are slightly shorter than the inter-pulse delay (333  $\mu\text{s}$ ) at a pulse repetition frequency of 3 kHz, except for stagnant air.

This explains the reduction in emission intensity at higher flow velocities, as shown in Fig. 4.18. The figure shows a roughly 25% reduction in emission intensity when increasing the flow from 0 to 1.4 m/s and a smaller, more grad-

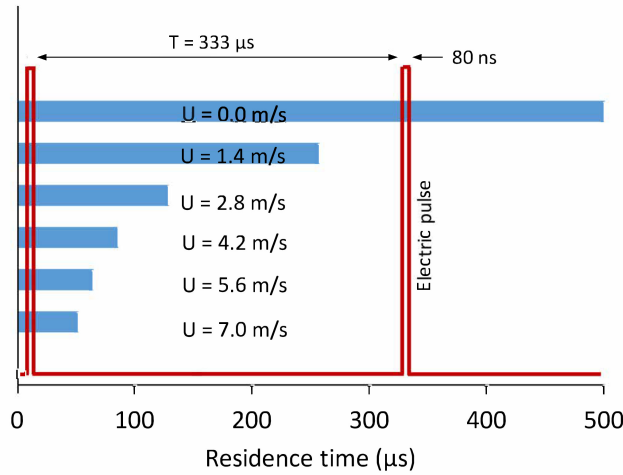


Figure 4.17: Gas residence time in the discharge region of the channels at different flow velocities and 3 kHz pulse repetition rate.

ual, reduction when increasing the flow further up to 7 m/s. In stagnant air, all high-voltage pulses ionize the same volume of gas in the discharge region. This increases the ionization level before the new breakdown occurs which leads to higher emission intensity, (Höft et al. 2016; Nijdam et al. 2010) while at higher velocities most of the gap is filled with fresh gas and less pre-ionization will exist.

## 4.8 Effect of pulse repetition frequency on discharge deposited energy

The nanosecond discharge in DBD microplasma reactor is affected by many factors. In this section, the effect of the pulse repetition frequency on the discharge energy is investigated. In this experiment, we applied a fixed voltage of 5 kV on a single-layer DBD reactor in stagnant air at atmospheric pressure. We can see from Fig. 4.19 that by increasing the pulse repetition frequency, the discharge intensity increases as more channels are ignited. The pulse energy is calculated at various pulse repetition frequencies, ranging from 0.1 kHz to 1.8 kHz.

As shown in Fig. 4.20, below 400 Hz, the reactor works in a capacitive mode only, and no plasma discharge is noticed. In this mode, all the current waves reflect back to the power supply, so that nearly no energy is deposited in the discharge. Above 400 Hz, the gas starts to breakdown in some channels, as shown in Fig. 4.19a, with a total energy of about 0.2 mJ/pulse. The discharge intensity is enhanced as the frequency increases from 400 Hz to 1.8 kHz. The total energy per

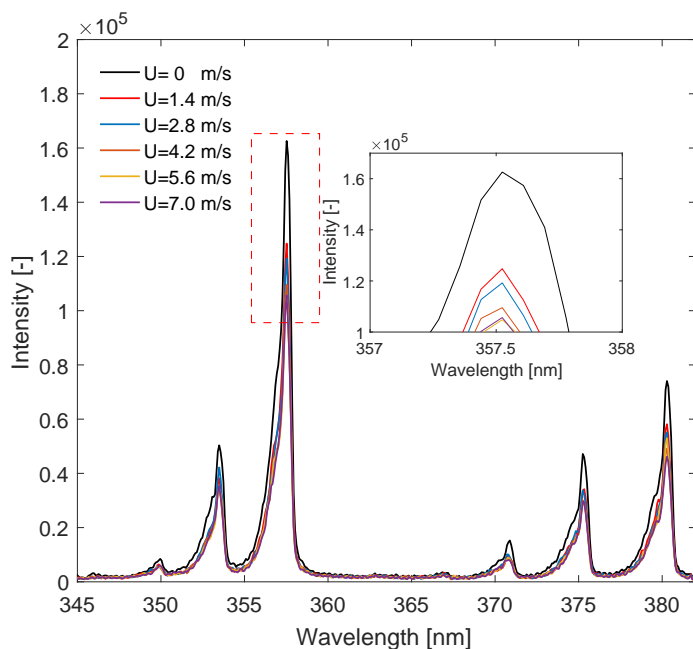


Figure 4.18: Non-normalized emission spectra in air at atmospheric pressure for different flow velocities for 5 kV pulses at 3 kHz repetition rate. The inset shows a magnification of the largest peaks (dashed).

pulse increases up to a threshold value of 0.53 mJ/pulse at a repetition rate of 1.6 kHz where all the channels are simultaneously ignited, see Fig. 4.19c.

This increase in the pulse energy can be attributed to several factors. Firstly, the increase in the pulse repetition rate increases the total plasma current due to the increase in the number of the ignited channels, as shown in Fig. 4.20. Secondly, it results in an accumulation in the residual ions and metastable species, which enhances the development of the discharge and, consequently, increases the discharge energy. Thirdly, it can be due to the heating of the dielectric material sequentially by the high-voltage pulses. This leads, on the one hand, to a reduction in the dielectric constant due to the effect of the heat on the orientational polarization, Eroglu et al. (2012). On the other hand, it heats up the gas inside the channels. Both effects give rise to the increase in the pulse energy.

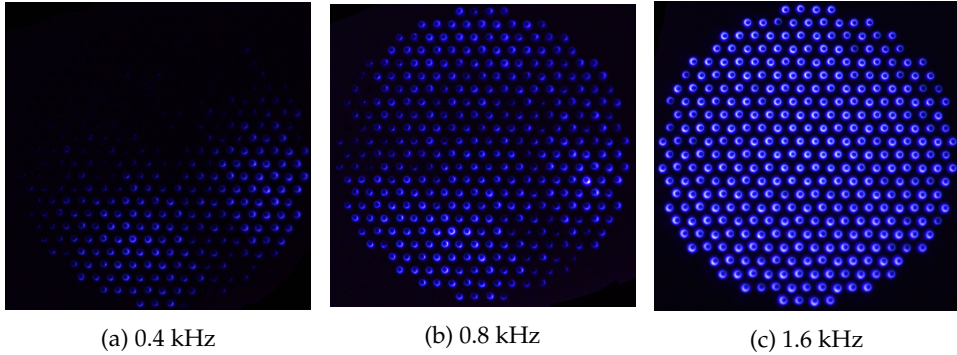


Figure 4.19: Images of plasma discharge in DBD microplasma reactor in stagnant air at voltage = 5 kV and pulse repetition frequency of (a) 0.4 kHz, (b) 0.8 kHz, and (c) 1.6 kHz. Exposure time = 200 ms.

## 4.9 Effect of equivalence ratio on the discharge characteristics

In the subsequent chapters we will study the effect of the nanosecond pulsed discharge on the combustion characteristics. However, during the experiment with methane-air gas mixture, we have noticed a change in the discharge performance by changing the gas composition from pure air to methane-air mixture. Therefore, we investigated the effect of the equivalence ratio of the methane/air mixture without burning, as well as that of the reactor temperature on the discharge characteristics. More specifically, we studied the influence of the mixture equivalence ratio on the full-breakdown frequency and the pulse energy.

### 4.9.1 Full-breakdown frequency

The full-breakdown frequency is defined as the pulse frequency at which the discharge breakdown is occurring in all the reactor channels simultaneously. To study the effect of the equivalence ratio on the full-breakdown frequency, we fixed the equivalence ratio at a certain value and increased the pulse frequency gradually till a visual breakdown in all the channels is achieved. Then, we did the same for all other equivalence ratios. The experiment is carried out at a fixed applied voltage of 5 kV at atmospheric pressure. The equivalence ratio is controlled by changing the fuel and air mass flow rate simultaneously, while keeping the total inlet volume flow rate constant at 3.4 l/s. The reactor temperature was varied between 298 K, 313 K and 328 K by changing the water jacket temperature. The reactor temperature was measured by means of a K-type thermocouple installed directly on the top surface near the central channel. The temperature was measured before turning on the plasma discharge to avoid the electromagnetic noise

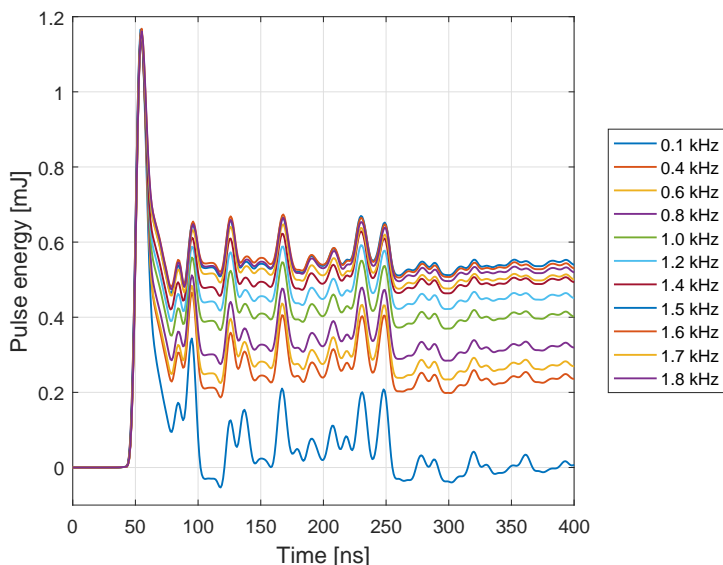


Figure 4.20: Effect of pulse repetition frequency on the discharge deposited energy. All are for stagnant air at atmospheric pressure and applied voltage of 5 kV.

resulting from the high-voltage pulses, as discussed in Section 4.2. Although the measured temperature is not exactly equal to the actual real-time reactor temperature during the pulse duration due to the pulse heating effect, it will still give a qualitative evaluation of the effect of the reactor temperature on the gas breakdown characteristics.

Figure 4.21 gives the correlation between the mixture equivalence ratio as well as the reactor temperature and the full-breakdown frequency. By increasing the equivalence ratio from zero to one, the full-breakdown frequency increases from 0.4 kHz to 5 kHz at a reactor temperature of 298 K (black line). While, at a reactor temperature of 323 K (red line), the same increase in the equivalence ratio results in an increase in the full-breakdown frequency from 0.25 kHz to 1.08 kHz only. Unlike pure air, it is important to point out that partial-breakdown (breakdown in some of the channels only) is not noticed for any equivalent ratio above zero. This means adding any amount of fuel to the air flow, and by gradual increase in the pulse frequency, the discharge goes from no-breakdown mode to full-breakdown mode directly, without passing by partial-breakdown mode.



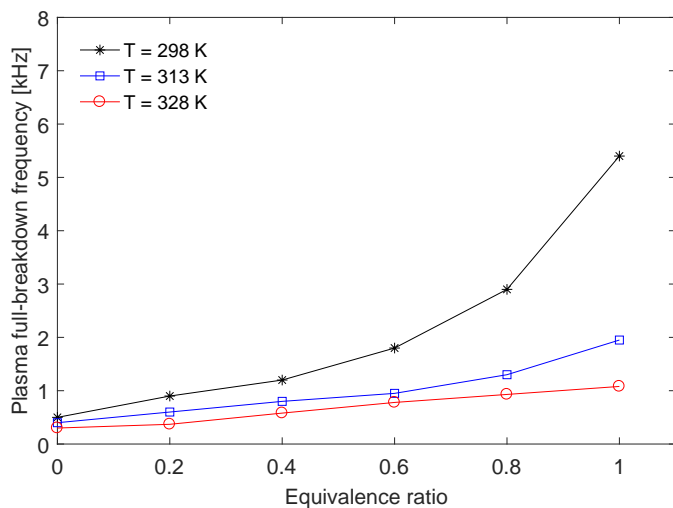


Figure 4.21: Effect of methane-air equivalence ratio ( $\phi$ ) on the full-breakdown frequency. The experiment is carried out at reactor temperatures of 298 K (in black), 313 K (in blue) and 328 K (in red). The total mass flow rate is constant at 3.4 l/s, and the voltage is 5 kV at atmospheric pressure.

### 4.9.2 Pulse energy

Studying the effect of the equivalence ratio on the plasma discharge is important to accurately determine the percentage of the flame power to the consumed power in the plasma discharge. To evaluate this, the pulse energies have been obtained for different equivalence ratios. The pulse energy was calculated by the same procedure as discussed in Sec. 4.2. Figure 4.22 shows the total pulse energy for different equivalence ratios, ranging from 0.5 to 0.75, while keeping the voltage across the electrodes at 5 kV. As shown in the figure, by increasing the equivalence ratio from 0.5 to 0.75, the total pulse energy decreases, slightly, from 0.45 to 0.42 mJ/pulse. A similar behaviour has been observed by Pilla et al. (2006), where they found that the excited species are partially consumed, quenched or produced in a smaller amount by increasing the amount of the fuel in the mixture. In the next section, we will explain this reduction of the pulse energy by studying the effect of the equivalence ratio on the kinetic and transport behavior.

### 4.9.3 Kinetic and transport coefficients of electrons in methane/air mixtures

To understand the discharge breakdown behavior in the DBD reactor for methane-air mixtures, the effect of the fuel content on the kinetic and transport coefficients

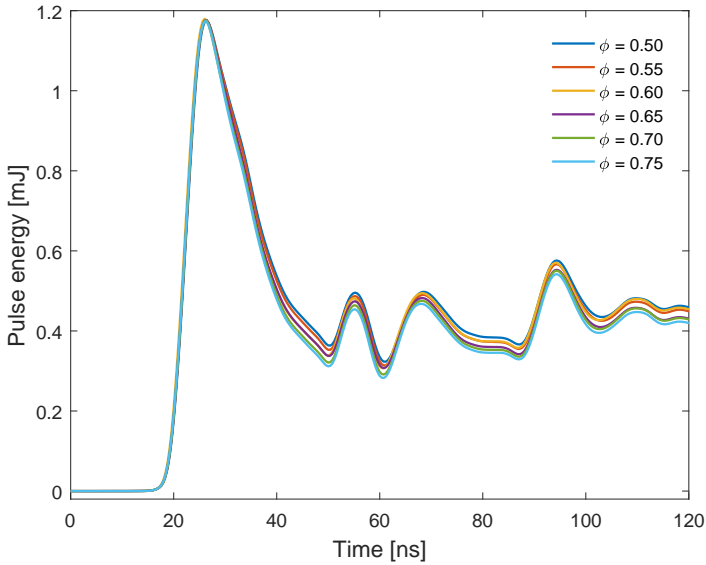


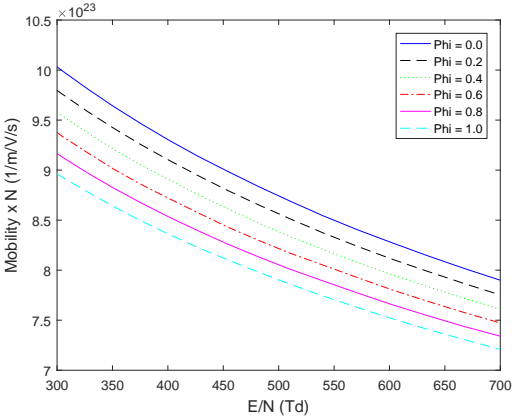
Figure 4.22: The discharge energy per pulse for methane-air mixture for different equivalence ratios, at atmospheric pressure and 3.4 l/min flow rate.

of electrons is required. These coefficients are evaluated by averaging corresponding cross-sections with the electron energy distribution function (EEDF). To obtain that, the electron Boltzmann equation has been solved numerically for  $N_2 : O_2 : CH_4$  mixtures using the BOLSIG+ solver<sup>1</sup>, Hagelaar and Pitchford (2005). Appendix D shows a list of the reaction rate coefficients for elastic, effective, excitation, ionization, and attachment reactions for oxygen, Nitrogen and Methane used in this study to calculate the electron energy losses and momentum losses due to collisions. A complete cross section data set for methane, nitrogen and oxygen is available on LXCat data exchange project ([www.lxcat.com](http://www.lxcat.com)).

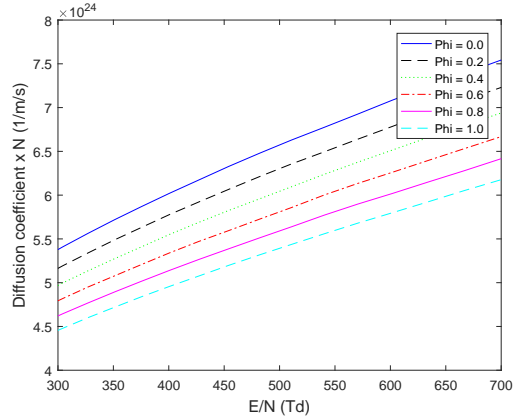
In Fig. 4.23, the reduced electron mobility  $\mu_e/N$ , the reduced diffusion coefficient  $D_e/N$ , the mean electron energy, and the reduced effective ionization coefficient  $\alpha_{\text{eff}}/N$  are given versus the reduced electric field  $E/N$ . The effective ionization coefficient  $\alpha_{\text{eff}}$  is given by the Townsend electron attachment coefficient  $\eta$  subtracted from the Townsend ionization coefficient  $\alpha$ . The Townsend coefficients  $\alpha$  and  $\eta$  are expressed in  $m^{-1}$ , and they represent the number of electrons formed or lost per unit length and normalized per electron, due to electron impact ionization and electron attachment, respectively. The simulations are performed for

<sup>1</sup>BOLSIG+ is a free program for the numerical solution of the Boltzmann equation for electrons in weakly ionized gases in uniform electric field conditions, which occur in swarm experiments and in various types of gas discharges and collisional low-temperature plasmas. Under these conditions the electron distribution function is non-Maxwellian and determined by an equilibrium between electric acceleration and momentum and energy losses in collisions with neutral gas particles.

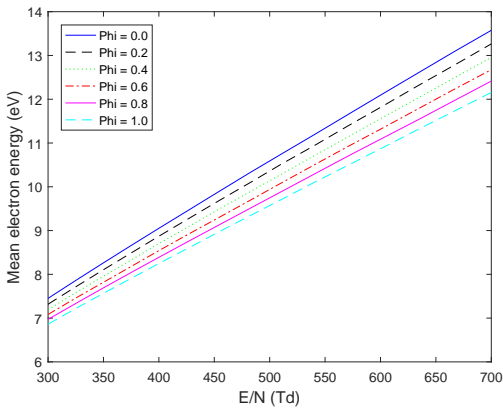
different equivalence ratios ranging from 0 to 1 at 300 K at atmospheric pressure. As shown in the figure, both electron mobility and diffusion coefficient are decreasing by the increase in the equivalence ratio of the mixture. This leads to a reduction in the mean electron energy. It can be also seen that the effective ionization coefficient in the methane-air mixture is close to that in air.



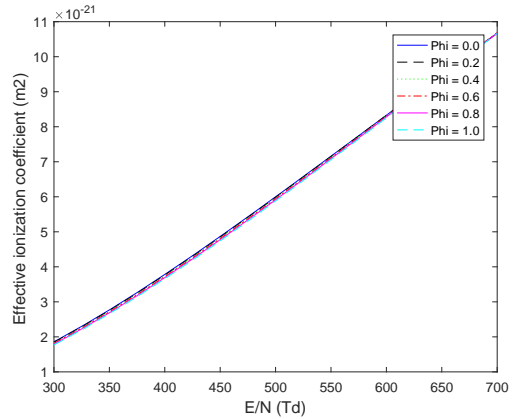
(a) Mobility  $\times N$  (1/mV/s)



(b) Diffusion coefficient  $\times N$  (1/m/s)



(c) Mean electron energy (eV)



(d) Ionization coefficient ( $m^2$ )

Figure 4.23: (a) The electron mobility, (b) the diffusion coefficient, (c) the mean electron energy, (d) the effective ionization coefficient versus the reduced electric field at different methane-air equivalence ratios. The cross section of electron collisions with  $O_2$ ,  $N_2$  and  $CH_4$  are given in Appendix D.

In addition to the ionization by electron impact, Naidis (2007) proposed another ionization process that has a substantial effect on discharge propagation. It is the production of precursor electrons ahead of the streamer front at absorp-

tion of ionizing radiation emitted by the streamer head. In air, the major source of precursor electrons is the ionization of  $O_2$  molecules by absorbing the photons emitted by excited  $N_2$  molecules. Adding  $CH_4$  leads to shortening of the length of propagation of ionizing radiation, as part of the photons are absorbed by methane molecules. The reduction in the electron energy as well as the reduction in the photo-ionization efficiency by increasing the concentration of  $CH_4$  in the mixture lead to reduction in the discharge energy as well as increase in the full-breakdown frequency.

## 4.10 Summary

In this chapter, we have presented the electric characteristics of our nanosecond plasma discharge. Special attention has been paid to the energy calculation as it is greatly influenced by the accuracy of the measurement of voltage and current. A new method for voltage and current synchronization is proposed. Pulse energies per channel of about  $1.46 \mu\text{J}$  and  $1.3 \mu\text{J}$  have been calculated from the current and voltage time-evolution at atmospheric pressure and 50 mbar, respectively.

Time-resolved optical emission spectroscopy measurements have been conducted to characterize the main thermal features of the plasma discharge in the DBD microplasma reactor. We have found that the discharge at low pressure is characterized by high vibrational temperatures (roughly 4000 K) and high effective reduced electric field strengths (10000 Td) compared to atmospheric pressure (3460 K and 550 Td), which indicates a higher electron energy at lower pressure.

Based on luminosity images, all gas flowing through the reactor can be assumed to interact with the plasma at 50 mbar. At higher pressures, the emission concentrates at the channel walls and not all gas is in direct contact with the plasma. The distribution of the plasma-generated radicals, however, is unknown. The luminous part of the plasma is strongly non-thermal, with vibrational temperatures of about 4000 K, but the gas temperature remains only a few degrees above ambient.

In addition, we have noticed that the discharge emission intensity slightly decreases by increasing the air flow velocity through the channels at atmospheric pressure due to the lower pre-ionization level at higher velocities. A reactor lifetime study showed around 100 minutes lifetime at low pressure. Nevertheless, more effort is needed to increase the lifetime of the reactor in order to transfer it to real applications.

Finally, the effect of the equivalence ratio on the discharge behavior has been investigated experimentally and numerically. We found that by increasing the equivalence ratio, the electron energy decreases while the ionization coefficient does not change. This leads to a reduction in the plasma intensity and increase in the full-breakdown frequency. In the next chapter, the developed reactor will

be used as a burner platform to study the effect of nanosecond discharges on the combustion characteristics.

## Effect of non-thermal plasma on flame stabilization and emissions

---

This chapter aims to address the effect of non-thermal plasma discharge on combustion characteristics. First, the laminar burning velocity of lean methane-air flames is measured, under different plasma conditions, using the flame area method. A comparison between the measured burning velocities at different plasma conditions and burning velocities obtained by numerical simulations at elevated temperatures has been performed to address the contribution of the thermal mechanism on the burning velocity enhancement. This is followed by a study of the lean blow-off limit at different operating pressures and plasma conditions. Also, the effect of plasma discharge on NO<sub>x</sub> emissions is presented.

---

### 5.1 Introduction

In recent decades, great efforts have been performed to reduce NO<sub>x</sub> emissions from the combustion products of gas turbines, aircraft engines, industrial burners and automotive engines. These efforts include and are not limited to exhaust gas recirculation, staging combustion, catalytic combustion, oxy-fuel combustion and lean premixed combustion. Lean combustion is promising but is limited by stability problems. One of the most promising ways to enhance stability in very lean conditions is to generate a sustainable source of reactive species in the combustion domain by so-called 'plasma-assisted combustion'.

Plasma-assisted combustion has gained a lot of attention over the last decades due to its capability to stabilize ultra-lean flames, decrease of ignition delay time, extend flammability limits and to increase the burning velocity (Kim et al. 2010;

Lacoste et al. 2013). A lot of fundamental research has been done to address different mechanisms by which non-thermal plasma enhances combustion characteristics.

Many types of power sources, like AC discharge (Choi et al. 2005), DC discharge (Korolev and Matveev 2006), microwave discharge (Stonies et al. 2004) and RF discharge (Bonazza et al. 1992), have been used to generate plasma discharges in combustion applications. Among all these types of plasma discharges, nanosecond-pulsed discharge is considered a very active source of highly energetic electrons and reactive species (Moselhy and Schoenbach 2003; Li et al. 2016). In addition, the non-thermal nature of nanosecond-pulsed discharges helps to avoid excessive gas heating which leads to thermal NO<sub>x</sub> production.

In addition, the dielectric barrier discharge scheme (DBD) is considered as one of the most successful ways to reduce the chance of generating the undesired transition to arc formation, which usually comes along with high-voltage pulses. The presence of a dielectric layer between the electrodes reduces the electric field generated by a given charge density. This helps to generate a uniform discharge distribution and reduces the chances of glow to arc transition for atmospheric pressure applications.

In this chapter, we introduce a new burner platform that utilizes a dielectric barrier microplasma reactor to sustain a stable non-thermal plasma discharge in all of the holes of a perforated burner plate using a nanosecond high-voltage power source at atmospheric pressure. In this way, we ensure a close interaction between plasma discharge and gas mixture before burning. Figure 5.2 shows an example of a methane-air flame stabilized above the perforate plate during the plasma discharge.

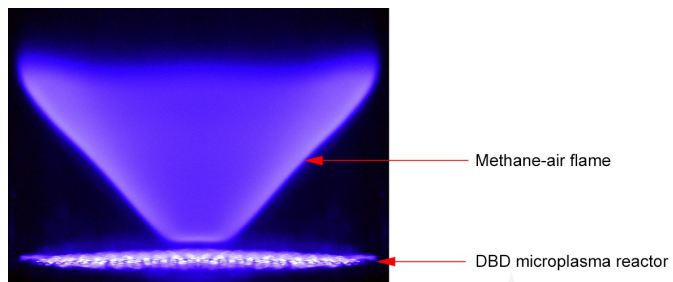


Figure 5.1: Image of the DBD microplasma burner and lean methane-air flame.

The main goal of this setup is to study the effects of the nanosecond plasma discharge on the burning velocity and the combustion chemistry of methane-air flames at atmospheric pressure over a broad range of plasma and flame conditions. Additionally, the lean flammability limit has been investigated for different equivalence ratios at different operating pressures. Then, the effect of plasma discharge on the flame emission, specially the NO<sub>x</sub> emission, will be studied and

Table 5.1: The characteristics of the annular and central channels.

	Annular channels	Central channels
Channel diameter (mm)	0.40	0.35
Area per channel (mm <sup>2</sup> )	0.13	0.10
Number of channels	344	19
Total area of the channels (mm <sup>2</sup> )	43.23	1.83
Coverage area (mm <sup>2</sup> )	296	18.10
Porosity (%)	14.6	10.10

presented. In order to be consistent with the previous analysis of the reactor, a minor modification to the reactor has been performed in order to obtain a V-shape flame. In the first part of this chapter we will present this modification in detail.

## 5.2 Modification of the reactor geometry

In this study, a V-shape flame is created to calculate the bunging velocity not affected by heat transfer to the perforated plate using the flame area method, which will be explained in details later. A minor modification to the reactor configuration in Fig. 2.3 has been made to produce a V-shaped flame. As shown in Fig. 5.2, the new configuration contains exactly the same number of channels with the same pattern. However, the diameter of 19 channels in the center of the reactor have been reduced to be 0.35 mm instead of 0.4 mm, while keeping the rest of the channels (annular channels) with a diameter of 0.4 mm. We tried to generate the same plasma strength between the two sets of holes. This was achieved by increasing the width of the copper electrode in order to keep the same dielectric width of 0.2 mm. This modification creates a small flow restriction in the central part of the device.

A comparison between the annular channels and the central channels is given in Table 5.1. The reactor porosity in the annular area (14.6%) is slightly higher than the central area (10.1%). This leads to a larger flow restriction in the center of the reactor. This flow restriction helps the flame to stabilize at the center of the device, see Fig. 5.1. Additionally, the small holes in the center provide a plasma discharge to the flame base, which is considered the closest point to the reactor. In this way we ensure the best interaction between the plasma and the plasma discharge.

## 5.3 Burning velocity measurements

Several methods are available to accurately determine the burning velocity of premixed flames. Some of these methods are the counterflow flame method (Park et al. 2011), spherical flame method (Sun et al. 2007), Bunsen flame method (Rallis



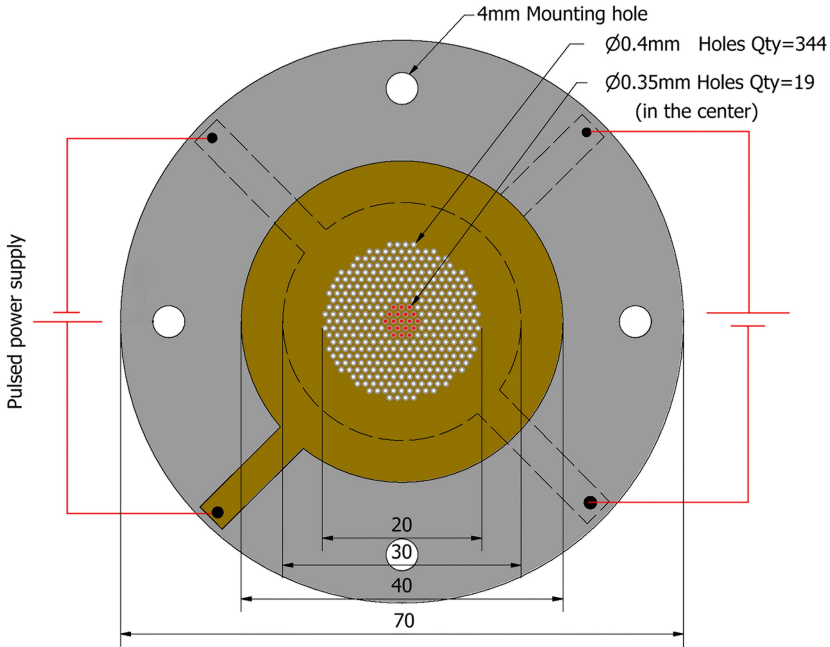


Figure 5.2: Schematic of the modified DBD microplasma reactor used to as a burner disk. The channels in the center are 0.05 mm smaller in diameter than the rest of the channels to create a flow restriction in the center.

and Garforth 1980) and heat flux method (Bosschaart and De Goey 2004). One of the simplest and accurate methods is the conical flame area method (Natarajan et al. 2009), where the flame is stabilized on the rim of a cylindrical tube.

Here we are proposing a similar method where the flame has an inverted conical shape and stabilized at its base, as explained earlier. The flame shoulders are not perfectly straight, but rounded at the base and curved at the top due to the heat transfer to the tube and boundary layer effects. Also, the velocity distribution is not perfectly uniform. So, the flame is affected by strain and flame curvature, which in turn affects the burning velocity. The average value of the burning velocity  $S_L$  can be obtained by dividing the gas mixture volume flow rate  $Q$  by the conical area of the flame front  $A_{flame}$ .

$$S_L = Q/A_{flame} \quad (5.1)$$

To accurately determine the flame area, CH\* chemiluminescence images taken by a Nikon camera model D5200 fitted with 50 mm focal length and CH\* band-pass interference filter (430 nm central wavelength with a full-width at half-height of 11.2 nm) have been used. A CH\* chemiluminescence analysis has been used to

avoid errors in the area calculation due to flame luminosity. Account is taken for the axial symmetry of the flame (see Fig. 5.3).

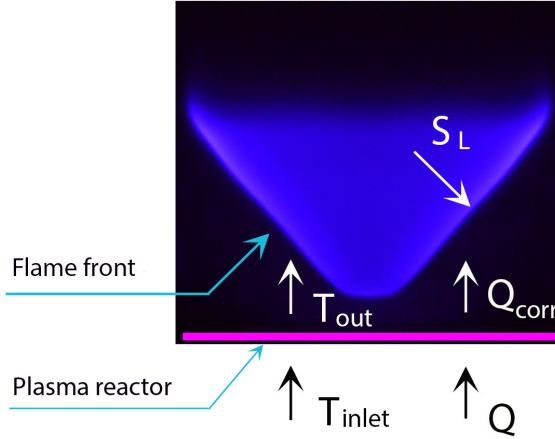


Figure 5.3: Schematic for the flame area method to measure the laminar burning velocity  $S_L$ .

This method has been validated by comparing the base-case results (without plasma discharge) with other published experimental and numerical (GRI-mech 3.0) results on the burning velocity of methane-air mixtures at atmospheric conditions (Wang et al. 2012; Bosschaart and De Goey 2003; Gu et al. 2000; Vagelopoulos and Egolfopoulos 1998; Tahtouh et al. 2009). As shown in Fig. 5.4, the present experimental results show a good agreement with published data with a slight over-estimation at very lean conditions.

In the case of plasma discharge, a correction has been made for the flow rate calculation to account for the mixture thermal expansion due to plasma heating effect to the gas mixture, see Fig. 5.3.

$$Q_{corr} = Q \cdot (T_{out}/T_{inlet}) \quad (5.2)$$

Where  $Q_{corr}$  is the corrected volume flow rate,  $Q$  is the inlet flow rate,  $T_{out}$  is the mixture temperature downstream the reactor and  $T_{inlet}$  is the inlet mixture temperature.  $T_{out}$  is calculated on the bases of the total consumed energy at the corresponding equivalence ratio.

To illustrate the effect of the plasma discharge on the laminar burning velocity, Fig. 5.5 shows  $CH^*$  chemiluminescence images of methane-air premixed flames

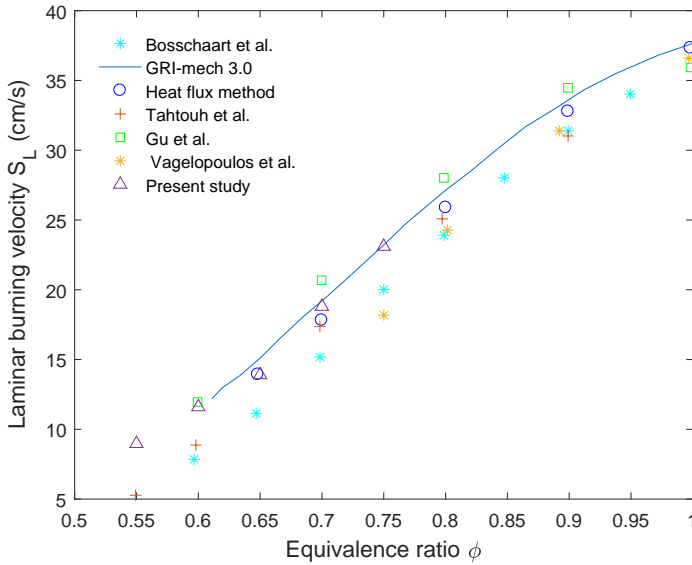


Figure 5.4: Validation of laminar burning velocity measurements in the present study by comparison with published data for methane-air mixtures at  $p = 1$  bar and  $T_{inlet} = 300$  K.

at different equivalence ratios, ranging from 0.55 to 0.75, and a plasma voltage of 5 kV at atmospheric pressure and different pulse repetition rates. For instance, at equivalence of 0.6, and in the absence of plasma discharge, the flame has a conical shape, with a 5 mm base, anchored at the central position. The figure shows a reduction in the flame front area by 27% at a pulse repetition rate of 10 kHz. At this condition, an increase of 22% in the mixture flow rate as a result of the heating effect due to the plasma discharge has been derived. This shows an overall increase in the burning velocity of about 66%. Table 5.2 shows the percentage of the plasma power to the flame power for methane-air flames at different equivalence ratios and pulse repetition rates. It is a small fraction (max 7%) of the flame power.

Figure 5.6 shows an overview on the effects of pulse repetition rate at different equivalence ratios on the laminar burning velocity of methane-air flames at atmospheric pressure and initial gas temperature of 300 K and a voltage of 5 kV. The plasma discharge, promoted by thermal and chemical enhancement mechanisms increases the laminar burning velocity. This enhancement depends on the mixture equivalence ratio  $\phi$ , discharge repetition rate  $F$ , the flame power and the flame to plasma distance. These factors can also identify the relative weight of

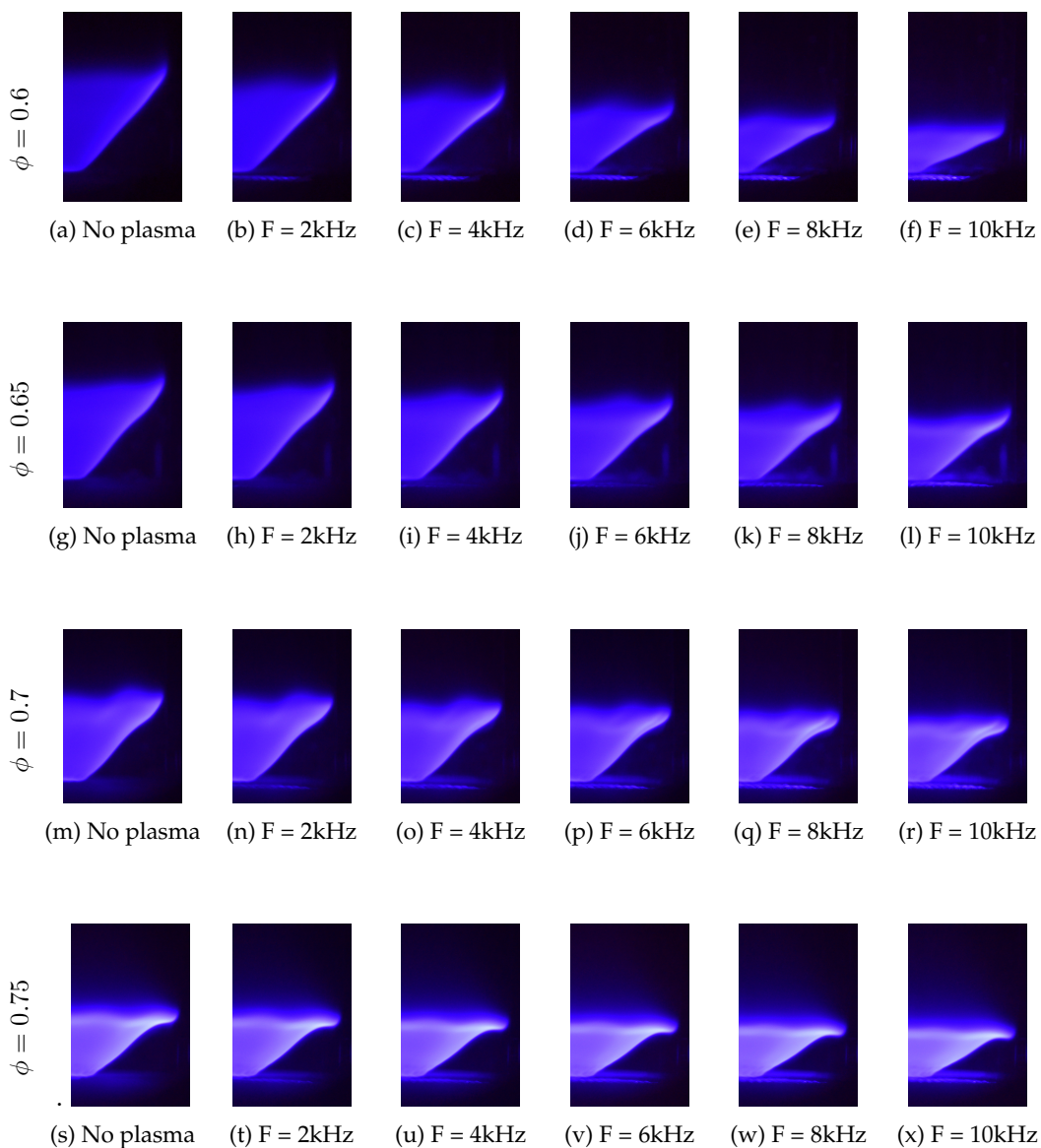


Figure 5.5:  $\text{CH}^*$  chemiluminescence images for methane-air flames at different equivalence ratio ( $0.6 \leq \phi \leq 0.75$ ) and at different pulse repetition rates ( $0 \text{ kHz} \leq F \leq 10 \text{ kHz}$ ). All at plasma voltage 5 kV and the inlet mixture temperature is 300 K.

Table 5.2: Percentage of the plasma power to the flame power (%) for methane-air flames at different equivalence ratios and pulse repetition rates at atmospheric pressure. All at plasma voltage of  $V = 5$  kV and inlet mixture temperature is 300 K.

Equivalence ratio	Flow rate (l/min)	Pulses repetition rate (kHz)				
		2	4	6	8	10
0.55	2.55	1.55 %	3.09 %	4.64 %	6.18 %	7.73 %
0.60	3.40	1.06 %	2.13 %	3.19 %	4.25 %	5.31 %
0.65	4.43	0.75 %	1.51 %	2.26 %	3.02 %	3.77 %
0.70	5.45	0.57 %	1.14 %	1.71 %	2.28 %	2.85 %
0.75	5.96	0.49 %	0.97 %	1.46 %	1.94 %	2.43 %

each mechanism to enhance the burning velocity. According to the figure, for very lean conditions ( $\phi = 0.55$ ), the plasma discharge is capable to increase the burning velocity from 8.5 cm/s to 16.6 cm/s, which is about 100% enhancement, at a pulse repetition rate of 10 kHz by supplying 7.9% of the flame power. At higher equivalence ratio, the influence of the plasma on the burning velocity is less significant. For instance, at an equivalence ratio of ( $\phi = 0.75$ ), the enhancement of laminar burning velocity at a pulse repetition rate of 10 kHz is only about 26%. We can explain this reduction of the plasma effect by two reasons. First, the plasma/flame power ratio decreases with increasing the equivalence ratio, as shown in Table 5.2. The second reason is the reduction in the amount of plasma species and radicals as a result of the increasing the amount of fuel in the mixture, as mentioned earlier in Section 4.9.2.

## 5.4 Thermal contribution to the burning velocity enhancement

This section is dedicated to estimate the contribution of the thermal mechanism to burning velocity enhancement. To achieve that, a steady one-dimensional simulation has been developed, using the CHEM1D solver (Somers 1994), to compare the experimental burning velocity enhancement using plasma discharge and the enhancement using an elevated inlet gas temperature only (numerically) at the same flow condition. The detailed GRI-Mech 3.0 chemical mechanism, which contains 325 reactions and 53 species, has been implemented in this study. A mesh with 100 adaptive grid points and a mixture-average transport model has been used.

The simulations have been done at elevated temperatures corresponding to those produced by the plasma discharge for a methane-air flame with an equiv-

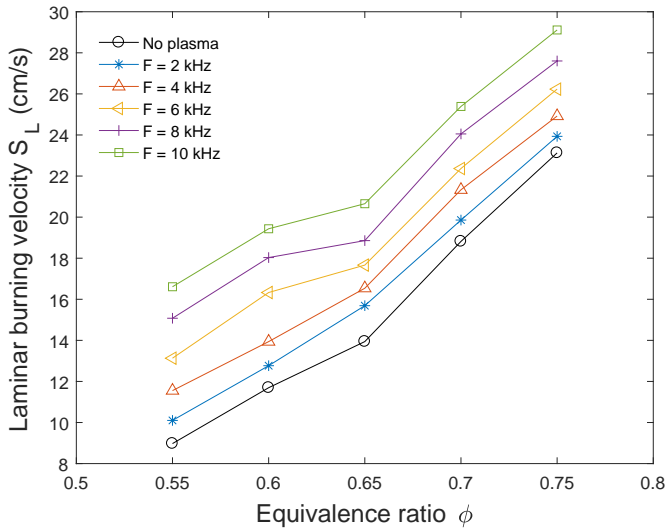


Figure 5.6: Effect of plasma discharge frequency ( $F$ ) on the laminar burning velocity ( $S_L$ ) of methane-air mixtures at atmospheric pressure. The pulse repetition rate of the plasma discharge ranges from 0 (no plasma) and 10 kHz, the initial gas temperature is 300 K and the plasma voltage is 5 kV.

alence ratio of 0.6. The temperatures of the inlet gas mixture at different plasma frequencies are measured using the same technique as described earlier in Section 4.5.3 but for methane-air mixtures with a volume flow rate of 3.4 l/min. Figure 5.7 shows the burning velocities at different pulse repetition rates (in blue), and simulated burning velocities by CHEM1D at elevated temperatures (in red).

The results indicate that the thermal effect of the plasma discharge is the dominating mechanism for the burning velocity enhancement. However, there is a small contribution (5-10%) due to other mechanisms, like kinetic and transport which can be extracted from the difference between the experimental and simulation results. Moreover, one can notice that this difference is slightly higher at high repetition rates. This can be attributed to the higher background ionization level at high repetition rates, as reported by Nijdam et al. (2011). This high background ionization can increase the concentration of the long lifetime species, which may play a role in the increase of the burning velocity. In Chapter 6, the local effect of the plasma discharge on the burning velocity will be investigated further using the PIV technique.

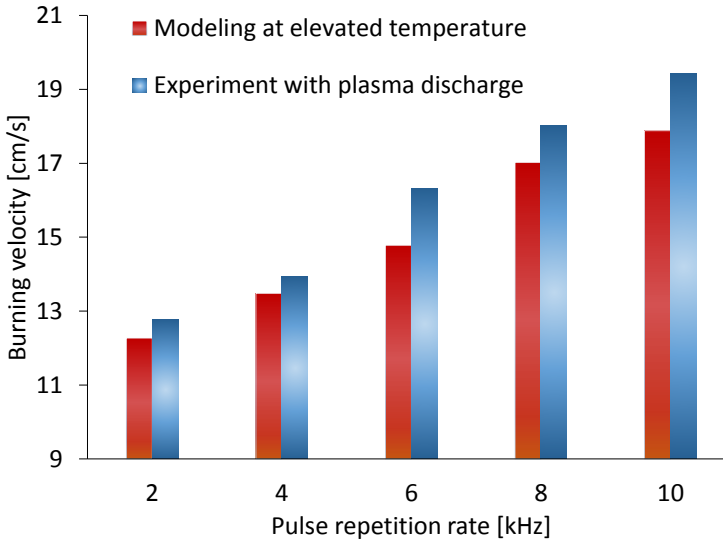


Figure 5.7: A comparison between the effect of plasma discharge (in blue) and the thermal effect (simulated by increasing the inlet mixture temperature (in red)) on the burning velocity, for methane-air flames at an equivalence ratio of 0.6 and mixture volume flow rate of 3.4 l/min.

## 5.5 Effect of plasma on blow-off limits.

An inverted flame can be considered as one of the most effective ways to study the flame stabilization mechanisms due to the absence of the interaction with the surrounding atmosphere at the point of stabilization. The stabilization of inverted flames occurs when a balance is achieved between the burning velocity at the flame base and the local mixture flow velocity. The stabilization mechanism of such flames has been studied intensively, during the last decades (Shoshin et al. 2013; Mallens et al. 2000; Edmondson and Heap 1970; Sung et al. 1992). The authors suggest two main mechanisms by which the inverted flame stabilizes. The first mechanism is the heat loss from the flame base to the stabilization plate. This mechanism assumes that the flame speed decreases when the flame approaches the stabilization disk to restore its original location, and vice versa. The second mechanism is the positive flame stretch rate at the flame base, which can lead to a reduction of local burning velocity and destroying thereby the balance between the flow velocity and burning velocity at the flame base.

In this section, the lean blow-off limit of methane-air flame is studied experi-

mentally for different plasma conditions at atmospheric pressure. These studies can provide fundamental insight into the capabilities of the ns-DBD plasma discharge on flame stabilization. The setups used in these studies are schematically shown in Fig. 3.1 and Fig. 3.6. The modified reactor, presented in Fig. 5.2 is used to anchor the flame in the center, as discussed earlier in this chapter. To measure the lean blow-off limits, the air mass flow rate was kept constant and the flame stabilization limit was approached by stepwise lowering the equivalence ratio until blow-off occurred. The plasma conditions are varied by changing the pulse repetition rate from 0 to 10 kHz with a step of 2 kHz. The voltage across the electrodes is kept constant at 5 kV.

Figure 5.8 shows the typical methane-air flame structures at different flow conditions, and Fig. 5.9 shows the lean blow-off limits of the flames for different plasma conditions and different air volume flow rates. The y-axis presents the lean equivalence ratio limit of the flame stabilization, and x-axis presents the air volume flow rate in the mixture. Any point above these curves represents a stable flame, while the flame does not exist below these curves. The effect of the central channels flow makes the interpretation of these results more complicated compared to the traditional bluff body or central rod configurations. As shown in the figure, for all the reported plasma conditions, the stabilization curves show a non-monotonic dependence of the blow-off limit on the air flow velocity. In the left part of the curves, at relatively low air flow rates, we can see that by increasing the air flow rate, the flame stabilization limit extends to lower equivalence ratio. At this range, the blow-off occurs from the flame base by losing the thermal contact with the burner disk, see Fig. 5.8 a, b and c. This reduction in the blow-off limits can be attributed to a combination effect of the increase in the flame curvature, stretch rate as well as the increase of the recirculating zone volume. The larger the flame curvature and stretch is the higher the burning velocity for flames with a Lewis number less than a unity (Yokomori et al. 2006; Egolfopoulos et al. 1989). Additionally, the strong recirculation zone, motivated by the high flow rate, works to widen the flame base and, hence, increases the contact area with the burner disk.

In the right part of the curves, the increase in the flow rate results in an increase in the flame base area, as shown in Fig. 5.8 d, e and f. This makes the flame more resistant to blow-off from the base. However, the strong aerodynamic acceleration produces flame stretch which reduces the flame diameter above the base, similar to what happens for premixed tubular flames (Chen and Ju 2008), forming a 'neck'. As lean limit equivalence ratio is decreased, flame fronts at the neck location become overlapping. Fuel conversion becomes incomplete, which leads to neck disruption and to blow-off of the flame (Vance et al. 2018). Similar behaviour has been reported by Shoshin et al. (2013) for rod-stabilized laminar inverted flames.

Lean blow-off limits for the same flames but with plasma discharge at different pulse repetition rates, ranging from 0 to 10 kHz, and voltage of 5 kV are also shown in Fig. 5.9. In general, the plasma discharge has a positive effect on the stability of the flame. The curves show a qualitatively similar trend compared to



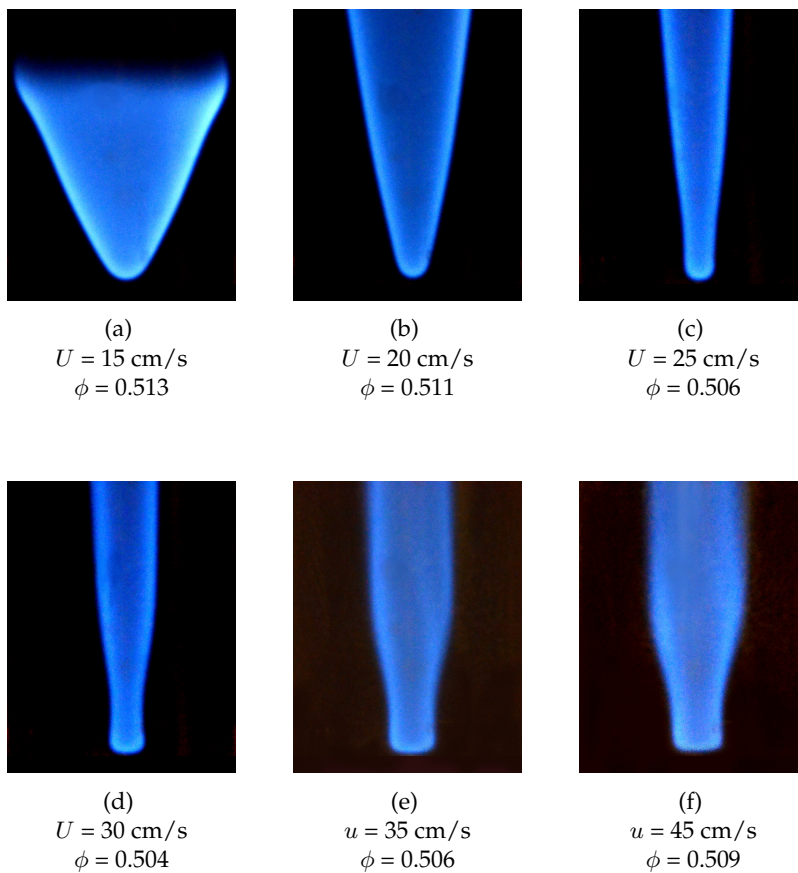


Figure 5.8: Methane-air flames near blow-off conditions for different gas flow velocities ( $u$ ) without plasma discharge. Equivalence ratios ( $\phi$ ) and gas flow velocity ( $u$ ) are mentioned below each figure.

the case without plasma discharge. The curves are slightly shifted to the right because of the density variation as a result of the plasma heating effect, which increases the volume flow rate for the same inlet flow conditions. The plasma discharge shows a reduction of about about 8% in equivalence ratio at the lean flame stabilization limit at the maximum pulse repetition rate. The effect of the plasma on the flame stability is slightly higher for the low-velocity part of the curves, where the flame blows-off from the base, and has a lower effect at the high-velocity part of the curves. This enhancement could be explained by the increase in the flow temperature as a result of the plasma discharge as well as the long-life species that can reach to the flame base.

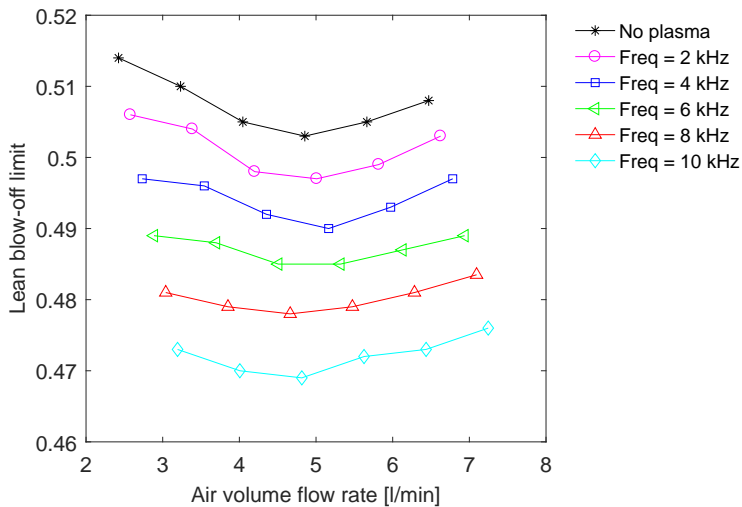


Figure 5.9: Effect of pulse repetition rate on lean blow-off limit of methane-air flames for different air flow rates at atmospheric pressure. The pulse repetition rates of the plasma discharge ranges from 0 to 10 kHz at peak voltage of 5 kV.

## 5.6 Nitric Oxides measurements

Quantitative measurements of NO and NO<sub>2</sub> have been performed for methane-air flames at different equivalence ratios ( $\phi = 0.55, 0.6, 0.65$  and  $0.7$ ) and at different pulse repetition rates of the plasma discharge. The modified reactor, presented in Fig. 5.2 is used in this study. The gas mixture flow rate as well as the plasma voltage were kept constant at 2.6 l/s and 5 kV, respectively, for all the experiments. A gas analyzer model MRU-AIR VARIO-plus with a water cooled probe of 0.8 cm water-jacket external tube diameter is used to sample the combustion products. The probe is located at a height of 10 cm above the burner disk along the tube

axis. The gas analyzer has a measuring range up to 1000 ppm of NO and NO<sub>2</sub> with an accuracy of 5%. To ensure a stable signal, a time-delay of two minutes after turning on the plasma discharge has been considered before sampling.

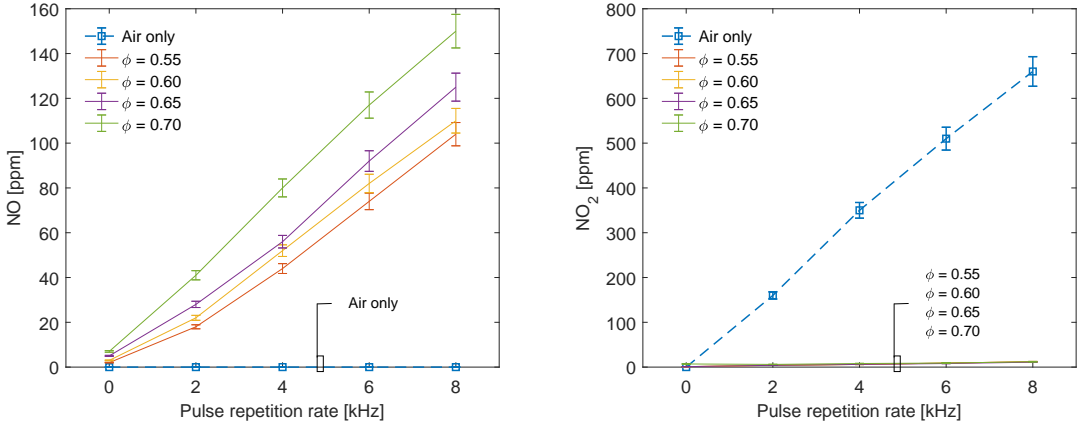
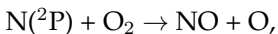
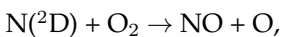


Figure 5.10: NO mole fraction (left) and NO<sub>2</sub> mole fraction (right) as a function of the pulse repetition frequency and equivalence ratio of methane-air flames at atmospheric pressure. The gas flow rate is 2.6 l/min and the plasma voltage is 5 kV.

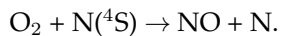
As shown in Fig. 5.10 (left), without plasma discharge, the NO concentration increases from 3 ppm to 8 ppm by increasing the equivalence ratio from 0.55 to 0.7. This is due to the increase in the flame temperature with increasing equivalence ratio. The main responsible reaction for the production of NO is  $O + N_2 \rightarrow NO + N$ , which has a high activation energy to break the triple bond of the nitrogen molecule (Turns 2000).

After turning on the plasma, one sees a linear relationship between the NO mole fraction and the pulse repetition frequency of the plasma discharge at all the flame conditions. The NO concentration reaches up to about 150 ppm at a pulse repetition rate of 8 kHz for equivalence ratio of 0.7, with an increase rate of 17.5 ppm/kHz. Slightly lower values have been observed at lower equivalence ratios. Uddi et al. (2009) investigated the production of NO in a nano-second high-pressure pulsed discharge activated DBD reactor and they attributed the production of the NO to the following reactions:



where the long-lived metastable  $N(^2D)$  and  $N(^2P)$  are produced by dissociative excitation of  $N_2$  ( $e + N_2 \rightarrow N + N + e$ ). The other source of NO is the Zel'dovich

reaction of oxygen molecules with ground state N atoms;



This reaction may occur at relatively high temperatures achieved in microstreamers of the DBD discharge at atmospheric pressure, as discussed previously in Section 4.3. For all equivalence ratios covered in this study, the produced  $\text{NO}_2$  mole fraction is very low (less than 2 ppm/kHz), as shown in 5.10 (right).

On the other hand, the situation for  $\phi = 0$  (air only) is different, where the measurements show a large amount of  $\text{NO}_2$  reaching 660 ppm at 8 kHz with a linear increase rate of 75 ppm/kHz, while there is almost no traces for NO at all. More investigations are needed to understand the reactions responsible for this behavior.

## 5.7 Summary and Conclusions

In this chapter, we demonstrated the possibility to increase the combustion stability of a lean premixed flame by the use of a non-thermal plasma discharge located in the perforated burner plate holes. An experiment to measure the laminar burning velocity has been done using the flame area method. A modification on the microplasma reactor was made to produce a V-shape flame.  $\text{CH}^*$  chemiluminescence image analysis has been performed to accurately determine the flame area. The validation of this method shows good agreement with other published data. The results show an increase of the burning velocity of about 100% in very lean ( $\phi = 0.55$ ) flames as a result of the plasma discharge effect. The results also show that the increase in the burning velocity depends on a number of factors, namely, equivalence ratio, pulse repetition rate, and plasma to flame power ratio. A comparison between the experimental and numerical results reveals that about 90% of the burning velocity enhancement is due to the increase in the mixture temperature as a result of the plasma discharge.

Secondly, the effect of the plasma discharge on the lean flame blow-off at atmospheric pressure has also been examined. Without plasma discharge, the obtained experimental curves have two different behaviors. At low flow rates, the increase in the flow rate results in reduction of the lean limit equivalence ratio. At these conditions, the flame blow-off occurs from its base. At high flow rates, the further increase in the flow rate, or, alternatively, reduction of the equivalence ratio, leads to the formation of a neck above the flame base. The flame blow-off at these conditions occurs through the stretch-induced flame extinction at the neck location. As higher mixture velocities produce stronger flame stretch rates, the limit equivalence ratios at this part increases with the increase of the air flow rate. By introducing the plasma discharge, the lean blow-off limit decreases about 8% at the maximum pulse repetition rate.

The plasma discharge also produces a significant amount of  $\text{NO}_x$  if the processed gas contains  $\text{N}_2$ . This raises doubts about the applicability of using plasma discharge in combustion application due to the environmental concerns. Effort is still needed to understand the mechanisms of the formation/destruction of  $\text{NO}_x$  and the possible treatment approaches to reduce the environmental impact.

# Effect of the plasma discharge on local burning velocity: A particle image velocimetry study

---

---

**I**n this chapter, we study the local effect of the nanosecond DBD microplasma discharge on the burning velocity of a methane-air flame obtained using particle image velocimetry (PIV) technique. The first section will present the working principle of the PIV technique, followed by a study to show the effect of the seeding density on the plasma discharge intensity and the consumed pulse energy. Then, the local burning velocity determination by PIV is presented and applied for a lean inverted premixed flame.

---

## 6.1 Introduction

As introduced in Chapter 5, plasma provides a way to enhance the combustion characteristics by increasing the burning velocity of premixed flames and extending the lean flammability limit. Some numerical and experimental efforts have been made toward understanding the main mechanisms responsible for the enhancement. However, these mechanisms are not quite clear till now, specially for nanosecond plasma discharges. This chapter considers another step toward the understanding of the influence of the plasma discharge on the flame characteristics by applying particle image velocimetry (PIV) to quantify the effect of the plasma on the local burning velocity of lean methane-air flames.

Particle Image Velocimetry (PIV) is considered as one of the most powerful and practical diagnostic tools for flow field analysis in fluid dynamics applications.

Instantaneous 2D and 3D flow velocity fields can be measured with high spatial and temporal resolution. It can be implemented with different techniques, i.e. planar, stereo and tomographic PIV among the most common ones. An overview on the planar technique, which is implemented in this study, will be presented. A more detailed review on the working principle of PIV can be found in literature (Raffel et al. 2007) and (Westerweel 1997).

For each mixture condition, an unstretched flame without plasma has a single value for the burning velocity regardless the measuring location, while the plasma may have a local effect on the burning velocity. The main objective of the present study is to investigate the local effect of the plasma discharge on the burning velocity for a conically shaped methane-air flame. The local burning velocity can give some information about the lifetime of the radicals which might lead to burning velocity enhancement. Another objective of this chapter is to study the flow field downstream the modified plasma reactor in the cold mixture and flame cases.

## 6.2 Working principle of PIV

PIV is a non-intrusive technique, which enables the measurement of the fluid velocity field in a plane of interest. The main principle is based on area illumination by a thin laser sheet and recording the light scattered by seeding particles at temporal moments separated by a known delay time. The typical PIV setup is presented in Fig 6.1. The tracer particles should be relatively small to not influence the flow field and to move with exactly the same speed as the gas flow, but also, large enough to be visualized and to avoid the uncertainty due to so-called 'pixel locking' if it occupies less than one pixel (Raffel et al. 2007). It is also important that the seeding particles are uniformly distributed within the flow field that needs to be examined. Additionally, a uniform particle size is desirable in order to avoid excessive radiation emission from large particles and background noise from the small particles.

Typically, in 2D planar PIV, tracer particles are illuminated two or multiple times, separated by a known time interval between the laser pulses. A laser sheet with a small thickness is used for the planer illumination. The illuminated particles are recorded by a camera on the same or separate frames.

The analysis of PIV can be performed in cross-correlation or auto-correlation modes. In the cross-correlation mode, two separate images are correlated together to define the displacement of particle. In auto-correlation mode, a single image is used for each frame to correlate multiple traces of the particles due to the pulsed illumination. Between two laser pulses, separated by a time interval ( $\Delta t$ ), the tracer particles move by  $\Delta x$  and  $\Delta y$  in a sub-domain window (known as interrogation window). The local velocity components can be derived from particle

(peak) displacement, as follows:

$$u = \frac{\Delta x}{\Delta t}, \quad (6.1)$$

$$v = \frac{\Delta y}{\Delta t}, \quad (6.2)$$

where  $u$  and  $v$  are the temporally averaged values for the axial and vertical velocity components over the time interval between two pulses and spatially averaged over the interrogation window. The integrated data from all the interrogation windows provides the velocity vector distribution in the measurement plane.

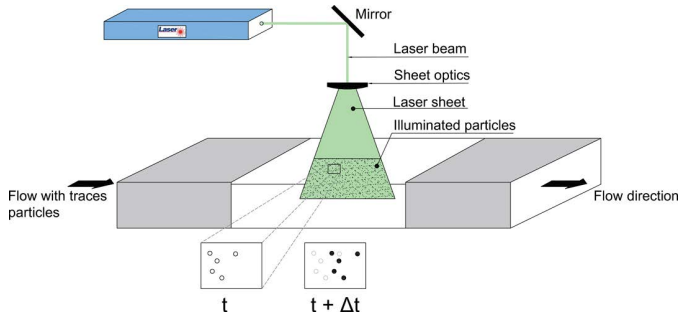


Figure 6.1: Principle of particle image velocimetry (PIV).

## 6.3 Experimental setup

A schematic of the PIV experimental setup used in this study is shown in Fig. 6.2. The flow is seeded with aluminum oxide ( $\text{Al}_2\text{O}_3$ ) particles with an average diameter of about  $1 \mu\text{m}$  using a custom-made motorized fluidized-bed seeding system, see Fig. 6.3. A bypass from the main flow stream is directed to the seeding system, with needle valves (V1 and V2), to control the seeding density. The seeding density can also be controlled by increasing the vibrational level of the fluidized-bed. The laser sheet illuminates the central plane of the burner and is aligned with a diametral row of the reactor channels. The diametral row contains 5 of the 0.35 mm channels in the center, and 7 of the 0.4 mm channels from each side. These 19 channels cover the entire effective diameter of the reactor.

The flame is protected by a quartz cylindrical tube of 40 mm diameter and 50 mm length to avoid flame fluctuations and ambient air penetration, which may affect the burning velocity measurements significantly. The tube diameter has been selected so that the flame does not touch the tube to avoid seeding particle accumulation on the tube wall, which would reduce the image quality significantly.



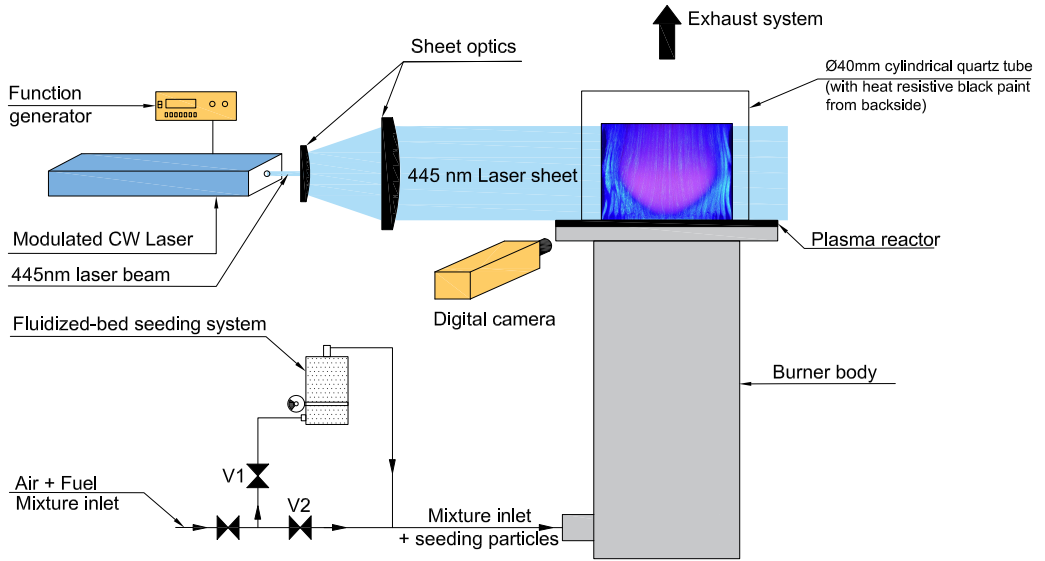


Figure 6.2: Schematic of experimental PIV setup.

and lead to inaccurate velocity measurements. To eliminate laser light reflections, the inner backside of the tube is painted by thermally resistant black paint.

A commercial 5 Watt continuous power DIY Laser, with a central wavelength of 445 nm, is used to illuminate the region of interest. The laser output is externally modulated by applying a standard TTL signal using a FeelTech frequency generator model FY2102S. A pulse repetition rate of 10 kHz, a time delay of 100  $\mu$ s, with 10% duty cycle (a fraction of one cycle in which a signal is active) was used in this experiment. These repetition rate and duty cycle are optimized to resolve both high velocities in the flame and low velocities prior the flame. A uniform 5 cm wide laser sheet is produced by a combination of a 20 mm focal length cylindrical lens and a 100 mm focal length spherical lens, which produces a nearly constant width of 0.5 mm width laser sheet.

The raw PIV images are post-processed using PIVview2C software GmbH (GmbH), using the auto-correlation mode. Single-exposed images with an exposure time of one second were used. This allows to register the same particle about 200 times on the same frame and to minimize the particle seeding density required to produce velocity measurements with high spatial resolution. The im-

ages are recorded by a D5100 Nikon camera with a digital resolution of 16.2 Mega-pixels fitted with micro-Nikkor lens with a 60 mm focal length. The camera was mounted facing the laser sheet as sketched in Fig. 6.2. Rectangular interrogation areas of 60x60 pixels (0.3 mm x 0.3 mm) with a 50% overlap were chosen.

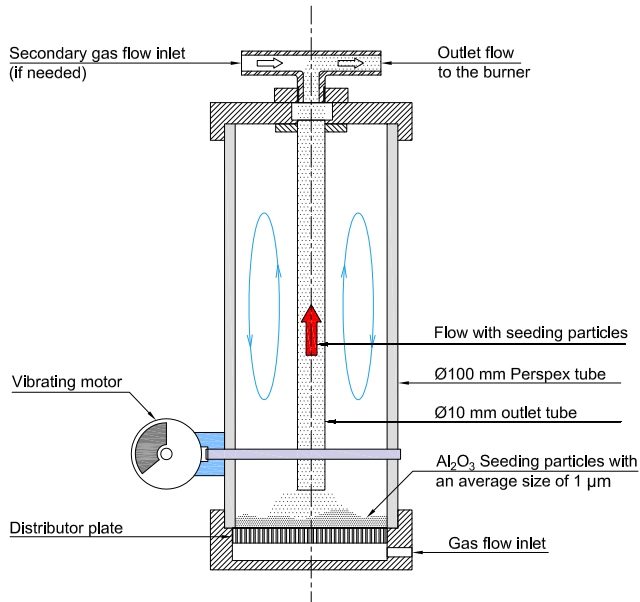


Figure 6.3: Schematic of the fluidized-bed seeding system.

## 6.4 Effect of seeding particle density on plasma discharge

The uncertainty of the PIV measurements is influenced by many factors, such as interrogation window size, seeding particle size, particle shift, background noise and the seeding particles density. One of the parameters which may affect the plasma discharge in microstructure and has a direct effect on the PIV uncertainty is the seeding particle density. Seeding density denotes the number of particles per unit volume. Raffel et al. (2013) shows that a larger seeding density will reduce the velocity measurement uncertainty significantly. However, before applying the seeding particles in a flow passing through a plasma discharge, we have to examine the effect of the seeding particles density on the plasma discharge from two perspectives. First, the pulse energy; to show the effect of the seeding density

on the drawn current by the plasma discharge. The second perspective is the spectra intensity of the discharge. Figure 6.4 shows short exposure images, where the particles are continuously illuminated by the laser source (100% duty cycle) and captured with an exposure time of  $1/4000$  second, for the flow downstream of the reactor at different seeding particle densities. The air flow rate is kept constant at  $3.4$  l/min and the particle seeding densities are changed by increasing the vibration level of the fluidized bed seeding system. These images are only considered for the seeding density calculation and not for velocity measurements. Seeding densities are calculated using an experimentally determined laser sheet thickness of  $130$   $\mu\text{m}$ .

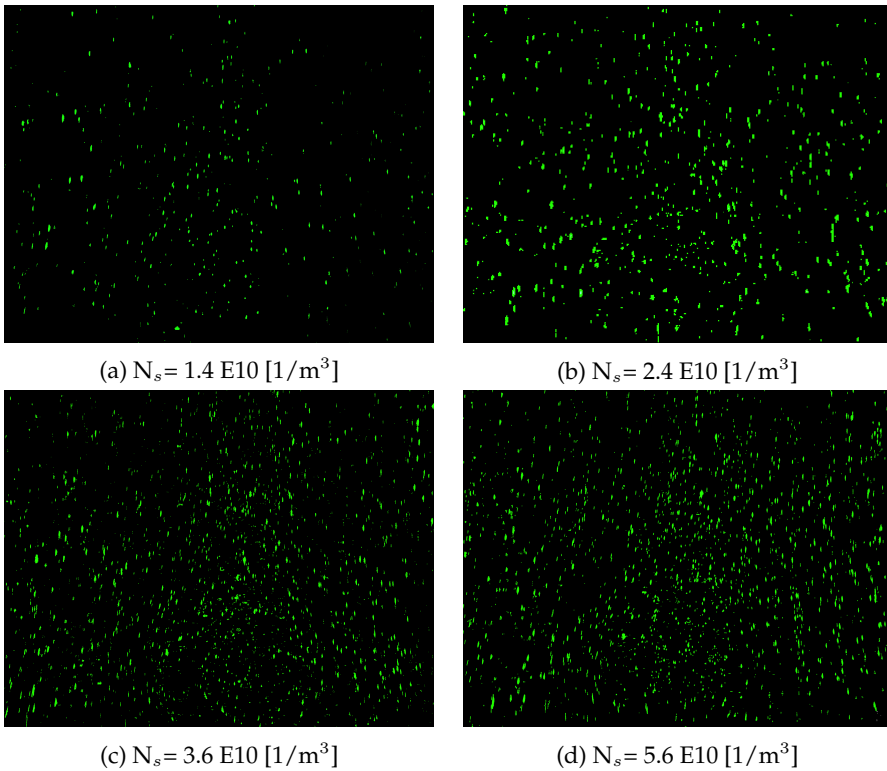


Figure 6.4: Images of seeding particles illuminated by the laser sheet downstream of the plasma reactor for different seeding particles densities (The seeding particles are shown in a green color). All the images are taken for an air flow rate of  $3.4$  l/min and an exposure time of  $1/4000$  second at atmospheric pressure.

Figure 6.5 shows the dependence of the pulse energy on the seeding particle density for an air flow rate of  $3.4$  l/min and a voltage of  $4$  kV. The pulse energies are calculated based on the method reported previously in section 4.2. The figure shows that the pulse energy variation is almost negligible, and lies within the

uncertainty range, when increasing the seeding particle density from 0 to  $5.6 \times 10^{10} \text{ 1/m}^3$ . This can reveal that the consumed current by the plasma discharge is almost constant and unaffected by the seeding density in this operating range.

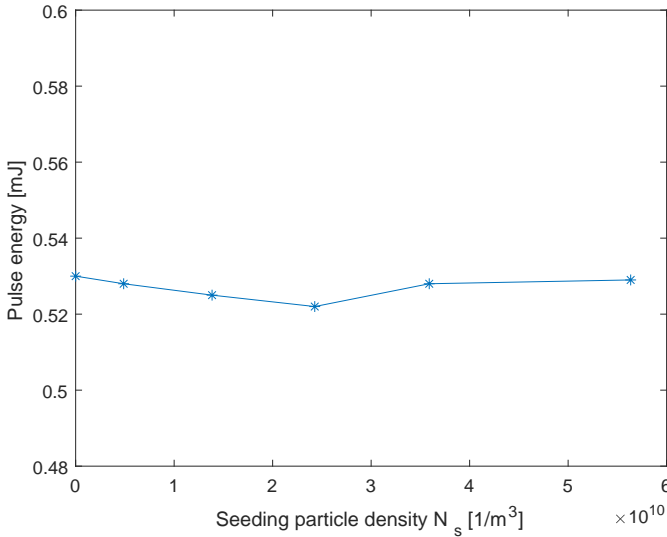


Figure 6.5: Pulse energy as a function of the seeding particle density for an air flow rate of 3.4 l/min and a pulse repetition rate of 3 kHz at atmospheric pressure and 5 kV.

Consuming the same amount of current does not necessarily mean producing the same plasma discharge intensity. Some of the plasma discharge may be quenched by the seeding particles. To test this, a comparison between the spectra intensities, for a wavelength range between 320 nm to 390 nm, for different seeding densities has been performed, as shown in Fig. 6.6. The spectra are calculated for 100 ns after the onset of the incident pulse, accumulated for 10,000 pulses, pulse repetition rate of 3 kHz and air flow rate of 3.4 l/min. The comparison shows also a minor effect of the seeding density on the plasma discharge intensity.

This effect can be explained by two reasons. The first is that, at atmospheric pressure, the plasma discharge is focused only in an annulus on the inner wall of the channel, as shown in Fig. 4.5a. At this location, the flow velocity is very low due to the boundary effect and, consequently, the probability of existing the particles is very low compared to the center of the channel. This eliminates the effect of the seeding particles on the plasma discharge. The second reason can be related to the big difference in time scale between the high-voltage pulses (nanosecond timescale) and the seeding flow (millisecond timescale), as shown previously in Fig. 4.17. From this study, we can say that applying PIV technique to measure the

velocity distribution for a flow passing through a nanosecond plasma discharge in the DBD micro-structure is possible as the plasma is unaffected by the seeding density in the range covered in this study.

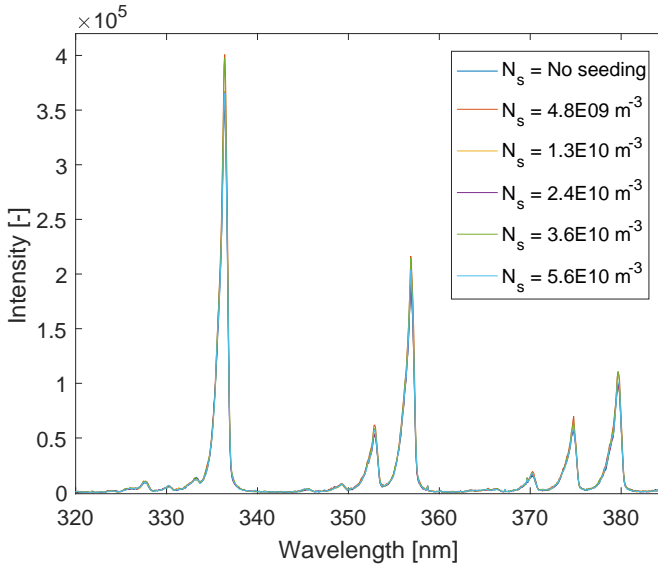


Figure 6.6: Non-normalized emission spectra in air at atmospheric pressure for different seeding densities ranging from 0 to  $5.6 \text{ E}10 \text{ m}^3$ . The plasma voltage is 5 kV with a pulse repetition rate of 3 kHz. The emission spectra are calculated at 100 ns after the onset of the indecent pulse and are accumulated for 10,000 pulses.

## 6.5 Velocity measurements

Figure 6.7 shows images for a methane-air mixture with a flow rate of 3.4 l/min and an equivalence ratio of 0.6 for (a) a cold flow and, (b) a flame. The Mie scattered light from the seeding particles (colored in green for visualization purpose only) shows clearly the flow structure in both cases. As seen in the images, in the cold flow case, a recirculation zone is formed in the center of the reactor in the downstream direction. This is due to the velocity difference between the central and the annular gas flows as a result of the porosity difference between the central part and the annular part of the reactor, which is shown previously in Table 5.1. This creates a reversing flow towards the center of the reactor. Under this flow condition, the maximum length of the recirculation zone along the centerline, which is called the aft stagnation point, is about 5 mm.

On the other hand, in the case of a flame, as shown in Fig. 6.7(b), we noticed the absence of the recirculation zone behind the reactor. This can be explained by the

high flow acceleration at the flame base due to the elevated temperature compared to the annular flow stream. This expands the flow of the central channels outward in radial direction.

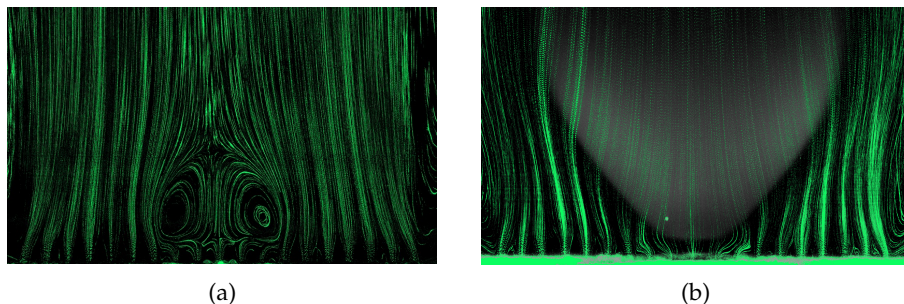


Figure 6.7: Flow visualization images for a gas mixture with a flow rate of 3.4 l/min, (a) for a cold flow case, (b) for a flame with an equivalence ratio of 0.6. The green color is for the seeding particles. Laser frequencies are 6 kHz for the cold flow and 10 kHz for the hot flow. Camera exposure time of 0.2 second with f-stop of f/5 and ISO speed of 2500 are used.

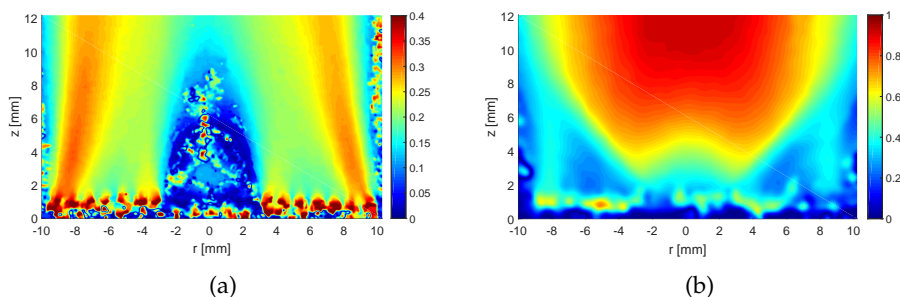


Figure 6.8: The experimental velocity distribution from PIV measurements for a gas mixture with a flow rate of 3.4 l/min, (a) for the cold flow case, and for (b) the flame case. The PIV conditions are mentioned in Fig. 6.7.

## 6.6 Local burning velocity measurements

In chapter 5, the effect of a non-thermal plasma discharge on the overall burning velocity of methane-air flames has been investigated by the flame area method. However, the plasma discharge may induce a local enhancement in the burning velocity depending on the distance between the reactor and the flame front. The local enhancement, if any, can be due to the presence of plasma generated radicals.

In this section, the local burning velocity of a conical flame will be derived from the stream-tube method. Stream-tube method uses the velocity vector distribution from PIV measurements to define two stream lines, so called 'stream-tube', where continuity of mass flow can be applied between them. For a cylindrically symmetric flow, a 'stream-tube' is actually a solid of revolution formed by rotating two neighbor streamlines around the flow symmetry axis. In the following section, the equations which govern the burning velocity based on the stream-tube method will be presented.

### 6.6.1 Governing equations

The stream-tube method (Shoshin and Jarosinski 2009) is based on the continuity of the mass flow along a stream-tube, see Fig.6.9:

$$\rho \cdot v \cdot A_{\perp} = const. \quad (6.3)$$

Let us define the mass burning velocity ( $m_b$ ) of the mixture by

$$m_b = \rho \cdot s_L \quad (6.4)$$

where  $\rho$  and  $s_L$  are the local gas density and local flame speed normal to the flame front. The perpendicular area at the inlet of the stream tube ( $A_{1\perp}$ ) can be written as

$$A_{1\perp} = A_1 \cos \alpha \quad (6.5)$$

here  $A_1$  is the intersection area between the flame front and the steam-tube, and  $\alpha$  is the angle between the flame front isothermal plane and the stream-tube diagonal plane at the intersection location.

The burning velocity at any specific location is assumed to be equal to the flow velocity normal to the flame front at this location, which can be written as;

$$s_L = v_1 \cos \alpha \quad (6.6)$$

where  $v_1$  is the flow velocity normal to the stream-tube cross section at the flame front location. We can apply the continuity of the mass, equation Eq.6.3, on the stream-tube between the flame front (point 1) and the exit from the tube (point 2), as follows;

$$\rho_2 \cdot v_2 \cdot A_{2\perp} = \rho_1 \cdot v_1 \cdot A_{1\perp} \quad (6.7)$$

By substituting Eq. 6.5 for  $A_{1\perp}$  and Eq. 6.7 for  $v_1$  in Eq. 6.7, one can get:

$$\rho_2 \cdot v_2 \cdot A_{2\perp} = \rho_1 \cdot A_1 \cdot \cos \alpha \cdot \frac{s_L}{\cos \alpha} = \rho_1 \cdot s_L \cdot A_1 \quad (6.8)$$

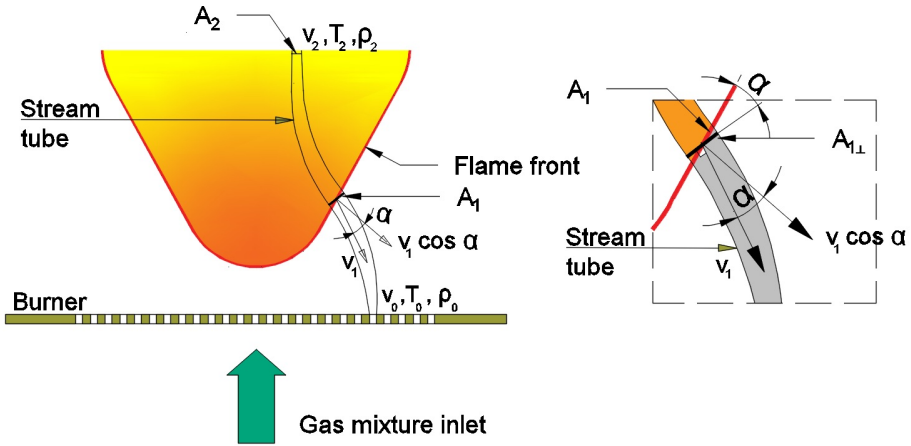


Figure 6.9: Schematic of stream-tube method.

From Eq. 6.4 and Eq. 6.8 we obtain the mass burning velocity:

$$m_b = \frac{\rho_2 \cdot v_2 \cdot A_{2\perp}}{A_1} \quad (6.9)$$

The required burning velocity, which is corresponding to the inlet gas temperature, can be given by:

$$L_b = s_L \cdot \frac{\rho_1}{\rho_0} \quad (6.10)$$

From Eqs. 6.8, 6.9 and 6.10

$$L_b = \frac{\rho_2}{\rho_0} \cdot \frac{A_{2\perp} \cdot v_2}{A_1} \quad (6.11)$$

The density ratio  $\frac{\rho_2}{\rho_0}$  is equal to  $\frac{T_0}{T_2}$ , assuming ideal gas law. So, we get : From Eqs. 6.4, 6.9 and 6.10

$$L_b = \frac{T_0}{T_2} \cdot \frac{A_{2\perp} \cdot v_2}{A_1} \quad (6.12)$$

From Eq. 6.12, we can see that the burning velocity determination by this technique requires measuring the following parameters:

- The inlet mixture temperature ( $T_0$ ).
- The temperature of products at the exit of the steam tube ( $T_2$ ).
- The area of the flame front at the intersection location with the stream-tube ( $A_1$ ).



- The area of the stream-tube at the exit plane ( $A_{2\perp}$ ).
- The gas velocity at the exit of the stream-tube ( $v_2$ ).

PIV measurement provides the velocity vector components ( $u$  and  $v$ ) at each node ( $x$  and  $y$ ) in the domain. This enables us to define the stream-tubes by using the built-in MatLAB function 'streamline'. This function allows to define the location, the required width and the starting points of the stream tubes. The width of the stream-tubes should not be too small, to avoid an uncertainty in area determination. However, it should not also be too large where the number of stream-tubes will be limited, which limits the spatial resolution of the local burning velocity measurements. The flame front location has been determined by performing an Abel inversion on the flame images. The Abel inversion is used to extract the radial (2D) distribution from a one-dimensional projection measurement.

The flame front is assumed to be located at the maximum intensity of the flame luminosity after the Abel inversion. Fig. 6.10 shows a chemiluminescence image for a flame at an equivalence ratio of 0.6 and flow rate of 3.4 l/min (left image), and the same flame after Abel inversion (right image). To accurately determine the flame areas at the entry and exit sections of the stream-tube,  $A_1$  and  $A_{2\perp}$  respectively, a 3D representation of the stream-tube is generated by revolving it around the flame centerline using a 3D AutoCAD software, see Fig. 6.11. The program calculates the entry and exit surface areas automatically. This is obtained for all the stream tubes in the flame as well as all flames at different plasma conditions.

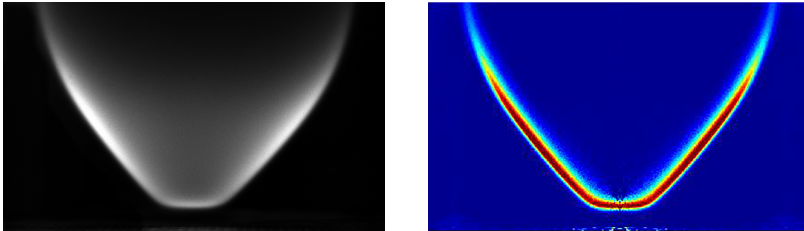


Figure 6.10: (Left) natural chemiluminescence image of a methane-air flame with an equivalence ratio of 0.6 and mixture flow rate of 3.4 l/min. (Right) Abel inversion for the same flame.

### 6.6.2 Temperature measurement.

Determination of local burning velocity by the stream-tube method requires temperature measurement of the combustion product at the stream-tube exit as mentioned earlier in this section. In this experiment, the temperature was measured by a bare wire S-type thermocouple (Platinum Rhodium - 10% / Platinum) at a

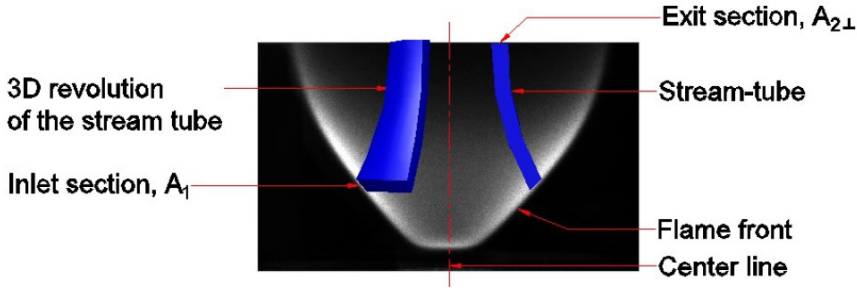


Figure 6.11: 3D representation of one steam-tube for methane-air flame with an equivalence ratio of 0.6 and mixture flow rate of 3.4 l/min. The schematic shows the entry section area  $A_1$  and exit section area  $A_{2\perp}$  used for burning velocity determination by the stream-tube method.

distance of 12 mm from the burner. The thermocouple junction was nearly a perfect sphere with a diameter of  $200 \pm 25 \mu\text{m}$  for a wire diameter of  $100 \mu\text{m}$ . The thermocouple wires are inserted in a two-holes high-temperature ceramic tube with an external diameter of 5 mm and length of 30 cm. A stainless steel protection tube with an internal diameter of 6 mm and a wall thickness of 0.5 mm is used to protect the ceramic tube from any mechanical shock during operation. A thermocouple reader model OMEGA HH506RA is used to read the temperature measurement. The device has an accuracy of  $\pm 0.05\% + 2^\circ\text{C}$  for type S thermocouple for an operating range between 0 and  $1800^\circ\text{C}$  and a resolution of  $0.1^\circ\text{C}$ .

The readout from the thermocouple underestimates the actual gas temperature due to the radiation energy loss from the thermocouple to the surroundings. To estimate the radiation correction, a radiation-convection energy balance for the thermocouple bead was performed as follow:

$$Q_c = Q_r \quad (6.13)$$

$$h_c A (T_g - T_p) = \varepsilon \sigma A (T_p^4 - T_w^4) \quad (6.14)$$

where  $h_c$  is the convective heat transfer coefficient, the subscript  $g$  refers to gas,  $p$  refers to the thermocouple probe, and  $w$  refers to the characteristic radiation transfer from the surrounding to the probe surroundings.  $A$  is the probe surface area,  $\sigma$  is the Stefan-Boltzmann's constant ( $5.67 \times 10^{-8} \text{ Wm}^{-2}\text{K}^{-4}$ ), and  $\varepsilon$  is the thermocouple material emissivity. The radiation transfer from the surrounding to the probe has a minor contribution and can be neglected. Then, Equ. 6.14 can be rearranged as follow:

$$T_g = T_p + \frac{\varepsilon \sigma}{h_c} T_p^4 \quad (6.15)$$

The convective heat transfer coefficient,  $h_c$ , for a probe junction assumed to be a spherical surface, can be obtained from a Nusselt number correlation, and is given by:

$$h_c = \frac{k \text{Nu}}{d} \quad (6.16)$$

The Nusselt number (Nu) can be obtained as a function of Reynolds number (Re) and Prandtl number (Pr) for flows over spherically shaped objects (Whitaker 1972), as follows:

$$\text{Nu} = (2 + 0.4 \text{Re}^{0.5} + 0.06 \text{Re}^{2/3}) \text{Pr}^{0.4} \left(\frac{\mu}{\mu_s}\right)^{0.5} \quad (6.17)$$

where the Reynolds number (Re) and Prandtl number (Pr) are given by:

$$\text{Re} = \frac{\rho u d}{\mu}, \quad (6.18)$$

$$\text{Pr} = \frac{c_p \mu}{k}, \quad (6.19)$$

where  $u$ ,  $\rho$ ,  $\mu$ ,  $c_p$ ,  $k$  are the flow velocity, density, viscosity, specific heat, and thermal conductivity of the combustion product at the exit of the stream tube, respectively.  $\mu_s$  is the viscosity of the surrounding fluid. For simplicity, the properties of air are considered in this study.

The thermocouple is mounted on a one-dimensional micrometric arm to allow the movement in the radial direction of the burner while keeping the junction at a constant vertical height of 12 mm. Fig. 6.12 shows the radial temperature profile with a spatial resolution of 0.5 mm of methane-air flame at a distance of 12 mm from the burner, which corresponds to the stream-tubes exit section. The flame has an equivalence ratio of 0.6 and gas flow rate of 3.4 l/s. A constant temperature of  $1600 \pm 20$  K was obtained inside the flame inner zone throughout a radius of 4 mm from the flame axis, followed by a minor temperature gradient to 1580 K at a radius of 7 mm. Then, a sharp reduction in the temperature, which reaches  $1000 \pm 15$  K at a radius of 11 mm, was observed. The temperature obtained from Fig. 6.12 was used for the local burning velocity calculation. The exit of stream-tubes which is considered in this study are located at radii between 3 cm and 7 cm. Accordingly, the temperature variations among all the stream-tubes exit sections is only 20 K.

Due to the high electromagnetic noise, the temperature measurements by a fine wire thermocouple in the presence of plasma discharge were not applicable. Instead, the combustion product temperature ( $T_2$ ) was measured at different inlet mixture temperatures corresponding to those generated by the plasma discharge at the same frequency. Fig. 6.13 shows the influence of the plasma discharge frequency, which represented by the change in the inlet mixture temperature, on

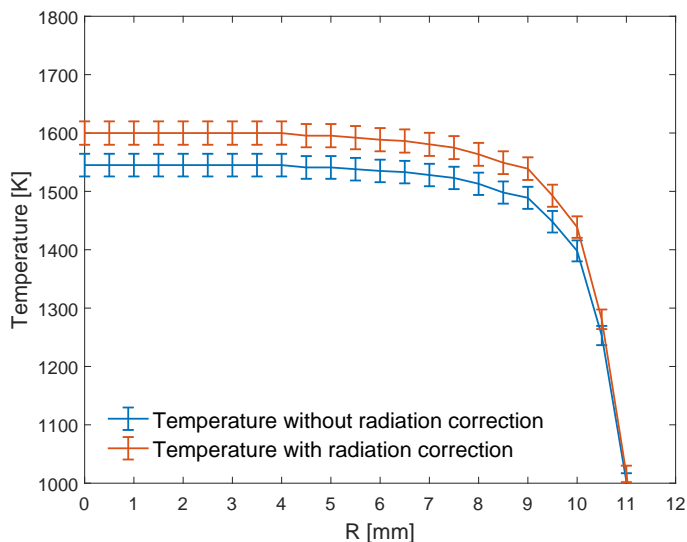


Figure 6.12: Radial temperature profile of methane-air flame at height of 12 mm from the burner with radiation correction (red line), and without radiation correction (blue line). The temperature was measured by a type-S thermocouple with a wire thickness of  $100\ \mu\text{m}$  and a junction diameter of  $200\ \mu\text{m}$ . The flame has an equivalence ratio of 0.6 and gas flow rate of  $3.4\ \text{l/s}$  without plasma discharge.

the combustion product temperature at the burner axis and a height of 12 mm. The figure reveals a small change of the flame temperature, from  $1600 \pm 20\ \text{K}$  to  $1625 \pm 20\ \text{K}$  as a result of increasing the plasma discharge frequency from 0 to 10 kHz. This change in the combustion product temperatures as well as the inlet mixture temperature are taken into account in the local burning velocity calculations.

### 6.6.3 Local burning velocity determination

Figure 6.14 (top) shows the experimental half-width Abel inverted chemiluminescence images for methane-air flames as a function of pulse repetition rate ranging from 0 to 10 kHz at equivalence ratio of 0.6 and atmospheric pressure. It is clear that, the flame height decreases with increasing equivalence ratio as a result of the increase in the burning velocity, as discussed earlier in Chapter 5. Figure 6.14 (bottom) shows the velocity distribution from the PIV measurements and the stream-tubes overlaid on it. Each stream-tube starts from the top of the image with a width of  $0.5\ \text{mm}$ , then it diverges toward the flame front, after that it converges again to reach the reactor channels. The exit plane from the stream tubes (point 2) is located at a height of 12 mm from the burner surface. This height is used for all the conditions considered in this study. Due to the variation in the ve-

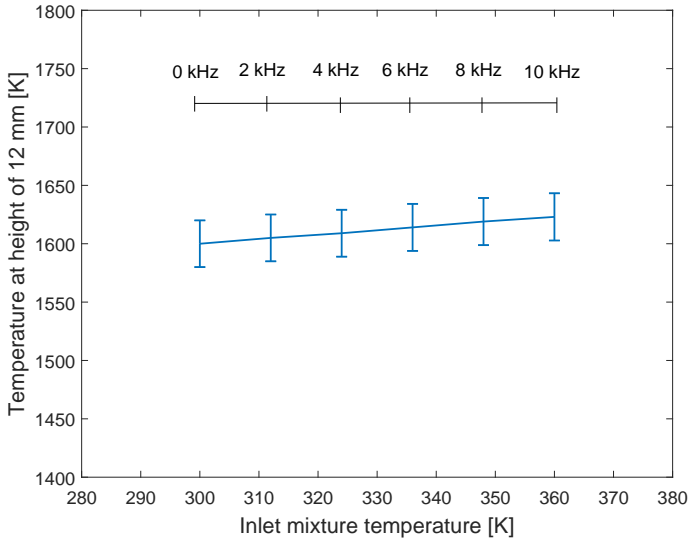


Figure 6.13: Temperature of the methane-air flames at the burner central axis ( $r = 0$  mm) and a height of 12 mm from the burner at different inlet mixture temperatures. The inlet mixture temperatures are corresponding to those produced by the plasma discharge at different plasma frequencies.

locity across the stream-tube exit section, the exit velocity ( $v_2$ ) is considered to be the flow velocity at the center of the stream tube at the exit plane. The upstream temperature, which is also equal to the inlet mixture temperature in the absence of the plasma discharge, is kept constant at 300 K by controlling the water temperature of the hot-water jacket. The inlet mixture temperatures ( $T_o$ ) in the presence of the plasma discharge, were taken from Fig. 4.12.

The local burning velocities at different heights from the reactor for methane-air flames with an equivalence ratio of 0.6 at different pulse repetition rates are presented in Fig.6.15. The figure also presents the simulated burning velocity using CHEM1D at the same gas inlet temperatures corresponding to those produced by the plasma discharge at different pulse repetition rates. In general, the estimated burning velocities by the stream-tube method are slightly lower than the corresponding simulated burning velocities at the same flame and plasma conditions. This can be explained by the fact that the uncertainty of the stream-tube method is a function of the uncertainty of several parameters, like the temperature and velocity determination at the exit plane, area estimation at the flame front and the temperature at exit and inlet. This limits the accuracy of the burning velocity determination by the stream-tube method.

The general trend of the curves shows a nearly constant value of the burning velocity in the locations close to the burner disk. By increasing the vertical

distance from the burner disk, the burning velocity decreases dramatically. This could be due to an increase in heat losses to the surroundings by increasing the distance from the burner disk. It is worth mentioning that, in our analysis, we avoided the locations which are very close to the burner disk for two reasons. The first is to avoid the positive stretch effect which can, significantly, affect the local burning velocity (Gu et al. (2000)), specifically, close to the perimeter of the flame base. The second reason is to avoid the jet effect of the channels which may also have an effect on the local burning velocity.

The figure also shows an increase in the 'global' burning velocity of about 75% by increasing the pulse repetition rate from 0 to 10 kHz. This can be extracted from the difference of the burning velocities for the flat part of the curves, which is 10 cm/s and 17.5 cm/s for 0 kHz and 10 kHz, respectively. It is also clear from the flatness of the curves at the locations close to the burner disk that, even at different plasma conditions, there is no local enhancement of the burning velocity as a result of increasing the plasma discharge, or at least for the distances covered in this study. This proves what we have found previously that the enhancement of the burning velocity is mainly controlled by the thermal mechanism, and there is no evidence for the existence of any radical or electric field effect that improves locally the burning velocity.

The average effective reduced electric field strength  $E/N$  inside the reactor channels is about 500 Td, based on our measurements in Chapter 4. This provides a certain electron energy distribution that is capable of rotational, vibrational, and even ionization excitation of several species. However, for molecular gases and a gas mixture at atmospheric pressure, the electron energy relaxation length is too short due to the short cross section of inelastic collisions, including ionization, electron attachment, electronic excitation, rotational excitation, vibrational excitation, and dissociation processes. The electron energy relaxation length is approximately equal to the effective mean free path for all inelastic processes. Moreover, the de-excitation rates are assumed to be at least three orders of magnitude larger than the excitation rates at the given conditions (Altendorfner et al. 2011). Also, take into account that the minimum distance between the flame front and the microplasma channels, at the flame base, is about 1 mm. This is significantly larger than the effective lifetime of the ions, vibrationally and rotationally excited species. This provides an explanation for the absence of the chemical effect of the plasma discharge on the local burning velocity.

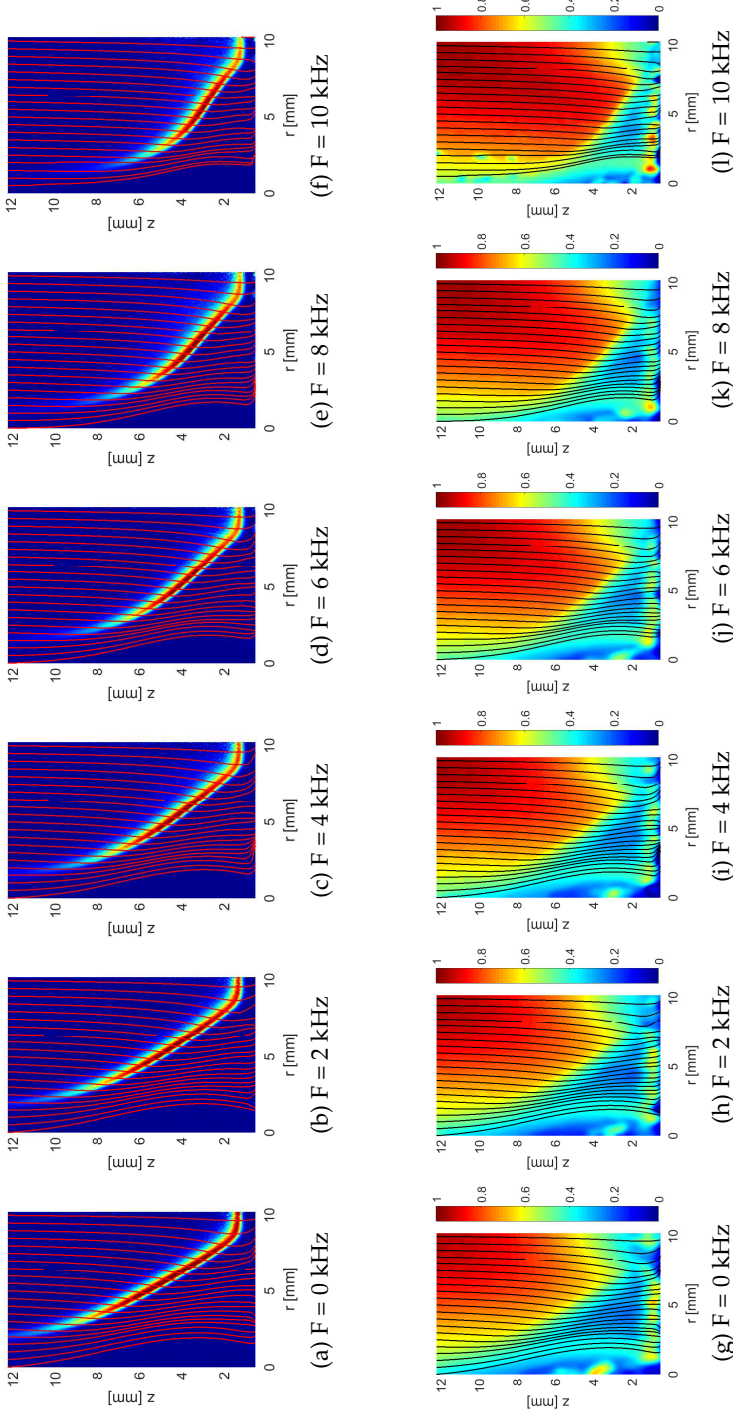


Figure 6.14: (Top) the half-width Abel inverted chemiluminescence images for methane-air flames at different pulse repetition rates ranging from 0 to 10 kHz. (Bottom) velocity contours from PIV measurements for the same flames and plasma conditions. The streamlines of the flow are overlaid in all the images. All the images are for an equivalence ratio of  $\phi = 0.6$  and mixture flow rate of 3.4 l/min at atmospheric pressure.

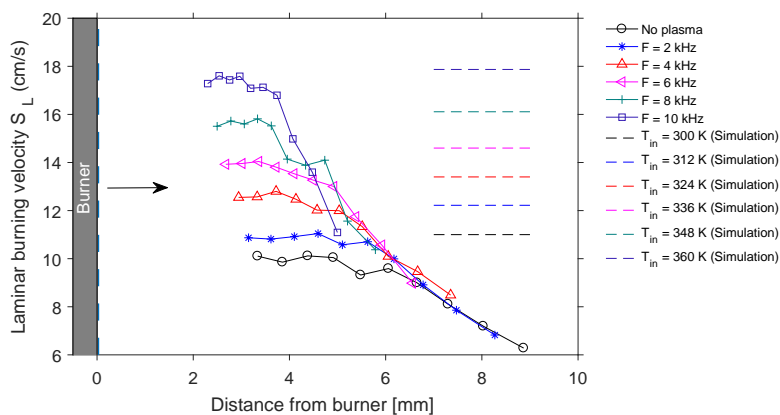


Figure 6.15: The local burning velocities of the methane-air flames at different vertical locations from the burner disk and at different pulse repetition rates. The dashed lines are for the simulated burning velocities using CHEM1D at equivalence ratio of 0.6 and gas inlet temperatures corresponding to those produced by the plasma discharge at different pulse repetition rates. All for an equivalence ratio of 0.6 and mixture flow rate of 3.4 l/min at atmospheric pressure.

## 6.7 Summary and Conclusions

The local effect of the plasma discharge on the burning velocity of lean methane-air flame is examined by the stream-tube method. In this experiment we used the same inverted flame that has been investigated in Chapter 5. PIV setup is used to determine the velocity distribution and to define the stream lines of the flow. The effect of using different seeding densities has been examined electrically and optically. A very minor (negligible) effect has been found in the tested seeding densities range. A set of visualization images has been used for cold flow as well as the flame to define the different flow regimes downstream of the reactor. The cold flow visualization images show a recirculation zone above the center of the burner disk, where the smaller channels are present. This recirculation zone is absent in case of a flame due to the high flow acceleration as a result of the elevated temperature at the flame base.

With the help of the velocity measurement, Abel inverted flame images and temperature measurements, the local burning velocities have been determined at different vertical locations from the plasma discharge. The stream-tube method shows a good agreement with the flame-area method with slightly lower values due to the measurement uncertainties. We have found that the burning velocity of the lean methane-air flame is independent of the distance to the plasma source to a certain distance, even at different plasma frequencies. This proves that, for the



studied distances, there is no local effect of the plasma discharge on the burning velocity. This means that the dominating mechanism is the thermal mechanism and there is no evidence of any local improvement due to chemical or aerodynamic mechanisms.

Although it has not been verified by experiment, nevertheless, the effect of the plasma discharge on the local burning velocity at low pressure, specially below 100 mbar, is expected to be more significant. This is due to the considerable increase in the mean free path and increase in the reduced electric field strength and, consequently, the higher electron energy and the larger amount of the active species and radicals, as discussed earlier in Section 4.6.

## Summary, conclusions and recommendations

---

---

### 7.1 Overview

The main objective of this thesis was to study the effect of nanosecond plasma discharge on premixed combustion stability and emissions. A nanosecond DBD microplasma reactor was developed, and different electrical and optical diagnostic techniques were employed to study the plasma discharge and combustion characteristics. To summarize the study, two main topics, based on the research objectives, are discussed. Firstly, the main thermal and electrical characteristics of the developed DBD microplasma reactor at different operating conditions were evaluated. Secondly, the effect of the generated plasma discharge on the flame stability and emissions of premixed flames was studied. Moreover, the main conclusions and suggestion for future research are provided in this chapter.

### 7.2 Summary and conclusion

To improve our understanding of the plasma discharge in DBD microplasma reactors and the effect of the generated plasma on combustion performance, we developed facilities to optically and electrically examine the plasma discharge at different pressures, flow velocities and gas compositions. From these experiments we have been able to summarize and draw some conclusions, as follow:

#### Plasma discharge characteristics

- We succeeded to generate a uniform plasma discharge in a plate with multiple micro-channels, at atmospheric pressure and below, using a nanosecond

high-voltage pulses in a dielectric barrier discharge configuration.

- We learned that the dielectric constant and the thickness of the dielectric material are the most crucial factors for the plasma characteristics as well as the reactor lifetime.
- We found that the discharge at low operating pressures is characterized by high vibrational temperatures (4000 K) and high effective reduced electric field strength (10000 Td) compared to the discharge at atmospheric pressure (3460 K and 550 Td, respectively).
- The plasma discharge in the DBD microplasma reactor is in a non-equilibrium state, where the vibrational, rotational and translational temperatures are highly unequal, in the pressure range between 50 mbar and 1 bar.
- The reduced electric field strength and the emission intensity distribution inside the micro-channels are investigated using optical emission spectroscopy, and they show a high dependence on the operating pressure and the pulse polarity.
- There is a minor effect of the flow velocity inside the channels on the plasma discharge intensity, except for a stagnant gas, which has a maximum intensity. We interpreted this by the high pre-ionization level in the case of a stagnant gas.
- For a pulse repetition rate of 400 Hz and below, the reactor works in a capacitive mode, and no plasma discharge is noticed. Above 400 Hz, a discharge breakdown occurs in some channels, which increases gradually until it reaches full-breakdown at 1.8 kHz, and the pulse energy increases accordingly.
- Discharge intensity and full-breakdown frequency are also influenced by the composition of the gas passing through the channels. The increase in the equivalence ratio results in a reduction in the plasma intensity as well as an increase in the full-breakdown frequency. Based on a numerical study, we also have found that the electron energy decreases by increasing the equivalence ratio.

### **Influence of combustion stability and emissions**

- A complete burner facility was developed in order to perform experiments utilizing the DBD microplasma reactor as the burner plate. The experiments used different burning velocity determination techniques to study the effect of the plasma discharge on the global and local burning velocities of the premixed flame.
- An increase of the burning velocity of about 100% in very lean ( $\phi = 0.55$ ) flames as a result of the plasma discharge effect was achieved.

- We learned that the increase in the burning velocity depends on a number of factors, namely, equivalence ratio, pulse repetition rate, and plasma to flame power ratio.
- A comparison between the experimental and numerical results reveals that about 90% of the burning velocity enhancement is due to the increase in the mixture temperature as a result of the plasma discharge for the current configuration.
- The effect of the plasma discharge on the '*local*' burning velocity was also evaluated using the stream-tube method. This method used the flow streams downward the reactor, created by the PIV analysis, to calculate the local burning velocity at different heights from the plasma source.
- We found a negligible effect of the seeding density on the plasma intensity. We explained that by the short residence time of the seeding particles in the plasma discharge.
- It is shown that, at atmospheric pressure, the burning velocity change is independent of the distance to the plasma source for all the pulse repetition rates covered in this study.
- Based on the above discussion, it can be concluded that the nanosecond DBD plasma discharge is a fast and energy efficient way to globally enhance the stability of the premixed flames through the thermal mechanism. Moreover, there is no evidence of exciting any local enhancement due to chemical contribution at atmospheric pressure.
- Although plasma assisted combustion has many merits, it has also environmental impact. We proved that using plasma discharge to enhance combustion stability comes with the cost of producing an elevated amount of NO<sub>x</sub>. Therefore, more research is needed to mitigate this impact .

### 7.3 Recommendation for future work

Based on the work presented in this thesis, there are several topics where detailed experiments and numerical modeling can significantly improve our understanding about how plasma enhances combustion.

- Using different dielectric material for the DBD microplasma reactor to increase the lifetime.
- Studying the effect of using different power sources (RF, AC or DC) on the generated species. The aim of this study is to reach a high electron energy, where the electrons are capable of breaking the fuel molecules bonds in one single collision.

- More investigations on the role of chemical mechanism of the plasma generated species are required at different pressure ranges. More specifically, the role of electronically excited oxygen ( $O_2(a^1\Delta_g)$  and  $O_2(b^1\Sigma_g^+)$ ) and OH radicals. Laser induced fluorescence LIF could give a quantitative evaluation for the production of these species in the discharge region.
- Numerical simulation model of plasma discharge inside the DBD reactor channel is required, considering all air-fuel chemical and electron-impact reactions. This will provide information about the generated radicals and species which may contribute to the combustion enhancement and their lifetime.
- The full kinetic mechanism of plasma-assisted ignition and combustion of hydrocarbons is very large and complex. Using detailed kinetic models is beyond our current computational capabilities. Therefore, it is important to develop a robust reduction mechanism methods to reduce and simplify the detailed kinetic models so that it can be used in numerical simulations.

# A

## APPENDIX

### Unsuccessful reactor geometries

---

---

In this appendix, different attempts to generate a uniform glow discharge using different reactor geometries are presented. The main purpose of this appendix is to report the unsuccessful geometries, aiming to save time and cost for who wants to continue developing of the DBD microplasma reactor. The unsuccessful attempts are not only related to the geometry problems, But also, can be related the power supply characteristics (voltage, current, pulse duration and rise-time), materials and the operating condition, like pressure, temperature, working gas, etc. However, we will focus in this appendix only on the geometry attempts.

#### A.1 Surface electrodes reactor

This geometry was one of the first attempts to generate a plasma discharge inside a micro channels. The geometry consists of two surface electrodes separated by a dielectric material. As shown in the A.1, the entire structure is drilled by 380 channels of 0.4 mm in diameter and 0.8 mm pitch. The dielectric thickness is 0.5 mm and the electrodes thickness is 38  $\mu$ . The electrodes are made of copper and the dielectric material is a composite of woven electrical grade fiberglass and epoxy resin with a dielectric constant of  $D_r$  of  $4.17 \pm 0.05$  (at 1 GHz / 23 °C).

The results of this geometry are presented in the Fig.A.2 for a voltage of (a) 2 kV, and (b) 4 kV. In this structure, only arc discharge can be developed at atmospheric pressure. This is due to the relation between the diameter of the channels and the operating pressure. As mentioned earlier in Chapter 2, the maximum channel diameter that can develop glow discharges in such configurations should follow the Allis-White similarity law, in which the product of the pressure ( $p$ ) and the channel diameter ( $D$ ) should fall in the typical operating range for MHCD, which is 0.1-13 mbar·cm. To meet this condition, the channel diameter should be less than 100  $\mu$ m for atmospheric pressure applications, which is not easy to manufacture for such geometry.

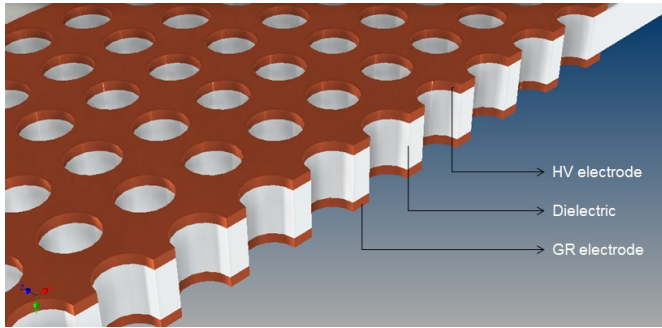


Figure A.1: The surface electrodes approach.

We can also notice from the images that the discharge is located in only few channels, while there is no discharge in the most of the channels. This is due to the limited power provided by the pulsed plasma generator. This number increases by increasing the applied voltage from 2 kV to 4 kV.

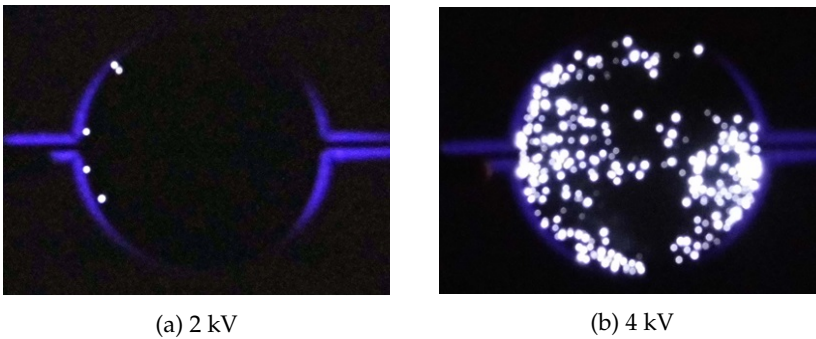


Figure A.2: Images showing the surface electrodes reactor at a pulse repetition rate of 3 kHz and pulse width of 50 ns at atmospheric pressure. The applied voltages are (a) 2 kV, and (b) at 4 kV.

## A.2 Wire electrodes reactor

This geometry consists of a dielectric slab and two wire electrodes located on the same plan. As shown in Fig. A.3, the two wires have a thickness of  $38 \mu$  and a width of 2 mm. The wire terminals are connected to the high-voltage axial cable from opposite sides. The aim of this design was to generate the plasma discharge as close as possible to the flame front. Similar to the first approach, after applying the high-voltage between the electrodes, there was no uniform discharge on the surface, but just sparks in some spots only.

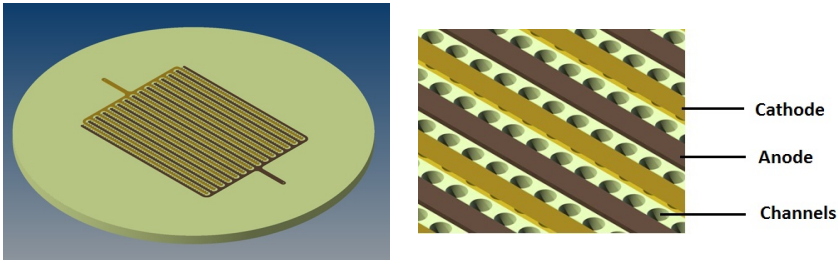


Figure A.3: Schematic for the wire electrodes geometry.

### A.3 Insulated thick metal reactor

This geometry consists of a 1.5 mm thickness aluminum electrode as a base plate, a 100  $\mu\text{m}$  thickness dielectric layer and a 38  $\mu\text{m}$  thickness copper foil, as shown in Fig. A.4. The dielectric material is POLYTHERM, which is made by a special dielectric polymer that allows to glue the copper layer to the aluminum base plate. This material has a dielectric constant of 5.5 and a thermal conductivity of 1.3 W/m.K. Thanks to the thin dielectric layer, this geometry allows maximum heat dissipation through the reactor base. This heat can be generated from the plasma discharge as well as the heat transferred from the flame.

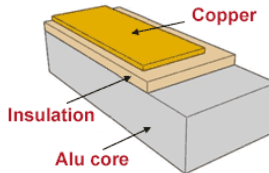


Figure A.4: Schematic for the insulated thick metal reactor .

Although, this design is very promising in plasma-assisted combustion applications due to its heat dissipation capability, but the minimum applied voltage of the plasma generator is higher than the arcing voltage. This is due to the small thickness of the dielectric layer. This problem can be avoided by using different plasma power source or different dielectric material or thickness.





**B****APPENDIX**

## Testing protocol for the NPG-6/15k pulse generator

---

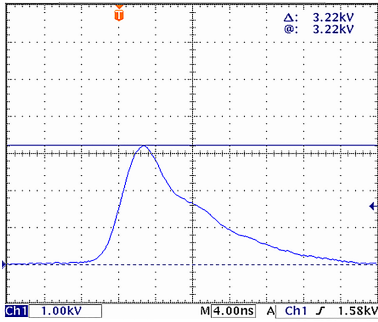
---

The NPG-6/15k high-voltage pulse generator has been qualified at the supplier using a 75 Ohm and 20 W non-inductive resistor connected at the terminal of a 3 m coaxial cable. The voltage is measured by a Tektronix P6015A high-voltage probe and monitored by a Tektronix TDS3052C oscilloscope with an analog bandwidth of 500 MHz and sampling rate of 5 GS/s. Tektronix P6015A high-voltage probe has a sensitivity of 1V/1kV, a maximum voltage of 20 kV and a rise-time of 4 ns.

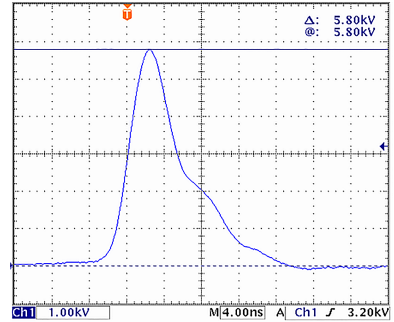
Figures B.1a and B.1b show the minimum and maximum pulse voltage amplitudes and the signal rise-time at a matched load of 75 Ohm. The measurements show values of 3.22 kV and 5.8 kV for the minimum and maximum voltage, respectively. While, the measured values are 6.44 kV and 11.6 kV for an open cable, as shown in Figs. B.2a and B.2b. The measurement of the output pulse front duration shows a pulse rise-time of 2.96 ns, measured between 5% to 95% levels, as shown in Figs. B.3. The maximum measured frequency is 15 kHz.

Table B.1: Summary of the nominal values vs the measured values for the NPG-6/15k pulse generator.

Technical parameter	Nominal value		Measured value	
	min	max	min	max
Output pulse polarity	Positive		Positive	
Output pulse amplitude at 75 Ohm matched load, see Fig.B.1a and B.1b	4kV	6kV	3.22kV	5.8kV
Output pulse amplitude at open cable, see Figs.B.2a and B.2b		12kV	6.44kV	11.6kV
Output pulse rise time (at 0.1-0.9 levels), see Fig.B.3		4 ns		2.96 ns
Output pulse repetition rate	100 Hz	15 kHz	1.5 Hz	15.95 kHz

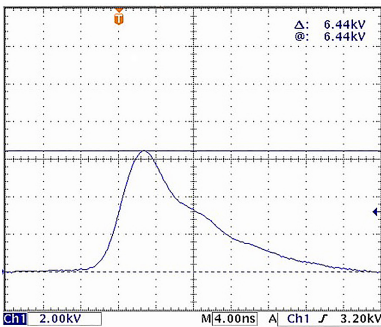


(a) Minimum amplitude.

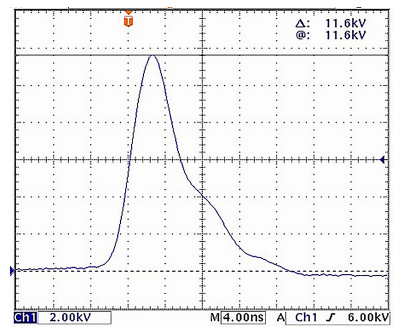


(b) Maximum amplitude.

Figure B.1: Output pulse waveform at matched load of 75 Ohm. Amplitude knob is in (a) 'min' position and (b) 'max' position, frequency knob is in "min" position.



(a) Minimum amplitude.



(b) Maximum amplitude.

Figure B.2: Output pulse waveform at open end of the cable. Amplitude knob is in (a) 'min' position, and (b) 'max' position, frequency knob is in "min" position.

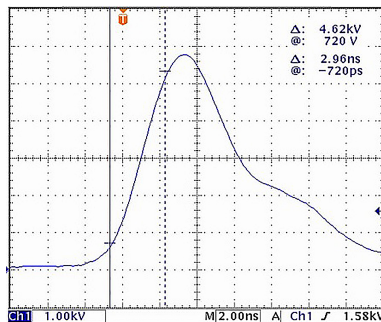


Figure B.3: Measurement of output pulse front duration.

# C

## APPENDIX

### Faraday cage

---

The electromagnetic field generated by the nanosecond high-voltage pulses is considered as one of the most significant problem that can affect or damage the instruments which are used in/around the setup. To reduce or eliminate this field, a Faraday cage has been built around the setup to cancel the field outside the cage. In this Appendix, we will present the main design principles of the Faraday cage and the measurement before and after using it.

#### C.1 The electromagnetic field measurements

The electromagnetic field was measured before using the Faraday cage. Figure C.1 shows a schematic digram for the Experimental setup before using the Faraday cage and the location where we measured the electromagnetic field. The electromagnetic field was measured by a PCE-EM 30 field meter. The meter is fitted with EP-04L probe to measure in a frequency range between 100 kHz to 100 MHz, and EP-03H probe for a frequency range between 100 MHz to 3 GHz. The meter has an accuracy of  $\pm 2$  dB.

Table C.1 shows the electromagnetic field EMF values at different frequencies for all the measuring locations around the setup. We can see that the EMF at the pulse generator (point A) and the reactor (point B), for frequencies from 100 kHz to 100 MHz, show a very high values. While, the system generates a very low EMF at frequencies above 100 MHz. The table shows also a slightly high value of EMF, reaches to 40 V/m, at the camera system (point H) and the oscilloscope (point G).

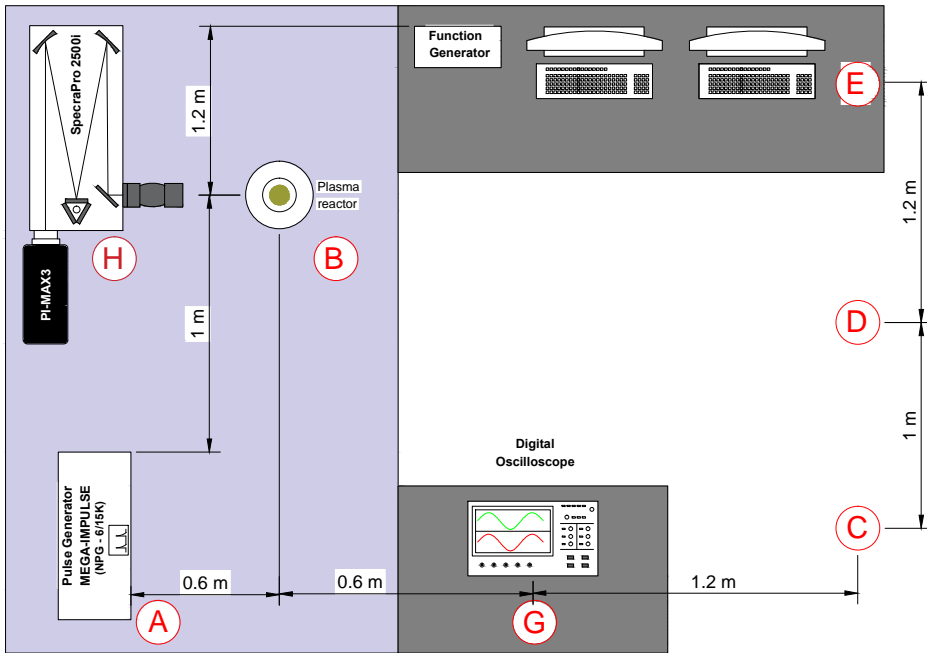


Figure C.1: Schematic of the experimental setup before using the Faraday cage. The schematic shows the location of the measuring points.

Table C.1: The measured electromagnetic field EMF for different frequencies at different locations. For the measuring locations refer to Fig.C.1.

Frequency	EMF [V/m]							
	Location							
	A	B	C	D	E	F	G	H
100 kHz	190	175	1	0.5	1	1	6	40
200 kHz	35	>220	1	1	1	1	30	27
500 kHz	>220	193	1	0.5	1	1	30	10
1 MHz	>220	>220	1	1	0.5	0.5	10	15
10 MHz	35	90	2.5	1.5	2	2	6.5	12
13.56 MHz	45	100	1.5	0.5	0.5	0.5	0.5	16
100 MHz	13	18	1.4	0.7	1.3	0.7	0.7	26
900 MHz	0.6	2.3	0.2	0.3	0.3	0.2	0.2	1.2
1.86 GHz	0.5	1.8	0.2	0.1	0.3	0.1	0.2	0.8

## C.2 Faraday cage design

The Faraday cage is constructed from perforated aluminum sheets with a thickness of 3 mm. The perforation has a diagonal pattern with hole diameter of 1 cm and pass-through ratio of 40%. Figure C.2 shows a schematic drawing for the Faraday cage. As shown, it has a width of 55 cm, length of 1.2 m, and height of 80. Each of the front and back sides has a movable window and a fixed window. The fixed window is used to pass-through all the electric, gas, and water connections. A 150 mm exhaust line is installed directly above the Faraday cage, and is connected to the general exhaust system of the lab. The entire cage is connected to the general ground connection of the building.

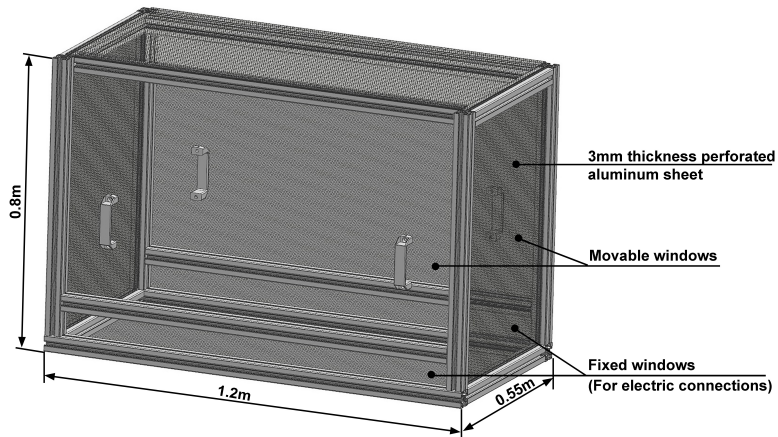


Figure C.2: Schematic drawing for the Faraday cage.

### C.2.1 Skin depth

The fields can be divided into two forms: magnetic and electric. The electric fields can be easily eliminated by a thin high conductive metal foil. However, magnetic fields are much more difficult to stop. They need to generate eddy currents inside the shield material to create magnetic fields that oppose the impinging field. The required depth of current penetration for a given shielding effectiveness (SE) depends on the frequency of the field, and on the characteristics of the metal used for the shield, and is known as the 'skin effect'. Figure C.3 shows the skin depth as a function of the frequency for different materials at room temperature. Based on our measurements in Table A.3, the range of the frequencies that is needed to be avoided is in the range between 10 kHz and 100 MHz, which is corresponding to a skin depth of about 1 mm for aluminum, (Beaty and Fink 2007) . A value of 3 mm is chosen for the Faraday cage skin depth as a factor of safety.

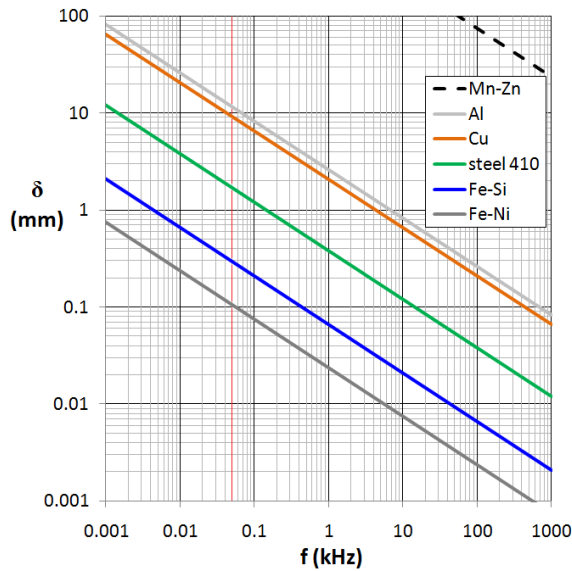


Figure C.3: Required skin depth as a function of the frequency of the field for different materials at room temperature, Beaty and Fink (2007).

## C.2.2 Minimum hole sizes

The holes in the Faraday cage should be sufficiently smaller than the wavelength of field. The frequency is related to the wavelength by the following equation:

$$f = \frac{c}{\gamma} \quad (\text{C.1})$$

where  $f$  is the frequency in Hz,  $c$  is the speed of light in m/s, and  $\gamma$  represents the wavelength in meters. In our case, the highest frequency required to be avoided is 1.86 GHz. This is corresponding to a wavelength of 16 mm. In our design, we considered a maximum holes size of 10 mm as a factor of safety.

## C.2.3 The EMF after using the Faraday cage

We performed the EMF measurements after using the Faraday cage. The results show that the measured EMF's do not exceed 1 V/m at all the locations and for all frequencies, as shown in Table C.2.

Table C.2: The EMF after using the Faraday cage for a plasma frequency of 5 kHz. For the measurement locations A, B and C refer to Fig. C.1.

Frequency	EMF [V/m]		
	Location		
	A	B	C
100 kHz	0.5	0.5	0.5
500 kHz	0.1	0.1	0.1
1 MHz	0.3	0.3	0.2
10 MHz	1	0.2	0.2





## D

## APPENDIX

## Electron-impact reactions with molecules and radicals for methane-air mixture

Table D.1: Electron impact excitation rate coefficients for CH<sub>4</sub>.

No.	Reaction	Type	$k_r$	Ref.
R1	E + CH <sub>4</sub> → CH <sub>3</sub> + H-	Attachment	BOLSIG+	Morgan (1992)
R2	E + CH <sub>4</sub> → H <sub>2</sub> + CH <sub>2</sub> -	Attachment	BOLSIG+	Morgan (1992)
R3	E + CH <sub>4</sub> → E + CH <sub>4</sub>	Elastic	BOLSIG+	Morgan (1992)
R4	E + CH <sub>4</sub> → E + CH <sub>4</sub> (0.162eV)	Vibrational	BOLSIG+	Morgan (1992)
R5	E + CH <sub>4</sub> → E + CH <sub>4</sub> (0.361eV)	Vibrational	BOLSIG+	Morgan (1992)
R6	E + CH <sub>4</sub> → E + CH <sub>4</sub> * (10eV)	Dissociation	BOLSIG+	Morgan (1992)
R7	E + CH <sub>4</sub> → E + CH <sub>4</sub> * (11eV)	Dissociation	BOLSIG+	Morgan (1992)
R8	E + CH <sub>4</sub> → E + CH <sub>4</sub> * (12eV)	Dissociation	BOLSIG+	Morgan (1992)
R9	E + CH <sub>4</sub> → E + CH <sub>4</sub> * (19eV)	Dissociation	BOLSIG+	Morgan (1992)
R10	E + CH <sub>4</sub> → E + E + CH <sub>4</sub> <sup>+</sup>	Ionization	BOLSIG+	Morgan (1992)
R11	E + CH <sub>4</sub> → E + E + H + CH <sub>3</sub> <sup>+</sup>	Ionization	BOLSIG+	Morgan (1992)

Table D.2: Electron impact excitation rate coefficients for N<sub>2</sub>.

No.	Reaction	Type	$k_r$	Ref.
R12	E + N <sub>2</sub> → E + N <sub>2</sub>	Effective	BOLSIG+	Phelps and Pitchford (1985)
R13	E + N <sub>2</sub> → E + N <sub>2</sub> * (0.02eV)	Rotational	BOLSIG+	Phelps and Pitchford (1985)
R14	E + N <sub>2</sub> → E + N <sub>2</sub> (V1) (0.29eV)	Vibrational	BOLSIG+	Phelps and Pitchford (1985)
R15	E + N <sub>2</sub> → E + N <sub>2</sub> (V1) (0.29eV)	Vibrational	BOLSIG+	Phelps and Pitchford (1985)
R16	E + N <sub>2</sub> → E + N <sub>2</sub> (V1) (0.291eV)	Vibrational	BOLSIG+	Phelps and Pitchford (1985)
R17	E + N <sub>2</sub> → E + N <sub>2</sub> (V2) (0.59eV)	Vibrational	BOLSIG+	Phelps and Pitchford (1985)
R18	E + N <sub>2</sub> → E + N <sub>2</sub> (V3) (0.88eV)	Vibrational	BOLSIG+	Phelps and Pitchford (1985)
R19	E + N <sub>2</sub> → E + N <sub>2</sub> (V4) (1.17eV)	Vibrational	BOLSIG+	Phelps and Pitchford (1985)

*Continued on next page*

Table D.2 – Continued from previous page

No.	Reaction	Type	$k_r$	Ref.
R20	E + N2 ->E + N2(V5)(1.47eV)	Vibrational	BOLSIG+	Phelps and Pitchford (1985)
R21	E + N2 ->E + N2(V6)(1.76eV)	Vibrational	BOLSIG+	Phelps and Pitchford (1985)
R22	E + N2 ->E + N2*(11.03eV)	Excitation	BOLSIG+	Phelps and Pitchford (1985)
R23	E + N2 ->E + N2*(11.88eV)	Excitation	BOLSIG+	Phelps and Pitchford (1985)
R24	E + N2 ->E + N2*(12.25eV)	Excitation	BOLSIG+	Phelps and Pitchford (1985)
R25	E + N2 ->E + N + N(13eV)	Excitation	BOLSIG+	Phelps and Pitchford (1985)
R26	E + N2 ->E + N2(V7)(2.06eV)	Vibrational	BOLSIG+	Phelps and Pitchford (1985)
R27	E + N2 ->E + N2(V8)(2.35eV)	Vibrational	BOLSIG+	Phelps and Pitchford (1985)
R28	E + N2 ->E + N2*(6.17eV)	Excitation	BOLSIG+	Phelps and Pitchford (1985)
R29	E + N2 ->E + N2*(7eV)	Excitation	BOLSIG+	Phelps and Pitchford (1985)
R30	E + N2 ->E + N2*(7.35eV)	Excitation	BOLSIG+	Phelps and Pitchford (1985)
R31	E + N2 ->E + N2*(7.36eV)	Excitation	BOLSIG+	Phelps and Pitchford (1985)
R32	E + N2 ->E + N2*(7.8eV)	Excitation	BOLSIG+	Phelps and Pitchford (1985)
R33	E + N2 ->E + N2*(8.16eV)	Excitation	BOLSIG+	Phelps and Pitchford (1985)
R34	E + N2 ->E + N2*(8.4eV)	Excitation	BOLSIG+	Phelps and Pitchford (1985)
R35	E + N2 ->E + N2*(8.55eV)	Excitation	BOLSIG+	Phelps and Pitchford (1985)
R36	E + N2 ->E + N2*(8.89eV)	Excitation	BOLSIG+	Phelps and Pitchford (1985)
R37	E + N2 ->E + E + N2+	Ionization	BOLSIG+	Phelps and Pitchford (1985)

Table D.3: Electron impact excitation rate coefficients for O<sub>2</sub>..

No.	Reaction	Type	$k_r$	Ref.
R38	E + O2 ->O2-	Attachment	BOLSIG+	Lawton and Phelps (1978)
R39	E + O2 ->O2-	Attachment	BOLSIG+	Lawton and Phelps (1978)
R40	E + O2 ->E + O2	Effective	BOLSIG+	Lawton and Phelps (1978)
R41	E + O2 ->E + O2(0.02eV)	Rotational	BOLSIG+	Lawton and Phelps (1978)
R42	E + O2 ->E + O2(V)(0.19 eV)	Rotational	BOLSIG+	Lawton and Phelps (1978)
R43	E + O2 ->E + O2(V)(0.38eV)	Rotational	BOLSIG+	Lawton and Phelps (1978)
R44	E + O2 ->E + O2(V)(0.38eV)	Vibrational	BOLSIG+	Lawton and Phelps (1978)
R45	E + O2 ->E + O2(V)(0.57eV)	Vibrational	BOLSIG+	Lawton and Phelps (1978)
R46	E + O2 ->E + O2(V)(0.75eV)	Vibrational	BOLSIG+	Lawton and Phelps (1978)
R47	E + O2 ->E + O2*(0.977eV)	Excitation	BOLSIG+	Lawton and Phelps (1978)
R48	E + O2 ->E + O2*(1.627ev)	Excitation	BOLSIG+	Lawton and Phelps (1978)
R49	E + O2 ->E + O2*(14.7eV)	Dissociative	BOLSIG+	Lawton and Phelps (1978)
R50	E + O2 ->E + O2*(4.5eV)	Excitation	BOLSIG+	Lawton and Phelps (1978)
R51	E + O2 ->E + O2*(6eV)	Excitation	BOLSIG+	Lawton and Phelps (1978)
R52	E + O2 ->E + O2*(8.4eV)	Excitation	BOLSIG+	Lawton and Phelps (1978)
R53	E + O2 ->E + O2*(9.97eV)	Excitation	BOLSIG+	Lawton and Phelps (1978)
R54	E + O2 ->E + E + O2+	Ionization	BOLSIG+	Lawton and Phelps (1978)

# Bibliography

- Akitsu, Tetsuya, Hiroshi Ohkawa, Masao Tsuji, Hideo Kimura and Masuhiro Kogoma (2005). Plasma sterilization using glow discharge at atmospheric pressure. *Surface and Coatings Technology* **193**(1), 29–34.
- Altendorfer, Florian, Johannes Kuhl, Lars Zigan and Alfred Leipertz (2011). Study of the influence of electric fields on flames using planar LIF and PIV techniques. *Proceedings of the Combustion Institute* **33**(2), 3195 – 3201.
- Andrews, Thomas and Peter G. Tait (1860). VII. on the volumetric relations of ozone, and the action of the electrical discharge on oxygen and other gases. *Philosophical Transactions of the Royal Society of London* **150**, 113–131.
- Bak, Moon Soo, Wookyung Kim and Mark A. Cappelli (2011). On the quenching of excited electronic states of molecular nitrogen in nanosecond pulsed discharges in atmospheric pressure air. *Applied Physics Letters* **98**(1), 011502.
- Beatty, H. Wayne and Donald G. Fink (2007). *Standard handbook for electrical engineers*. McGraw-Hill New York.
- Becker, K.H., K.H. Schoenbach and J.G. Eden (2006). Microplasmas and applications. *Journal of Physics D: Applied Physics* **39**(3), R55.
- Belhi, Memdouh, Pascale Domingo and Pierre Vervisch (2010). Direct numerical simulation of the effect of an electric field on flame stability. *Combustion and Flame* **157**(12), 2286 – 2297.
- Benedikt, J., V. Raballand, A. Yanguas-Gil, K. Focke and A. von Keudell (2007). Thin film deposition by means of atmospheric pressure microplasma jet. *Plasma Physics and Controlled Fusion* **49**(12B), B419.
- Bonazza, Thomas J., Kurt L. VanVoorhies and James E. Smith (1992). RF plasma ignition system concept for lean burn internal combustion engines. In *SAE Technical Paper*. SAE International.
- Bosschaart, Karel (2002). *Analysis of the heat flux method for measuring burning velocities*. Technische Universiteit Eindhoven Eindhoven, The Netherlands.

- Bosschaart, K.J. and L.P.H. De Goeij (2003). Detailed analysis of the heat flux method for measuring burning velocities. *Combustion and flame* **132**(1-2), 170–180.
- Bosschaart, K.J. and L.P.H. De Goeij (2004). The laminar burning velocity of flames propagating in mixtures of hydrocarbons and air measured with the heat flux method. *Combustion and Flame* **136**(3), 261–269.
- Brande, William Thomas (1814). IV. The bakerian lecture: on some new electro-chemical phenomena. *Philosophical Transactions of the Royal Society of London* **104**, 51–61.
- Bruggeman, P.J., N. Sadeghi, D.C. Schram and V. Linss (2014). Gas temperature determination from rotational lines in non-equilibrium plasmas: a review. *Plasma Sources Science and Technology* **23**(2), 023001.
- Cathey, C.D., T. Tang, T. Shiraishi, T. Urushihara, A. Kuthi and M.A. Gundersen (2007). Nanosecond plasma ignition for improved performance of an internal combustion engine. *IEEE Transactions on Plasma Science* **35**(6), 1664–1668.
- Chen, Hsin Liang, How Ming Lee, Shiao Huei Chen and Moo Been Chang (2008a). Review of packed-bed plasma reactor for ozone generation and air pollution control. *Industrial & Engineering Chemistry Research* **47**(7), 2122–2130.
- Chen, Hsin Liang, How Ming Lee, Shiao Huei Chen and Moo Been Chang (2008b). Review of packed-bed plasma reactor for ozone generation and air pollution control. *Industrial & Engineering Chemistry Research* **47**(7), 2122–2130.
- Chen, Zheng and Yiguang Ju (2008). Combined effects of curvature, radiation, and stretch on the extinction of premixed tubular flames. *International Journal of Heat and Mass Transfer* **51**(25-26), 6118–6125.
- Choi, Yoon-Ho, Ji-Hun Kim, Kwang-Hyun Paek, Won-Tae Ju and YS Hwang (2005). Characteristics of atmospheric pressure N<sub>2</sub> cold plasma torch using 60-Hz AC power and its application to polymer surface modification. *Surface and Coatings Technology* **193**(1), 319–324.
- Conrads, H. and M. Schmidt (2000). Plasma generation and plasma sources. *Plasma Sources Science and Technology* **9**(4), 441.
- Correale, G., T. Michelis, D. Ragni, M. Kotsonis and F. Scarano (2014). Nanosecond-pulsed plasma actuation in quiescent air and laminar boundary layer. *Journal of Physics D: Applied Physics* **47**(10), 105201.
- Correale, Giuseppe, Ilia Popov, Aleksandr Rakitin, Andrei Starikovskii, Steven Hulshoff and Leo Veldhuis (2011). Flow separation control on airfoil with pulsed nanosecond discharge actuator. In *49th AIAA Aerospace Sciences Meeting including the New Horizons Forum and Aerospace Exposition*, pp. 1079.

- de Goey, L.P.H., A. van Maaren and R.M. Quax (1993). Stabilization of adiabatic premixed laminar flames on a flat flame burner. *Combustion Science and Technology* **92**(1-3), 201–207.
- Edmondson, H. and M.P. Heap (1970). Blowoff of inverted flames. *Combustion and Flame* **14**(2), 191–194.
- Egolfopoulos, F.N., P. Cho and C.K. Law (1989). Laminar flame speeds of methane-air mixtures under reduced and elevated pressures. *Combustion and Flame* **76**(3), 375 – 391.
- Eroglu, A., A. Tataroglu and S. Altindal (2012). On the temperature dependent dielectric properties, conductivity and resistivity of MIS structures at 1MHz. *Microelectronic Engineering* **91**, 154 – 158.
- Felix, Valentin, Philippe Lefaucheu, Olivier Aubry, Judith Golda, Volker Schulz von der Gathen, Lawrence J Overzet and Remi Dussart (2016). Origin of microplasma instabilities during DC operation of silicon based microhollow cathode devices. *Plasma Sources Science and Technology* **25**(2), 025021.
- Foest, R., M. Schmidt and K. Becker (2006). Microplasmas, an emerging field of low-temperature plasma science and technology. *International Journal of Mass Spectrometry* **248**(3), 87 – 102.
- Fridman, Alexander (2008). *Plasma chemistry*. Cambridge university press.
- Fuss, Sabine, Josep Canadell, Glen Peters, Massimo Tavoni, Robbie Andrew, Philippe Ciais, Robert Jackson, Chris Jones, Florian Kraxner, Nebosja Nakicenovic et al. (2014). Betting on negative emissions. *Nature Climate Change* **4**(10), 850.
- GmbH, PIVTEC. Pivview2c. Available from Internet: <https://www.pivtec.com>.
- Gomes, M.P., B.N. Sismanoglu and J. Amorim (2009). Characterization of microhollow cathode discharges. *Brazilian Journal of physics* **39**(1), 25–30.
- Grabowski, L.R., E.M. Van Veldhuizen, A.J.M. Pemen and W.R. Rutgers (2007). Breakdown of methylene blue and methyl orange by pulsed corona discharge. *Plasma Sources Science and Technology* **16**(2), 226.
- Gu, X.J., M.Z. Haq, M. Lawes and R. Woolley (2000). Laminar burning velocity and markstein lengths of methane-air mixtures. *Combustion and Flame* **121**(1-2), 41–58. cited By 438.
- Gulyaev, G.A., G.A. Popkov and Yu Shebeko (1985). Effect of a constant electrical field on combustion of a propane-butane mixture with air. *Combustion, Explosion and Shock Waves* **21**(4), 401–403.

- Hagelaar, G.J.M. and L.C. Pitchford (2005). Solving the boltzmann equation to obtain electron transport coefficients and rate coefficients for fluid models. *Plasma Sources Science and Technology* **14**(4), 722.
- Hassanein, A. and I. Konkashbaev (1998). Performance and lifetime assessment of reactor wall and nearby components during plasma instabilities. *Journal of nuclear materials* **258**, 645–652.
- Hensel, Karol, Zdenko Machala and Pierre Tardiveau (2009). Capillary microplasmas for ozone generation. *The European Physical Journal Applied Physics* **47**(2), 22813.
- Hippler, Rainer, Sigismund Pfau, Martin Schmidt and Karl Schoenbach (2001). Low temperature plasma physics: fundamental aspects and applications. pp. 530.
- Höft, H., M.M. Becker and M. Kettlitz (2016). Impact of gas flow rate on breakdown of filamentary dielectric barrier discharges. *Physics of Plasmas* **23**(3), 033504.
- Huang, Ying and Vigor Yang (2009). Dynamics and stability of lean-premixed swirl-stabilized combustion. *Progress in Energy and Combustion Science* **35**(4), 293 – 364.
- Ju, Yiguang and Wenting Sun (2015). Plasma assisted combustion: Dynamics and chemistry. *Progress in Energy and Combustion Science* **48**, 21 – 83.
- Karl, Schoenbach, El-Habachi Ahmed, Shi Wenhui and Ciocca Marco (1997). High-pressure hollow cathode discharges. *Plasma Sources Science and Technology* **6**(4), 468.
- Kim, Woogyung, M. Godfrey Mungal and Mark A. Cappelli (2010). The role of in situ reforming in plasma enhanced ultra lean premixed methane/air flames. *Combustion and Flame* **157**(2), 374–383.
- Klimov, Anatoly, Valentin Bityurin, A Kuznetsov, B Tolkunov, N Vystavkin and M Vasiliev (2004). External and internal plasma-assisted combustion. In *42nd AIAA Aerospace Sciences Meeting and Exhibit*, pp. 1014.
- Kogelschatz, Ulrich (2003). Dielectric-barrier discharges: Their history, discharge physics, and industrial applications. *Plasma Chemistry and Plasma Processing* **23**(1), 1–46.
- Kogelschatz, Ulrich, Baldur Eliasson and Walter Egli (1999). From ozone generators to flat television screens: history and future potential of dielectric-barrier discharges. *Pure and Applied Chemistry* **71**(10), 1819–1828.
- Kolb, Juergen, H. Mohamed, Robert Price, James Swanson, Angela Bowman, R.L. Chiavarini, M. Stacey and K.H. Schoenbach (2008). Cold atmospheric pressure air plasma jet for medical applications. *Applied Physics Letters* **92**(24), 241501.

- Korolev, Y.D. and I.B. Matveev (2006). Nonsteady-state processes in a plasma pilot for ignition and flame control. *IEEE Transactions on Plasma Science* **34**(6), 2507–2513.
- Kosarev, I.N., N.L. Aleksandrov, S.V. Kindysheva, S.M. Starikovskaia and A.Yu. Starikovskii (2009). Kinetics of ignition of saturated hydrocarbons by nonequilibrium plasma: C<sub>2</sub>H<sub>6</sub>- to C<sub>5</sub>H<sub>12</sub>-containing mixtures. *Combustion and Flame* **156**(1), 221 – 233.
- Kumar, Ashwani, Kapil Kumar, Naresh Kaushik, Satyawati Sharma and Saroj Mishra (2010). Renewable energy in india: Current status and future potentials. *Renewable and Sustainable Energy Reviews* **14**(8), 2434 – 2442.
- Lacoste, D.A., D.A. Xu, J.P. Moeck and C.O. Laux (2013). Dynamic response of a weakly turbulent lean-premixed flame to nanosecond repetitively pulsed discharges. *Proceedings of the Combustion Institute* **34**(2), 3259–3266.
- Laux, C.O., J. Andreasson and J. Risberg (2006). [www.specair-radiation.net](http://www.specair-radiation.net).
- Lawton, S.A. and A.V. Phelps (1978). Excitation of the  $b^1\Sigma_g^+$  state of O<sub>2</sub> by low energy electrons. *The Journal of Chemical Physics* **69**(3), 1055–1068.
- Lee, H.J., C.H. Shon, Y.S. Kim, S. Kim, G.C. Kim and M.G. Kong (2009). Degradation of adhesion molecules of G361 melanoma cells by a non-thermal atmospheric pressure microplasma. *New Journal of Physics* **11**(11), 115026.
- Lee, Sang Min, Cheol Soo Park, Min Suk Cha and Suk Ho Chung (2005). Effect of electric fields on the liftoff of nonpremixed turbulent jet flames. *IEEE Transactions on Plasma Science* **33**(5), 1703–1709.
- Leonov, Sergey, Dmitry Yarantsev, Anatoly Napartovich and Igor Kochetov (2006). Plasma-assisted combustion of gaseous fuel in supersonic duct. *IEEE Transactions on Plasma Science* **34**(6), 2514–2525.
- Li, Ting, Igor Adamovich and Jeffrey Sutton (2013). A burner platform for examining the effects of non-equilibrium plasmas on oxidation and combustion chemistry. *Combustion Science and Technology* **185**(6), 990–998.
- Li, Ting, Igor Adamovich and Jeffrey Sutton (2016). Effects of non-equilibrium plasmas on low-pressure, premixed flames. part 1: CH\* chemiluminescence, temperature, and OH. *Combustion and Flame* **165**, 50–67.
- Liao, S.Y., D.M. Jiang, Z.H. Huang, Ke Zeng and Q. Cheng (2007). Determination of the laminar burning velocities for mixtures of ethanol and air at elevated temperatures. *Applied Thermal Engineering* **27**(2-3), 374–380.
- Lieberman, Michael and Alan Lichtenberg (2005). *Principles of plasma discharges and materials processing*. John Wiley & Sons.



- Mallens, R.M.M., L.P.H. De Goey and C.K. Law (2000). A numerical study of the stabilisation of a lean laminar premixed V-shaped flame. *Combustion science and technology* **159**(1), 373–389.
- Michael, James, Tat Loon Chng and Richard Miles (2013). Sustained propagation of ultra-lean methane/air flames with pulsed microwave energy deposition. *Combustion and Flame* **160**(4), 796–807.
- Mintoussov, E.I., S.J. Pendleton, F.G. Gerbault, N.A. Popov and S.M. Starikovskaia (2011). Fast gas heating in nitrogen-oxygen discharge plasma: II. energy exchange in the afterglow of a volume nanosecond discharge at moderate pressures. *Journal of Physics D: Applied Physics* **44**(28), 285202.
- Morgan, Lowell (1992). A critical evaluation of low-energy electron impact cross sections for plasma processing modeling. ii: Cl<sub>4</sub>, SiH<sub>4</sub>, and CH<sub>4</sub>. *Plasma chemistry and plasma processing* **12**(4), 477–493.
- Moselhy, Mohamed and Karl Schoenbach (2003). Nanosecond pulse generators for microdischarge excimer lamps. In *Pulsed Power Conference, 2003. Digest of Technical Papers. PPC-2003. 14th IEEE International*, Volume 2, pp. 1317–1320. IEEE.
- Nagaraja, Sharath, Ting Li, Jeffrey A Sutton, Igor V Adamovich and Vigor Yang (2015). Nanosecond plasma enhanced H<sub>2</sub>/O<sub>2</sub>/N<sub>2</sub> premixed flat flames. *Proceedings of the Combustion Institute* **35**(3), 3471–3478.
- Nagaraja, Sharath, Vigor Yang, Zhiyao Yin and Igor Adamovich (2014). Ignition of hydrogen–air mixtures using pulsed nanosecond dielectric barrier plasma discharges in plane-to-plane geometry. *Combustion and Flame* **161**(4), 1026 – 1037.
- Naidis, G.V. (2007). Modelling of transient plasma discharges in atmospheric-pressure methane–air mixtures. *Journal of Physics D: Applied Physics* **40**(15), 4525.
- Natarajan, J, Y Kochar, T Lieuwen and J Seitzman (2009). Pressure and preheat dependence of laminar flame speeds of H<sub>2</sub>/CO/CO<sub>2</sub>/O<sub>2</sub>/He mixtures. *Proceedings of the Combustion Institute* **32**(1), 1261–1268.
- Nehra, Vijay, Ashok Kumar and H.K. Dwivedi (2008). Atmospheric non-thermal plasma sources. *International Journal of Engineering* **2**(1), 53–68.
- Nijdam, S., F. van de Wetering, R. Blanc, E.M. van Veldhuizen and U. Ebert (2010). Probing photo-ionization: experiments on positive streamers in pure gases and mixtures. *Journal of Physics D: Applied Physics* **43**(14), 145204.
- Nijdam, S., G. Wormeester, E.M. Van Veldhuizen and U. Ebert (2011). Probing background ionization: positive streamers with varying pulse repetition rate and with a radioactive admixture. *Journal of Physics D: Applied Physics* **44**(45), 455201.

- Ombrello, Timothy, Xiao Qin, Yiguang Ju, Alexander Gutsol, Alexander Fridman and Campbell Carter (2006). Combustion enhancement via stabilized piecewise nonequilibrium gliding arc plasma discharge. *AIAA journal* **44**(1), 142–150.
- Ombrello, Timothy, Sang Hee Won, Yiguang Ju and Skip Williams (2010). Flame propagation enhancement by plasma excitation of oxygen. part I: Effects of O<sub>3</sub>. *Combustion and Flame* **157**(10), 1906 – 1915.
- Ono, Ryo and Tetsuji Oda (2003). Dynamics of ozone and OH radicals generated by pulsed corona discharge in humid-air flow reactor measured by laser spectroscopy. *Journal of applied physics* **93**(10), 5876–5882.
- Pai, David, Gabi Stancu, Deanna Lacoste and Christophe Laux (2009). Nanosecond repetitively pulsed discharges in air at atmospheric pressure—the glow regime. *Plasma Sources Science and Technology* **18**(4), 045030.
- Papadakis, A., S. Rossides and A. Metaxas (2011). Microplasmas: A review. *The Open Applied Physics Journal* **4**(1).
- Paris, P., M. Aints, F. Valk, T. Plank, A. Haljaste, K.V. Kozlov and H-E Wagner (2005). Intensity ratio of spectral bands of nitrogen as a measure of electric field strength in plasmas. *Journal of Physics D: Applied Physics* **38**(21), 3894.
- Park, Okjoo, Peter Veloo, Ning Liu and Fokion Egolfopoulos (2011). Combustion characteristics of alternative gaseous fuels. *Proceedings of the Combustion Institute* **33**(1), 887–894.
- Pedersen, Timothy and Robert Brown (1993). Simulation of electric field effects in premixed methane flames. *Combustion and Flame* **94**(4), 433–448.
- Phelps, A.V. and L.C. Pitchford (1985). Anisotropic scattering of electrons by N<sub>2</sub> and its effect on electron transport. *Physical Review A* **31**(5), 2932.
- Pilla, Guillaume, David Galley, Deanna Lacoste, Francois Lacas, Denis Veynante and Christophe O Laux (2006). Stabilization of a turbulent premixed flame using a nanosecond repetitively pulsed plasma. *IEEE Transactions on Plasma Science* **34**(6), 2471–2477.
- Raffel, Markus, Christian Willert, Jürgen Kompenhans et al. (2007). *Particle image velocimetry: a practical guide*. Springer Science & Business Media.
- Raffel, Markus, Christian E Willert, Steven T Wereley and Jürgen Kompenhans (2013). *Particle image velocimetry: a practical guide*. Springer.
- Rallis, Costa John and Ashton Martin Garforth (1980). The determination of laminar burning velocity. *Progress in Energy and Combustion Science* **6**(4), 303–329.
- Roupassov, D.V., A.A. Nikipelov, M.M. Nudnova and A. Yu Starikovskii (2009). Flow separation control by plasma actuator with nanosecond pulsed-periodic discharge. *AIAA journal* **47**(1), 168–185.

- Rusterholtz, Diane (2012). *Nanosecond repetitively pulsed discharges in atmospheric pressure air*. Ph. D. thesis, Ecole Centrale Paris.
- Rusterholtz, D.L., D.A. Lacoste, G.D. Stancu, D.Z. Pai and C.O. Laux (2013). Ultrafast heating and oxygen dissociation in atmospheric pressure air by nanosecond repetitively pulsed discharges. *Journal of Physics D: Applied Physics* **46**(46), 464010.
- Saito, Masahiro, Toshihiro Arai and Masataka Arai (1999). Control of soot emitted from acetylene diffusion flames by applying an electric field. *Combustion and Flame* **119**(3), 356 – 366.
- Sakai, Osamu, Yutaka Kishimoto and Kunihide Tachibana (2005). Integrated coaxial-hollow micro dielectric-barrier-discharges for a large-area plasma source operating at around atmospheric pressure. *Journal of Physics D: Applied Physics* **38**(3), 431.
- Sansonetti, Craig, Marc Salit and Joseph Reader (1996). Wavelengths of spectral lines in mercury pencil lamps. *Applied optics* **35**(1), 74–77.
- Schiffer, Hans-Wilhelm, Tom Kober and Evangelos Panos (2018). World energy council's global energy scenarios to 2060. *Zeitschrift für Energiewirtschaft* **42**(2), 91–102.
- Schoenbach, Karl, R. Verhappen, T. Tessnow, F.E. Peterkin and W.W. Byszewski (1996). Microhollow cathode discharges. *Applied Physics Letters* **68**(1), 13–15.
- Schutze, Andreas, James Jeong, Steven Babayan, Jaeyoung Park, Gary Selwyn and Robert Hicks (1998). The atmospheric-pressure plasma jet: a review and comparison to other plasma sources. *IEEE transactions on plasma science* **26**(6), 1685–1694.
- Shashurin, A., M. Keidar, S. Bronnikov, R.A. Jurjus and M.A. Stepp (2008). Living tissue under treatment of cold plasma atmospheric jet. *Applied Physics Letters* **93**(18), 181501.
- Shibkov, Valery, Vladimir Chernikov, Alexey Ershov, R Konstantinovskij, L Shibkova and Valery Zlobin (2004). Propane-butane-air mixture ignition and combustion in the aerodynamic channel with the stagnant zone. In *42nd AIAA Aerospace Sciences Meeting and Exhibit*, pp. 838.
- Shimizu, K., T. Ishii and M. Blajan (2010). Emission spectroscopy of pulsed power microplasma for atmospheric pollution control. *IEEE Transactions on Industry Applications* **46**(3), 1125–1131.
- Shimizu, Kazuo, Takeki Sugiyama and Manisha NL Samaratunge (2008). Study of air pollution control by using micro plasma filter. *IEEE Transactions on Industry Applications* **44**(2), 506–511.

- Shimizu, Kazuo, Akira Umeda and Marius Blajan (2011). Surface treatment of polymer film by atmospheric pulsed microplasma: Study on gas humidity effect for improving the hydrophilic property. *Japanese Journal of Applied Physics* **50**(8S2), 08KA03.
- Shoshin, Yuriy, Robert Johan Maria Bastiaans and Laurentius Philippus Hendrika de Goey (2013). Anomalous blow-off behavior of laminar inverted flames of ultra-lean hydrogen–methane–air mixtures. *Combustion and Flame* **160**(3), 565–576.
- Shoshin, Yuriy and Jozef Jarosinski (2009). On extinction mechanism of lean limit methane–air flame in a standard flammability tube. *Proceedings of the Combustion Institute* **32**(1), 1043 – 1050.
- Sismanoglu, B.N., K.G. Grigorov, R. Caetano, M.V.O. Rezende and Y.D. Hoyer (2010). Spectroscopic measurements and electrical diagnostics of microhollow cathode discharges in argon flow at atmospheric pressure. *The European Physical Journal D-Atomic, Molecular, Optical and Plasma Physics* **60**(3), 505–516.
- Somers, L.M.T. (1994). The simulation of flat flames with detailed and reduced chemical models. *Eindhoven University of Technology, Eindhoven*.
- Stonies, Robert, Susanne Schermer, Edgar Voges and José AC Broekaert (2004). A new small microwave plasma torch. *Plasma Sources Science and Technology* **13**(4), 604.
- Sun, Hongyan, S.I. Yang, G. Jomaas and C.K. Law (2007). High-pressure laminar flame speeds and kinetic modeling of carbon monoxide/hydrogen combustion. *Proceedings of the Combustion Institute* **31**(1), 439–446.
- Sun, Wenting, Sang Hee Won, Timothy Ombrello, Campbell Carter and Yiguang Ju (2013). Direct ignition and S-curve transition by in situ nano-second pulsed discharge in methane/oxygen/helium counterflow flame. *Proceedings of the Combustion Institute* **34**(1), 847–855.
- Sung, C.J., C.K. Law and A. Umemura (1992). On adiabatic stabilization of inverted flames. In *Symposium (International) on Combustion*, Volume 24, pp. 205–212. Elsevier.
- Tahtouh, Toni, Fabien Halter and Christine Mounaïm-Rousselle (2009). Measurement of laminar burning speeds and markstein lengths using a novel methodology. *Combustion and Flame* **156**(9), 1735–1743.
- Tien, J.H. and M. Matalon (1991). On the burning velocity of stretched flames. *Combustion and Flame* **84**(3-4), 238–248.
- Turns, Stephan R. (2000). An introduction to combustion: Concepts and application.

- Uddi, Mruthunjaya, N. Jiang, I.V. Adamovich and W.R. Lempert (2009). Nitric oxide density measurements in air and air/fuel nanosecond pulse discharges by laser induced fluorescence. *Journal of Physics D: Applied Physics* **42**(7), 075205.
- Vagelopoulos, C.M. and F.N. Egolfopoulos (1998). Direct experimental determination of laminar flame speeds. In *Symposium (international) on combustion*, Volume 27, pp. 513–519. Elsevier.
- Vance, F.H., Y. Shoshin, J.A. van Oijen and L.P.H. de Goeij (2018). Effect of lewis number on premixed laminar lean-limit flames stabilized on a bluff body. *Proceedings of the Combustion Institute*.
- Wang, Z.H., L. Yang, Bo Li, Z.S. Li, Z.W. Sun, Marcus Aldén, K.F. Cen and A.A. Konnov (2012). Investigation of combustion enhancement by ozone additive in CH<sub>4</sub>/air flames using direct laminar burning velocity measurements and kinetic simulations. *Combustion and flame* **159**(1), 120–129.
- Warnock, J. N., K. Bratch and M. Al-Rubeai (2005). *Packed Bed Bioreactors*, pp. 87–113. Dordrecht: Springer Netherlands.
- Weltmann, Klaus-Dieter, Katja Fricke, Manfred Stieber, Ronny Brandenburg, Thomas von Woedtke and Uta Schnabel (2012). New nonthermal atmospheric-pressure plasma sources for decontamination of human extremities. *IEEE Transactions on Plasma Science* **40**(11), 2963–2969.
- Westerweel, Jerry (1997). Fundamentals of digital particle image velocimetry. *Measurement science and technology* **8**(12), 1379.
- Whitaker, Stephen (1972). Forced convection heat transfer correlations for flow in pipes, past flat plates, single cylinders, single spheres, and for flow in packed beds and tube bundles. *AIChE Journal* **18**(2), 361–371.
- Winands, G., Keping Yan, A. Pemen, S. Nair, Zhen Liu and E. Van Heesch (2006). An industrial streamer corona plasma system for gas cleaning. *IEEE transactions on plasma science* **34**(5), 2426–2433.
- Xu, Da (2013). *Thermal and hydrodynamic effects of nanosecond discharges in air and application to plasma-assisted combustion*. Ph. D. thesis, Ecole Centrale Paris.
- Yagodnikov, D.A. and A.V. Voronetskii (1994). Effect of an external electrical field on ignition and combustion processes. *Combustion, Explosion and Shock Waves* **30**(3), 261–268.
- Yazicioglu, Ozge and T. Yacar Latircioglu (2017). Applications of plasma technology in energy sector. *Journal of Engineering and Science* **3**, 18–24.
- Yin, Z., I.V. Adamovich and W.R. Lempert (2013). OH radical and temperature measurements during ignition of H<sub>2</sub>-air mixtures excited by a repetitively pulsed nanosecond discharge. *Proceedings of the Combustion Institute* **34**(2), 3249–3258.

- Yokomori, Takeshi, Zheng Chen and Yiguang Ju (2006). Studies on the flame curvature effect on burning velocity. In *44th AIAA Aerospace Sciences Meeting and Exhibit*, pp. 161.
- Yu, Qinqin, Meng Kong, Tong Liu, Jinhua Fei and Xiaoming Zheng (2012). Characteristics of the decomposition of CO<sub>2</sub> in a dielectric packed-bed plasma reactor. *Plasma Chemistry and Plasma Processing* **32**(1), 153–163.
- Zhang, Ding-Zong, Yan-Hui Wang and De-Zhen Wang (2017). Numerical study on the discharge characteristics and nonlinear behaviors of atmospheric pressure coaxial electrode dielectric barrier discharges. *Chinese Physics B* **26**(6), 065206.
- Zhang, Shuai, Wen-chun Wang, Peng-chao Jiang, De-zheng Yang, Li Jia and Sen Wang (2013). Comparison of atmospheric air plasmas excited by high-voltage nanosecond pulsed discharge and sinusoidal alternating current discharge. *Journal of Applied Physics* **114**(16), 163301.



# List of Symbols

## Operators

$A$	Area
$d$	Hole diameter
$D_e$	Diffusion coefficient
$E$	Energy
$E/N$	Reduced electric field strength
$C$	Capacitance
$c$	Speed of light
$F$	Frequency
$Q$	Volume flow rate
$I$	Intensity
$I$	Current
$Q$	Volume flow rate
$k$	Thermal conductivity
$k_r$	Rate of reaction
$k_B$	Boltzmann constant
$m_b$	Mass burning velocity
$P$	Pressure
$T$	Temperature
$R$	Resistance
$S_L$	Laminar burning velocity
$u$	Axial velocity component
$v$	Radial velocity component
$V$	Voltage
$t$	Time



---

$T_e$	Electron temperature
$T_i$	Ion temperature
$T_g$	Gas temperature
$n_e$	Electron density
$N_s$	Seeding number density
$S$	Sensitivity

**Subscript**

corr	Corrected
cap	Capacitive
eff	Effective
out	Outlet
in	Inlet
g	Gas
e	Electron
meas	Measured
min	Minimum
max	Maximum
rot	Rotational
vib	Vibrational

**Greek**

$\phi$	Equivalence ratio
$\rho$	Density
$\alpha$	Angle
$\alpha_{eff}$	Effective ionization coefficient
$\nu$	Frequency
$\lambda$	Wavelength
$\gamma$	Wavelength
$\Delta$	Delta
$\mu$	Micron
$\mu_e$	Electron mobility
$\sigma$	Skin depth

# List of Abbreviations

APPJ	Atmospheric Pressure Plasma Jet
AC	Alternative Current
CAM	Computer Aided manufacturing
CFD	Computational Fluid dynamics
CCD	Charge-Coupled Device
CH <sub>4</sub>	Methane
CO	Carbon monoxide
CO <sub>2</sub>	Carbon dioxide
CH*	Electronically-excited Methylidyne
DBD	Dielectric Barrier Discharge
DC	Direct Current
EMF	Electromagnetic Field
EEDF	Electron Energy Distribution Function
FS	Full Scale
FPS	Frame Per Second
HTP	High Temperature Plasma
HV	High voltage
LIF	Laser Induced Fluorescence
LTE	Local Thermal Equilibrium
MHCD	Micro-hollow Cathode Discharge
MFC	Mass Flow Controller
NO <sub>x</sub>	Nitrogen Oxides
NTP	Non-Thermal Plasma

NPR	Nanosecond Repetitively Pulsed
OH	Particle Image Velocimetry
OH*	Electronically-excited hydroxyl
PIV	Particle Image Velocimetry
PAC	Plasma-Assisted Combustion
ppm	Part per million
SPS	Second Positive System
SE	Shielding Effectiveness
RF	Radio-frequency
RCP	Representative Concentration Pathways
TALIF	Two-Photon Absorption Laser Induced Fluorescence
UV	Ultra-Violet
WHO	World Health Organization

# Acknowledgments

With my sincere regards I would like to thank professor Ute Ebert, my promoter, who introduced me to the Multiphase and Reacting Flow group in mechanical department at Eindhoven university of Technology. Without her support from early beginning this project would never have seen the light. I really enjoyed and learned a lot from our regular discussions.

I want to take this opportunity to express my deep regards to professor Philip de Goey, my promoter, who gave me the opportunity to work within this group and start my PhD project under his supervision. Thanks for giving me the guidance and the freedom to shape the project in the way that I like. This allows me to improve my independent research capabilities as well as my technical skills.

I would like to express my most sincere gratitude to my supervisors Jeroen, Sander and Yuriy for their support, motivation and fruitful discussions. Thanks for being beside me at every situation I have faced. Sander, I greatly appreciate your valuable effort and time for transferring your knowledge and experience to me and reviewing my papers and thesis. We had hard times to get the reactor working, but finally we did it. Jeroen, there are no words can express my deep gratitude to you. I really owe you a great deal for your hard work with me through all these years. Yuriy, you accepted to join my project in a very critical moment. However, you worked very hard with me to setup and finish the experiments in the right time. I do feel lucky to get the opportunity to work with you all.

I would like to extend my gratitude to Nico Dam. Nico, thank you for sharing your valuable knowledge and experience on optical diagnostics as well as plasma discharges. I really appreciate all the time you spent with me setting up the experiments and attending my regular meetings.

Acknowledgments to Dr. Eddie van Veldhuisen who gave me the opportunity to work under his supervision in the plasma laboratories. He spent with me a lot of effort and time for initiating and testing the first ideas of the DBD microplasma reactor. I really appreciate his unique way of explaining complicated physics issues in a very efficient and easy way.

Beside Philip, Ute, Yuriy, Jeroen and Sander, I also would like to thank the members of my thesis committee, Dr. Bergthorson, Prof. Kroesen and Prof. Pemen

for their reviews and efforts committed to improve this dissertation.

I was so happy to have a lot of friends beside me during my exciting PhD journey. I would like to specifically mention Mohamed Darwish, Mohammed Ezz, Faizan Vance, Ahmed Shahin, Abdullah Sanad, Ahmed El-Agamy and Omar Shokry and their families for always being there at any hard time. We also spent a lot of pleasant time together.

It was a pleasure to be among a large group of fellow researchers and friend in mechanical and physics departments: Uger, Yigit, Suliman, Zhen, Faizan, Taha, Aromal, Denis, Amin, Samaneh, Robben, Camila, Marjan, Ravi, Marc, Tom and many others. You made my daily working hours full of joy and excitement. I was always enjoying our interactions and conversations about different aspects of life. I wish to thank Hans, Theo, Martin, Henri, Jaap, Bart, Jan and Frank who made the life in the lab a way easier, your help is very appropriated. You were always ready to design, troubleshoot and fix my problems, thanks you.

A special thanks to Leon, Marcel and Stijn, the founders of Bright Society, for believing in my talent. You made the transition from the academic life to the industry very efficient and smooth. I enjoyed a lot our conversations during our meetings and your amazing events. Only few people have a long-term effect on my life, and you are definitely among them.

My deepest gratitude goes to my mother for her outstanding inspiration to me. Getting to this stage in my life has taken a lot of work, but it is nothing compared to how you worked and sacrificed for me. Fatma and Eman, my sisters, my heartfelt thanks for your support, affection and encouragement. You are the best gift from Allah to me.

The last and the most special person I want to thank is my beloved wife Marwa. Marwa, without your sacrifice and support, I could never have accomplished the achievement I have today, if there is any. Thanks for sharing all the difficult moments that we have faced together. My beautiful daughters, Nour and Karma, your smiles kept my spirits always high. I love you all.

# List of Publications

## Journal papers

Elkholy, A.H.E., Y. Shoshyn, S. Nijdam, E.M. van Veldhuizen, J.A. van Oijen, U. Ebert and L.P.H. de Goey (2018). Burning velocity measurement of methane-air flame in a new DBD microplasma burner platform. *Experimental Thermal Fluid Science Journal* **95**, 18-26.

Elkholy, A.H.E., S. Nijdam, E.M. van Veldhuizen, U. Ebert, J.A. van Oijen, N.J. Dam, L.P.H. de Goey (2018). Characteristics of a novel nanosecond DBD microplasma reactor for flow applications. *Plasma Sources Science and Technology* **27**(5), 055014.

Elkholy, A.H.E., Y. Shoshyn, S. Nijdam, J.A. van Oijen, U. Ebert and L.P.H. de Goey. PIV measurement for determination of the local burning velocity of plasma-assisted methane-air combustion. In preparation, to be submitted to *Combustion and Flame Journal*.

## Conference proceedings

Elkholy, A.H.E., Y. Shoshyn, S. Nijdam, E.M. van Veldhuizen, J.A. van Oijen and L.P.H. de Goey (2018). A new DBD microplasma burner for measuring the effect of nanosecond plasma discharge on burning velocity of methane-air flames. *MCS-10 : Tenth Mediterranean Combustion Symposium, 17-21 September 2017, napoli, Italy*.

Elkholy, A.H.E., V. Kornilov, J.A. van Oijen and L.P.H. de Goey (2015). Plasma-assisted combustion: interaction of a flat flame with a nanosecond dielectric barrier discharge plasma. *COMBURA 2015, 7-8 October 2015, Soesterberg, The Netherlands*.



# Curriculum Vitae

Ahmed Elkholy was born on 9 January 1982 in Cairo, Egypt. He is a researcher with an interest of thermo-fluid dynamics, energy, optical/laser diagnostics and nanosecond plasma discharges.

## Education

- 2014 —2019** PhD, mechanical Engineering.  
Eindhoven University of technology, Eindhoven, the Netherlands.  
Mechanical engineering department.  
PhD Dissertation: Development of a nanosecond DBD plasma reactor for combustion applications.
- 2007 —2010** MSc, Mechanical engineering.  
Helwan University, Cairo, Egypt.  
Mechanical Engineering department.  
MSc thesis: Computational and experimental study for droplet behavior under flashing condition.
- 1998 —2003** BSc, Mechanical engineering.  
Helwan University, Cairo, Egypt.  
Mechanical engineering department.  
BSc Project: combustion characteristics of lean flame in bluff body burner.

## Professional experience

**March 2018 —Present**  
Vacuum system designer —ASML, Veldhoven, the Netherlands.



**April 2009 —March 2014**

Technical Project leader —Reyam consulting office, Cairo, Egypt.

**April 2007 —March 2009**

Senior Mechanical Engineer —ZFP Zuhair Fayez Partnership Consultants, Cairo, Egypt.

**May 2004 —March 2007**

Junior Mechanical Engineer —EMG Electro-mechanical design group, Cairo, Egypt.